MEASUREMENTS OF CROSS SECTION AND NORMALIZED DIFFERENTIAL CROSS SECTION OF TOP QUARK PAIR PRODUCTION IN PP COLLISIONS AT SQRT(S)=7 TEV

A Dissertation

Presented to the Faculty of the Graduate School

of Cornell University

in Partial Fulfillment of the Requirements for the Degree of

Doctor of Philosophy

by

Yao Weng

May 2013

MEASUREMENTS OF CROSS SECTION AND NORMALIZED DIFFERENTIAL CROSS SECTION OF TOP QUARK PAIR PRODUCTION IN PP COLLISIONS AT SQRT(S)=7 TEV

Yao Weng, Ph.D.

Cornell University 2013

Two measurements are reported in this thesis. First, the cross section of the top quark pair production in proton proton collisions is measured in the electron plus jets channel, using 857.7 pb^{-1} of 2011 data recorded by the CMS experiment at $\sqrt{s} = 7$ TeV. This measurement relies on kinematic distributions to statistically separate the signal from the Standard Model backgrounds. Data-driven methods are employed to minimize the dependence on the simulation. The measured cross section is $\sigma_{t\bar{t}} = 166.7^{+78.2}_{-69.3}$ (stat. $\oplus$ syst.) pb, which is in agreement with NLO perturbative QCD calculation. In the second measurement, the $t\bar{t}$ normalized differential cross section with respect to the jet multiplicity is determined. The data used in the later analysis amounts to 5 fb^{-1}, which was taken during the full 2011 run by CMS. A b-tagging technique is applied to efficiently reject Standard Model backgrounds. The measured total cross section is $\sigma_{t\bar{t}} = 161.2^{+12.4}_{-11.6}$ (stat. $\oplus$ syst.) pb, which is used for normalization. The resulting differential cross section shows good agreement with the Standard Model prediction, and provides an important input for comparisons between different Monte Carlo generators.

Biographical Sketch

Yao Weng was born in Tianjin, China in 1982. She attended Huazhong University in Wuhan, China in 2000, majored in physics, and received her Bachelor of Science in the summer of 2004. In the fall of 2004, she spent one year to take some advanced courses of physics in Graduate School of Chinese Academy of Science, Beijing, China. After that, she joined in the BESII (Beijing Sepctrometer) collaboration in Institute of High Energy Physics. She worked in the R value group under the direction of Prof. Haiming Hu for two years and received her Master of Science in the summer of 2007.

In the spring of 2007, Yao got an admission of the Ph.D. program from Cornell physics department and started her graduate study in the fall. After taking the required courses, she started working with Prof. Julia Thom on the top quark physics in the Cornell CMS group in 2008. She got her Master of Science from Cornell University in 2010 after passing the A exam, at the same time Prof. Julia Thom promoted her to be a Ph.D. candidate. Her thesis project was to measure the cross section and normalized differential cross section of top quark pair production with the CMS experiment.

Dedicated to My Parents.

Acknowledgments

This thesis could not be finished without the help of many people in many different ways, this is my huge thank-you to all of you.

Foremost, I would like to express my deepest gratitude to my advisor, who is also my committee chair, Prof. Julia Thom for her encouragement and support during my graduate studies. She offered me a great opportunity to work in the CMS collaboration, and tailored a program with interesting physics well suited for me. She always gave me the freedom in pursuing research and guided me through the difficult problems I met in the research, so the work in this thesis was also yours. I gratefully thank my other committee members: Prof. Peter Wittich and Prof. Csaba Csaki for their long term instruction on both theory and experiments, and their valuable comments and suggestions for this thesis.

The research in this thesis was conducted with the CMS experiment of LHC. We built a wide collaboration with CERN, Brunel University, Rice University, Vrije University, and Karlsruhe Institute of Technology. I wish to thank Freya Blekman, Karl Ecklund, Matthew Chadwick, Matthew Barrett, Vesna Cuplov, Hongwan Liu, William Martin and James Zabel for helping me understand the physics, statistics and computing used in the analysis. Without your efforts and hard working, our measurement with early data from LHC could not have been published. I worked with Enrique Palencia, Philip Symonds and Martijn Mulders on top quark physics study almost three years, it is hard to describe the warm kindness I had taken from this team. Thank you for developing analysis strategy, tracking problems and submitting grid jobs in data preparation. I also appreciate the collaboration with Alexis Descroix, Ulrich Husemann, Patrica Lobelle, and Shawn Williamson. Though it took almost one year to make the results of the normalized differential cross section

measurement public, I was very happy to work with you as you were always resourceful in understanding top quark physics and considerate when I fell behind with my analysis work.

I owed thanks to people in Cornell CMS group. Prof. Ritchie Patterson and Prof. Jim Alexander sent me offer to work in LEPP. Prof. Lawrence Gibbons, Chris Jones, Dan Riley and Valentin Kuznetsov taught me the knowledge of CMS software, especially the programming skills in C++. Prof. Anders Ryd involved me in the Pixel online software development project, which furthered my understanding in detectors and parallel programming. My officemates Don Teo and Stephen Poprocki were always tolerant of my endless questions in the analysis and in English grammar. I also thank people located in CERN and Fermilab: Walter Hopkins, Ben Kreis, Luke Winstrom and Josh Thompson, exchanging the instant message with them helped me quickly fix the problems in my work. The senior students: Xin Shi, Darren Puigh, Steve Stroiney, Avishek Chatterjee, and Jennifer Vaughan, kindly shared the experience in pursuing their Ph.D. with me. It helped me in dealing with problems in both courses and analysis. My special thanks go to Flip Tanedo for helping reviewing my theory chapter of this thesis, and to Gala Kaufman and Susan Dittmer for discussing top physics.

I lived in Ithaca for six years and made lots of friends, i.e. Y.J. Chen, Wan Li, P.J. Zhou, Jingxian Zheng, Qingqun Mao, Yang Xie, Lin Xue, Hui Liu, Yi-Ting Hsu, Haiyan Deng, Yang Zhang and Kaifu Bian. There is a long list of names, but I cannot put them all here. Thank all of you for the company and support. Last but not least, I send this ancient aphorism to my parents “great sound is hard to hear, great love is beyond words”, thank them for years of love !

Table of Contents

List of Figures

List of Tables

CHAPTER 1

Introduction

The Standard Model (SM) theory of particle physics was developed in the early 1970's by Sheldon Glashow, Steven Weinberg and Abdus Salam [1][2][3]. It has been verified in a very wide range of energies by a variety of experiments. In SM, the basic blocks of universe are leptons and quarks. Their interactions are mediated by gauge bosons, namely, photons, W and Z bosons, and gluons. The SM incorporates theories for three fundamental forces: the electromagnetic, weak and strong nuclear forces but leaves out gravity. All the fundamental particles predicted by SM receive their mass by interacting with the Higgs boson.

The heaviest particle in the SM is the top quark, and its existence was confirmed almost two decades ago at the Tevatron [4][5] ($\sqrt{s} = 1.96$ TeV) at Fermilab. Two collaborations, CDF and DØ, measured top quark properties, i.e. the production cross section of top pairs and single top, mass, charge asymmetry, top pair spin correlation, etc. These measurements are important for testing the SM and searching for new physics.

The Top quark was rediscovered by ATLAS (A Toroidal LHC Apparatus) and CMS (Compact Muon Solenoid) at the LHC (Large Hadron Collider) at $\sqrt{s} = 7$ TeV only a few months after its first run on Nov. 20^{th} 2009 [6][7]. Fig. 1.1[8] shows the measured and predicted $t\bar{t}$ production cross sections from the Tevatron and LHC, where the $t\bar{t}$ production cross section at LHC is 20 times greater than that at the Tevatron. The large production cross section and large instantaneous luminosity of the LHC ensure a high top quark production rate. In 2011, around 8×10^5 top quark pairs were produced [9]. This enables the precise study of many aspects of the top quark.

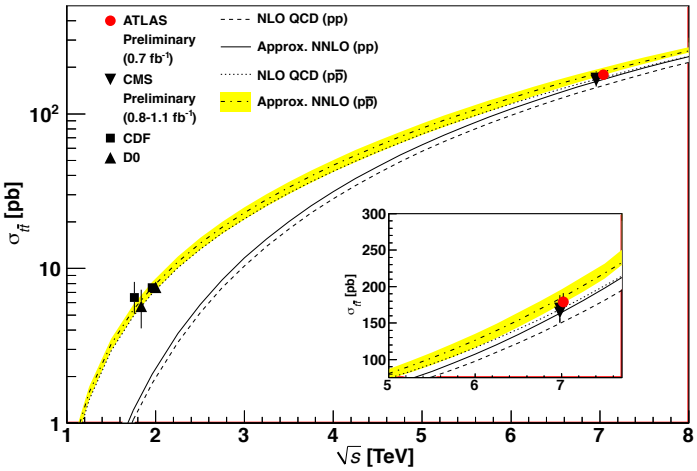

Figure 1.1: $t\bar{t}$ production cross section measurements from the Tevatron and LHC, compared with NLO and NNLO calculation. The plot is taken from [8].

The work described in this thesis includes the measurements of the top quark pair cross section and normalized differential cross section with data collected during 2011 with the CMS experiment. The thesis is organized as follows: the theoretical foundation and motivation for the work in this thesis is introduced in Chapter 2. Chapter 3 presents a brief overview of the LHC, all sub-detectors of CMS as well as its trigger system. The physics objects used in the measurements are discussed in Chapter 4, including the reconstruction algorithms of individual object and their performance. Chapter 5 summarizes the dataset and event simulation for the analysis, event selections, and Monte Carlo (MC) reweighting procedures. Measurements of top quark pair production cross section and differential cross section with respect to jet multiplicity are detailed in Chapters 6 and 7. Both chapters are structured similarly: they start with the analysis strategy, followed by the background estimation and systematic uncertainty studies, and end with final results. The summary and outlook are given in Chapter 8.

Throughout this thesis, natural units are applied, in which the speed of light c and the reduced Planck constant $\hbar$ are set to one ($\hbar = c = 1$).

CHAPTER 2

Theoretical Background and Motivation

The theoretical foundations of this thesis are based on the Standard Model (SM). In this chapter, a short overview of the SM is presented in Section 2.1. Since the measurements described in this thesis deal with the top pair cross section and differential cross section, top quark physics, including top pair production at hadron colliders and top decay, is detailed in Section 2.2 and followed by a summary of the motivation in Section 2.3.

2.1 Overview of Standard Model

The SM describes the fundamental particles and their interactions. It is a relativistic quantum field theory that is invariant under the gauge group $\mathrm{SU(3)_C} \times \mathrm{SU(2)_L} \times \mathrm{U(1)_Y}$. $\mathrm{SU(3)_C}$ describes the strong interaction, which introduces three types of color charges C, and $\mathrm{SU(2)_L} \times \mathrm{U(1)_Y}$ describes the unification of electromagnetic and weak interactions, where L and Y are weak isospin and hypercharge respectively.

All matter particles are built from three generations of spin-1/2 fermions. Labeled according to their increasing masses, each generation is divided into a pair of quarks and a pair of leptons. The quark doublet contains an "up"-type (up, charm or top) quark with electric charge 2/3 and a "down"-type (down, strange or bottom) quark with electric charge $-1/3$. Quarks also carry color charges and are thus able to participate the strong interaction. The lepton doublet consists of an electron-like fermion (e, μ, or τ) with electric charge -1 and its neutral partner neutrino. The force carriers are spin-1 gauge bosons: the

massless photon γ mediates the electromagnetic interaction, the massive $W^{\pm}$ and Z bosons are responsible for the weak interaction, and the massless gluons for the strong interaction. Fig. 2.1 summarizes three families of quarks and leptons, as well as the forces carriers [10].

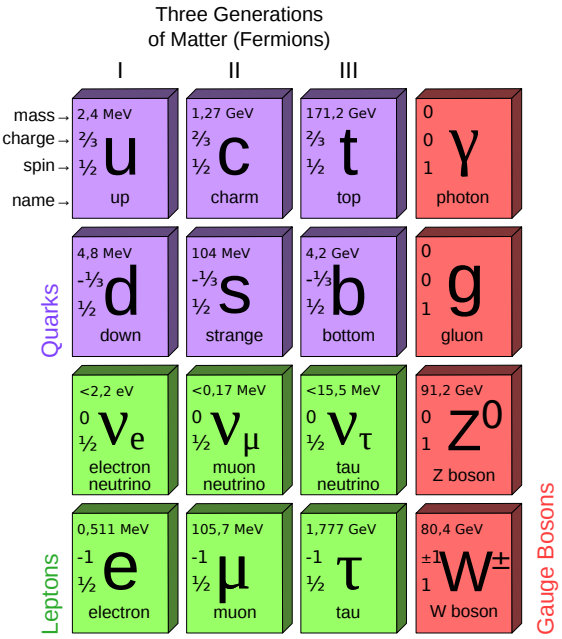

Figure 2.1: Standard Model elementary particles with their masses and charges, taken from [10].

2.1.1 Electroweak Sector and Higgs Mechanism

The electroweak (EWK) interaction in SM is based on the gauge group $\mathrm{SU(2)_L} \times \mathrm{U(1)_Y}$. There are three $\mathrm{SU(2)_L}$ gauge bosons W^a_μ, $a = 1,\ 2,\ 3$ with gauge coupling g and one $\mathrm{U(1)_Y}$ gauge boson B_μ with gauge coupling g'. Many experiments had confirmed that the charged weak force acts only on the left-handed[1] component of fermions [11][12]. The chirality is distinguished by the generator of $\mathrm{SU(2)_L}$, also called weak isospin I. The right-handed[2]

[1]Chirality for a fermion Ψ is determined by the chirality operator γ^5, i.e. $\gamma^5\Psi = \pm\Psi$. To construct chiral eigenstates out of an arbitrary fermion, we introduce projectors P_L and P_R, $P_{L(R)} = (1 \pm \gamma^5)/2$. The left and right handed components are $\Psi_L = P_L\Psi$ and $\Psi_R = P_R\Psi$ respectively.

[2]Right-handed neutrino does not exist in SM.

fermions are singlets with zero weak isospin. The left-handed fermions are doublets $\Phi = \begin{pmatrix} \nu_i \\ \ell_i^- \end{pmatrix}_L$ or $\begin{pmatrix} u_i \\ d_i' \end{pmatrix}_L$ with $I_3 = -1/2$ for leptons and down type quarks and $I_3 = 1/2$ for neutrinos and up type quarks. d_i' represents an eigenstate of the weak interaction, and is related to the mass eigenstate d_i via CKM matrix (V_{ij}) [13], i.e. $d_i' \equiv V_{ij} d_i$. The electric charge Q is related to the third component of weak isospin I_3 and weak hypercharge Y via $Q = I_3 + \dfrac{Y}{2}$, where $Y/2$ is the generator of $\mathrm{U(1)_Y}$. This construction ensures electric charge conservation after spontaneous symmetry breaking, which is explained below. Tab. 2.1 summarizes the electroweak assignments for I_3, Q and Y.

Table 2.1: $\mathrm{SU(2)_L \times U(1)_Y}$ assignment for I_3, Q and Y.

	ν_L^i	ℓ_L^i	ℓ_R^i	u_L	d_L	u_R	d_R
I_3	$1/2$	$-1/2$	0	$1/2$	$-1/2$	0	0
Q	0	-1	-1	$2/3$	$-1/3$	$2/3$	$-1/3$
Y	-1	-1	-2	$1/3$	$1/3$	$4/3$	$-2/3$

The covariant derivative with respect to $\mathrm{SU(2)_L \times U(1)_Y}$ gauge invariance is

$$\mathcal{D}_\mu = \partial_\mu + igW_\mu^a \tau^a + \frac{i}{2} g' Y B_\mu, \tag{2.1}$$

where τ^a are generators of $\mathrm{SU(2)}_L$ with $a = 1,\ 2,\ 3$, depending on representations of fermions. $\tau^a = \dfrac{\sigma^a}{2}$ (σ^a are Pauli matrices) for the left-handed doublets and $\tau^a = 0$ for right-handed singlets. The kinetic terms in the Lagrangian for fermions are

$$\mathcal{L}_{\text{fermion}} = \sum_{f \in (\text{lepton quarks})} i \bar{f} \gamma^\mu \mathcal{D}_\mu f, \tag{2.2}$$

where the sum runs over three generations of leptons and quarks. The kinetic terms of Lagrangian for the gauge fields is

$$\mathcal{L}_{\text{gauge}} = -\frac{1}{4} W_{\mu\nu}^a W_a^{\mu\nu} - \frac{1}{4} B_{\mu\nu} B^{\mu\nu}, \tag{2.3}$$

where the field strength tensors $W^a_{\mu\nu}$ and $B_{\mu\nu}$ are

$$W^a_{\mu\nu} = \partial_\mu W^a_\nu - \partial_\nu W^a_\mu - g\epsilon^{abc} W^b_\mu W^c_\nu \tag{2.4}$$

$$B_{\mu\nu} = \partial_\mu B_\nu - \partial_\nu B_\mu, \tag{2.5}$$

where ϵ^{abc} are three dimensional Levi-Civita symbols.

The Lagrangian in Eq. 2.2 and 2.3 does not contain mass terms for either the fermions or the gauge bosons, as mass terms would destroy the $\mathrm{SU(2)_L} \times \mathrm{U(1)_Y}$ gauge symmetry. Hence, the symmetry must be spontaneously broken while gauge bosons and fermions would obtain their mass. It is accomplished by introducing a $\mathrm{SU(2)_L}$ doublet $\phi = \begin{pmatrix} \phi^+ \\ \phi^0 \end{pmatrix} = \begin{pmatrix} (\phi_1 - i\phi_2)/\sqrt{2} \\ (\phi_3 - i\phi_4)/\sqrt{2} \end{pmatrix}$, where ϕ_i are four real fields. This complex scalar doublet ϕ is the so-called Higgs field with hypercharge $Y = 1$, and its simplest renormalizable potential is constructed as following

$$V(\phi) = \mu^2 \phi^\dagger \phi + \lambda \left(\phi^\dagger \phi\right)^2 \quad \lambda > 0, \tag{2.6}$$

$$= \frac{1}{2}\mu^2 \sum_{i=1}^{4} \phi_i^2 + \frac{1}{4}\lambda \left(\sum_{i=1}^{4} \phi_i^2 \right)^2 . \tag{2.7}$$

If $\mu^2 > 0$, the minimum of $V(\phi)$ is at $\phi = 0$ and the symmetry is thus preserved. However, if we choose $\mu^2 < 0$ and the vacuum expectation value (v.e.v) of ϕ as $\langle \phi_i \rangle = 0$, $i = 1, 2, 4$ and $\langle \phi_3 \rangle = v$, the minimum of $V(\phi)$ will occur at non-zero value v. The $\mathrm{SU(2)}_L \times \mathrm{U(1)_Y}$ symmetry in vacuum is thus broken, illustrated in Fig. 2.2. Since electric charge Q satisfies $Q = I_3 + \dfrac{Y}{2}$, $Q\langle\phi\rangle = 0$ which indicates that electromagnetism is unbroken.

To build the physical spectrum, Higgs field ϕ is parameterized by

$$\phi(x) = \exp\left(i \frac{\xi^a(x)\sigma^a}{v} \right) \begin{pmatrix} 0 \\ \dfrac{v + H(x)}{\sqrt{2}} \end{pmatrix} . \tag{2.8}$$

where $H(x)$ is the real field corresponding to the physical Higgs scalar and $\xi^a(x)$ are massless pseudoscalar: Nambu-Goldstone bosons [15]. But $\xi^a(x)$ disappear in the physical

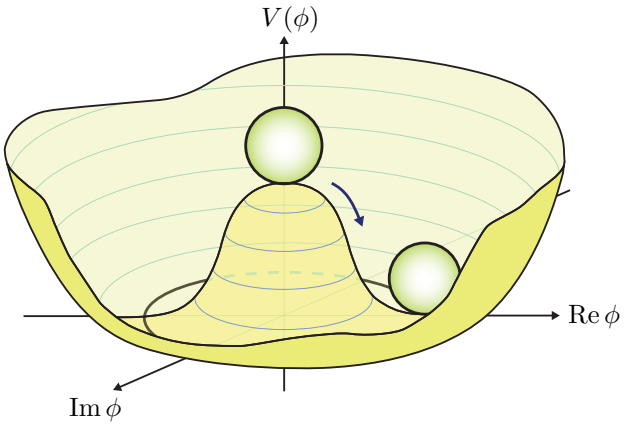

Figure 2.2: The potential of the Higgs field with $\mu^2 < 0$, taken from [14].

spectrum by gauge transformations $\phi' = \exp\left(-i\frac{\xi^a(x)\sigma^a}{v}\right)\phi = \begin{pmatrix} 0 \\ (v+H(x))/\sqrt{2} \end{pmatrix}$. Then the Lagrangian of Higgs field is

$$\mathcal{L}_{\text{Higgs}} = (\mathcal{D}^\mu\phi)^\dagger\,(\mathcal{D}_\mu\phi) - V(\phi). \tag{2.9}$$

The kinetic energy term in Eq. 2.9 contributes the following terms

$$(\mathcal{D}^\mu\phi)^\dagger\,(\mathcal{D}_\mu\phi) = \frac{1}{2}\,(0,\ v)\left(g\tau^a W_\mu^a + \frac{g'}{2}B_\mu\right)^2\begin{pmatrix} 0 \\ v \end{pmatrix} + H \text{ terms}. \tag{2.10}$$

We rotate the weak eigenstates of gauge bosons to their mass eigenstates as following,

$$W_\mu^\pm = \frac{1}{\sqrt{2}}\left(W_\mu^1 \mp iW_\mu^2\right) \tag{2.11}$$

$$Z_\mu = -\sin\theta_W B_\mu + \cos\theta_W W_\mu^3 \tag{2.12}$$

$$A_\mu = \cos\theta_w B_\mu + \sin\theta_W W_\mu^3, \tag{2.13}$$

where $\tan\theta_W \equiv \frac{g'}{g}$. Plug Eq. 2.11–2.13 into Eq. 2.10, the gauge bosons obtain mass

$$(\mathcal{D}^\mu\phi)^\dagger\,(\mathcal{D}_\mu\phi) = M_W^2 W_\mu^+ W^{-\mu} + \frac{M_Z^2}{2}Z_\mu Z^\mu - \frac{1}{4}F_{\mu\nu}F^{\mu\nu} + ..., \tag{2.14}$$

$$F_{\mu\nu} = \partial_\mu A_\nu - \partial_\nu A_\mu$$

where A^μ field remains massless, corresponding to the photon, and m_W and m_Z are

$$m_W = \frac{gv}{2}, \quad m_Z = \frac{v}{2}\sqrt{g^2 + g'^2} = \frac{m_W}{\cos\theta_W}. \tag{2.15}$$

Fermions gain mass through their Yukawa coupling with the Higgs boson, the gauge invariant terms in the Lagrangian are

$$\begin{aligned} \mathcal{L}_{\rm YW} &= \lambda_e \bar{\ell}_L \phi e_R + \lambda_u \bar{q}_L \phi^c u_R + \lambda_d \bar{q}_L \phi d_R + h.c. + 2^{\rm nd} \text{ and } 3^{\rm rd} \text{ generation} \\ &= \frac{\lambda_e v}{\sqrt{2}} \bar{e}_L e_R + \frac{\lambda_u v}{\sqrt{2}} \bar{u}_L u_R + \frac{\lambda_d v}{\sqrt{2}} \bar{d}_L d_R + ..., \end{aligned} \tag{2.16}$$

where $\phi^c \equiv -i\sigma_2 \phi^*$, and the mass terms of the first generation fermions are $m_e = \lambda_e v/\sqrt{2}$, $m_u = \lambda_u v/\sqrt{2}$ and $m_d = \lambda_d v/\sqrt{2}$.

In the SM, the full Lagrangian of the electroweak and Higgs sectors are the sum of Eq. 2.2, 2.3, 2.9 and 2.16, i.e. $\mathcal{L}_{\rm EWK} = \mathcal{L}_{\rm fermion} + \mathcal{L}_{\rm gauge} + \mathcal{L}_{\rm Higgs} + \mathcal{L}_{\rm YW}$. The v.e.v parameter v is determined experimentally from μ decay: $\mu \to e\bar{\nu}_e\nu_\mu$, where the measured Fermi constant is of $G_F = 1.166 \times 10^{-5}$ GeV^{-2} [16]. As $\frac{G_F}{\sqrt{2}} = \frac{g^2}{8M_W^2} = \frac{1}{2v^2}$, v is deduced to be ~ 246 GeV. The SM predicted the existence of W and Z bosons with $m_W = 80.381$ GeV and $m_W = 91.187$ GeV respectively, both of them were discovered at CERN by UA1 and UA2 collaborations [17][18] in 1981, and their latest mass as from PDG [8] are $m_W = 80.420 \pm 0.031$ GeV and $m_Z = 91.1876 \pm 0.0021$ GeV. ATLAS[19] and CMS[20] collaborations announced the discovery of a Higgs-like boson on July 4$^{\rm th}$ 2012, so far consistent with the SM properties. Its mass, using a combination of all available data, is 124.5 ± 0.8 GeV [8].

2.1.2 Strong Sector

The theory of strong interactions is referred to as Quantum Chromodynamics (QCD). In the SM, the $\mathrm{SU(3)_C}$ gauge symmetry is unbroken, and is governed by the following Lagrangian

$$\mathcal{L}_{\mathrm{QCD}} = i\bar{\psi}_q^i \gamma^\mu (\mathcal{D}_\mu)_{ij} \psi_q^j - m_q \bar{\psi}_q^i \psi_{qi} - \frac{1}{4} G_{\mu\nu}^a G_a^{\mu\nu}. \tag{2.17}$$

In Eq. 2.17, ψ_q^i denotes a quark field of flavor q with color index i running from 1 to $N_C = 3$, i.e. there are three color charges, m_q is the quark mass, $G_{\mu\nu}^a$ is the gluon field strength tensor, expressed as

$$G_{\mu\nu}^a = \partial_\mu A_\nu^a - \partial_\nu A_\mu^a - g_s f_{abc} A_\mu^b A_\nu^c, \tag{2.18}$$

where A_μ^a is the gluon field with index a running from 1 to $N_C^2 - 1 = 8$, i.e. there are eight different gluons, g_s is the QCD gauge coupling constant, f_{abc} are the $\mathrm{SU(3)_C}$ structure constants. They are related to $\mathrm{SU(3)_C}$ group generators t^a[3] as the following commutation:

$$\left[t^a,\ t^b\right] = i f_{abc} t^c. \tag{2.19}$$

$\mathcal{D}_\mu$ in Eq. 2.17 is the covariant derivative, defined as

$$(\mathcal{D}_\mu)_{ij} = \delta_{ij}\partial_\mu + i g_s t_{ij}^a A_\mu^a. \tag{2.20}$$

Owing to the non-Abelian character of the $\mathrm{SU(3)_C}$ group, the last term in Eq. 2.17 includes triple and quadruple gluon vertices. It thus gives rise to two important attributes for QCD: asymptotic freedom and color confinement.

Asymptotic freedom: Physical observables are calculated using a perturbation series in the coupling parameter $\alpha_s \equiv \dfrac{g_s^2}{4\pi}$. Renormalization is required to remove the ultraviolet

[3]Generators of $\mathrm{SU(3)_C}$ group correspond to eight 3×3 matrices. They satisfy $t^i = \dfrac{\lambda_i}{2}$, where λ_i are the Gell-Mann matrices [21].

divergences in the calculation. It thus introduces a mass scale μ_R (renormalization scale), at which physics of time scales $|t| \ll 1/\mu_R$ are removed from perturbative calculations, and induces a dependence of α_s on scale μ_R. In QCD, $\alpha_s(\mu_R^2)$ satisfies the following renormalization group equation (RGE):

$$\mu_R^2 \frac{\partial \alpha_s(\mu_R^2)}{\partial \mu_R^2} = \beta\left(\alpha_s(\mu_R^2)\right) = -\beta_0 \alpha_s^2(\mu_R^2) - \beta_1 \alpha_s^3(\mu_R^2) - \beta_2 \alpha_s^4(\mu_R^2) + \mathcal{O}\left(\alpha_s^5\right). \quad (2.21)$$

The negative sign in Eq. 2.21 is the result of gluon self-interactions when including all loop contributions in the RGE. Moreover, it is the origin of asymptotic freedom, i.e. the coupling constant decreases with increasing energy scale μ_R.

At one-loop order $\beta_0 = \dfrac{33 - 2N_f}{12\pi}$, where N_f is the number of active quark flavors at the energy scale μ_R. The solution of Eq. 2.21 in this one-loop approximation is

$$\alpha_s(Q^2) = \frac{\alpha_s(\mu_R^2)}{1 + \beta_0 \alpha_s(Q^2) \ln\left(\dfrac{Q^2}{\mu_R^2}\right)}, \quad (2.22)$$

where Q^2 is the momentum transfer in a given process and $\alpha_s(\mu_R^2)$ is the reference term. RGE only provides the evolution of the coupling constant, therefore, the mass of Z^0 is conventionally chosen as a specific reference scale. The latest value from PDG is $\alpha_s(M_Z^2) = 0.1184 \pm 0.0007$ [8]. $\alpha_s(Q^2)$ can thus be accurately determined at any energy scale $Q^2 \geq 1$ GeV^2. In order to illustrate asymptotic freedom, a new scale $\Lambda_{\text{QCD}}^2 = \dfrac{\mu_R^2}{e^{1/(\beta_0 \alpha_s(\mu_R^2))}}$ is introduced, which transforms Eq. 2.22 into

$$\alpha_s(Q^2) = \frac{1}{\beta_0 \ln\left(\dfrac{Q^2}{\Lambda_{\text{QCD}}^2}\right)}. \quad (2.23)$$

When $Q \gg \Lambda_{\text{QCD}}$, the coupling constant approaches to zero; and when Q is close to Λ_{QCD}, $\alpha_s(Q^2)$ will diverge to infinity and the perturbative approximation breaks down. Λ_{QCD} has been experimentally determined to be ~ 200 MeV, indicating the scale at which the strong

coupling constant blows up. Asymptotic freedom allows the use of perturbation theory to calculate cross sections of hard scattering processes in hadron-hadron collisions at the parton-level, which will be explained in Section 2.2.1.

Color confinement: Quarks and gluons are not observed in nature as free particles. Instead, they form color-neutral hadrons. In particle detectors, they are observed as jets which will be discussed in Section 4.4. The hadronization process (or fragmentation) involves a low momentum transfer and thus can not be calculated by perturbative theory. Therefore, we should resort to phenomenological models. The commonly used models are the string model [22], adopted by PYTHIA, and the cluster model [23] for HERWIG.

The string model is based on "linear confinement", where the potential from the color field between a quark (q) and an anti-quark ($\bar{q}$) grows linearly in the separation of charges. This potential gives a string-like color field configuration. When q and $\bar{q}$ move apart, they lose their energy to the color field. The increasing potential may finally break the string into quark and anti-quark pairs. Intermediate gluons produce transverse "kinks" on the string, resulting in more complicated configurations. The fragmentation continues until a cutoff is reached, and the produced quarks are combined into final-state hadrons. In the cluster model, gluons are forced to split into $q\bar{q}$ pairs at the end of the parton shower. Then the color singlet clusters are formed by $q\bar{q}$ pairs after the parton shower, which subsequently decay into hadrons following flavor conservation.

2.2 Top Quark Physics

The top quark was first discovered by CDF and DØ at the Tevatron proton anti-proton ($p\bar{p}$) collider in 1995 [4][5]. The current world average of the measured top quark mass is

$m_t = 173.5 \pm 1.0$ GeV [8], which is by far the heaviest of all known elementary particle masses. Through the precise measurements of top quark productions and properties, there are many ways to stringently test the SM and probe for new physics. For example, the lifetime of top quark is too short to form hadrons, allowing for the study of essentially bare quarks. The Yukawa coupling of top quark is around one, therefore, electroweak observables with quantum loop corrections are sensitive to top quark mass, i.e. precision measurements of top quark mass and W boson mass provides a better constraint on the Higgs mass than other observables. The top quark production cross sections and distributions are potentially sensitive to exotic intermediate heavy states, as new gauge boson may have strong coupling to the top quark.

2.2.1 Top Quark Pair Production

Top quark pairs ($t\bar{t}$) are produced via strong interactions at hadron colliders. Fig. 2.3 shows the leading order (LO) Feynman diagrams of $t\bar{t}$ production.

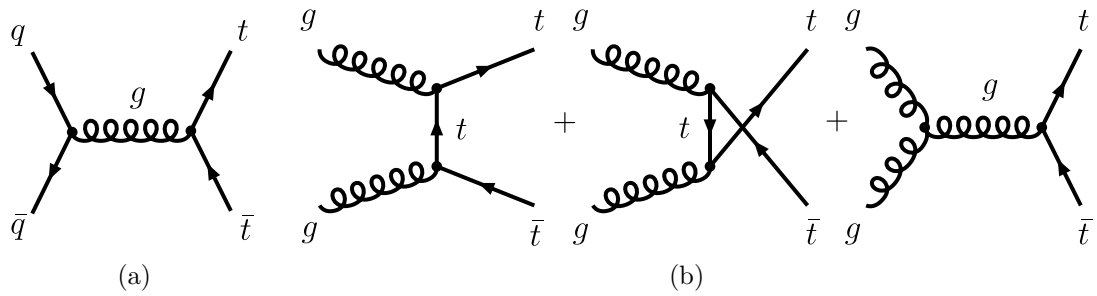

Figure 2.3: The LO Feynman diagrams of top quark pair production in: 2.3(a) quark and anti-quark annihilation and 2.3(b) gluon-gluon fusion.

Based on the QCD factorization theorem [24][25], a general cross section can be separated (factorized) into a perturbative QCD calculable parton level cross section and a long-distance effects which are determined by experiments. Theoretically, the $t\bar{t}$ production

cross section is calculated as the convolution of parton distribution functions (PDF) for the colliding protons (A and B) and the hard scattering parton cross section $\hat{\sigma}_{a+b\to t\bar{t}}$

$$\sigma_{A+B\to t\bar{t}}(\sqrt{s}, m_t) = \sum_{a,b=q,\bar{q},g} \int \hat{\sigma}_{a+b\to t\bar{t}}(\hat{s}, \mu_R^2, \mu_F^2, m_t) f_a^A(x_a, \mu_F^2) f_b^B(x_b, \mu_F^2) dx_a dx_b, \quad (2.24)$$

where two arbitrary scales for renormalization and factorization are μ_R and μ_F respectively, PDF $f_i^h(x_i, \mu_F^2)$ describes the probability density for a parton of type i carrying x_i a momentum fraction x_i of hadron h, $\hat{\sigma}_{a+b\to t\bar{t}}$ is the short-distance (hard) scattering cross section of partons a and b, and $\hat{s} = x_a x_b s$ with a minimum value of $(2m_t)^2$ in order to produce top quark pairs.

μ_R and μ_F are usually set to the typical momentum scale Q of the hard processes $\mu_F^2 = \mu_R^2 = Q^2$, such as the transverse momentum of produced particles, the mass of produced particles or a sum of them. Both scales appear at any fixed order in the perturbative expansion when calculating $\hat{\sigma}_{a+b\to t\bar{t}}$. It thus leads to a systematic uncertainty from the choice of Q^2 which will be discussed in Section. 5.2. PDFs cannot be calculated perturbatively from first principles. They are determined by applying a global fit on a variety of data taken from different experiments, i.e. measurements of the structure functions in deep lepton-hadron inelastic scattering and in lepton pair production in hadron-hadron collisions. The evolution of PDFs with scale μ_F is predicted by DGLAP equation [26], therefore, DGLAP is used to "run" PDFs from one perturbative scale to another scale.

CTEQ[27] and MSTW[28] are the main groups in performing PDF parameterization. Fig. 2.4 shows parton distributions within protons with $Q^2 = (m_t)^2 = (170\ \text{GeV})^2$, and their corresponding uncertainties. The gluon density starts to go beyond the quark densities near $x = 0.1$. If we assume $x_a = x_b = x$ for $t\bar{t}$ production threshold $\hat{s} = x^2 s = (2m_t)^2$,

then the momentum fraction x is shown in the following equation [29],

$$x = \sqrt{\frac{\hat{s}}{s}} = \frac{2m_t}{\sqrt{s}} = \begin{cases} 0.176 & \text{Tevatron Run II, } \sqrt{s} = 1.96 \text{ TeV} \\ 0.05 & \text{LHC } \sqrt{s} = 7 \text{ TeV} \\ 0.025 & \text{LHC } \sqrt{s} = 14 \text{ TeV} \end{cases} \tag{2.25}$$

Eq. 2.25 indicates that $t\bar{t}$ are produced mainly by quark and anti-quark annihilation (Fig. 2.3(a)) at the Tevatron. While at LHC 80% of $t\bar{t}$ are produced by gluon-gluon fusion (Fig. 2.3(b)) at $\sqrt{s} = 7$ TeV. This contribution rises to 90% at $\sqrt{s} = 14$ TeV.

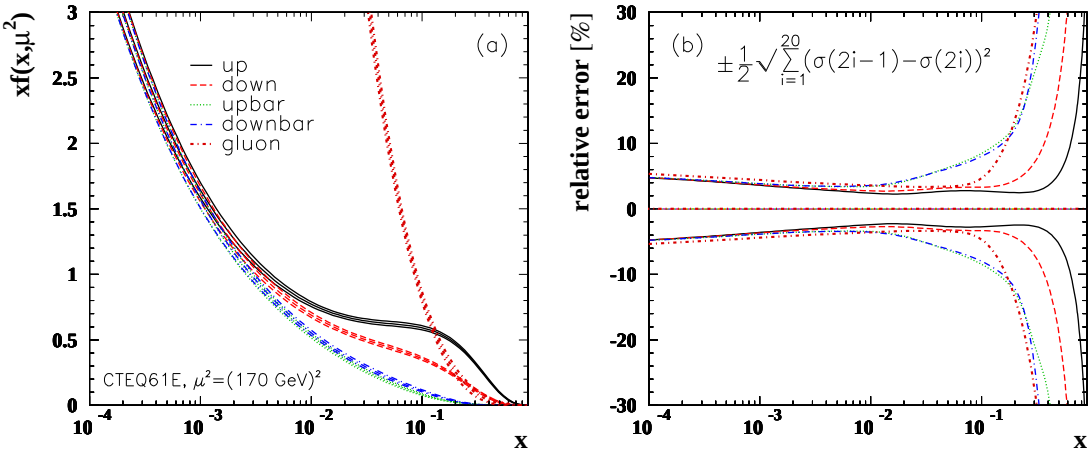

Figure 2.4: Parton distribution functions from CTEQ61 with their uncertainty bands for $Q^2 = (170 \text{ GeV})^2$ (left), and relative uncertainties on PDFs shown in the left plot, taken from [29].

The differential parton level cross section of $2 \to 2$ process is

$$d\hat{\sigma}_{a+b\to t\bar{t}} = \frac{d^3p_3}{(2\pi)^3 2E_3} \frac{d^3p_4}{(2\pi)^3 2E_4} \frac{(2\pi)^4 \delta^4(p_1 + p_2 - p_3 - p_4)}{2(p_1 + p_2)^2} \overline{\sum} |\mathcal{M}_{a+b\to t\bar{t}}|^2 , \tag{2.26}$$

where p_1 and p_2 (p_3 and p_4) are four-momentum of incoming (outgoing) partons, and the LO matrix elements after color and spin average are given in [30]:

$$\overline{\sum} |\mathcal{M}(q\bar{q} \to t\bar{t})|^2 = (4\pi\alpha_s)^2 \frac{4}{9} \left(\tau_1^2 + \tau_2^2 + \frac{\rho}{2}\right) \tag{2.27}$$

$$\overline{\sum} |\mathcal{M}(gg \to t\bar{t})|^2 = (4\pi\alpha_s)^2 \left(\frac{1}{6\tau_1\tau_2} - \frac{3}{8}\right) \left(\tau_1^2 + \tau_2^2 + \frac{\rho}{2} - \frac{\rho^2}{4\tau_1\tau_2}\right) , \tag{2.28}$$

where $\tau_1 = 2\frac{(p_1 \cdot p_3)}{(p_1+p_2)^2}$, $\tau_2 = 2\frac{(p_2 \cdot p_3)}{(p_1+p_2)^2}$ and $\rho = \frac{4m_t^2}{(p_1+p_2)^2}$. Then hard scattering cross sections in the limit of $\hat{s} \to \infty$ ($\hat{s} = (p_1+p_2)^2$) are

$$\hat{\sigma}(q\bar{q} \to t\bar{t}) \propto \frac{1}{\hat{s}}, \tag{2.29}$$

$$\hat{\sigma}(gg \to t\bar{t}) \propto \frac{1}{\hat{s}}\left(\frac{1}{\beta}\log\frac{1+\beta}{1-\beta} - 2\right), \tag{2.30}$$

where $\beta = \sqrt{1-4m_t^2/\hat{s}}$. Notice that at large $\hat{s}$ the $q\bar{q}$ annihilation vanishes more quickly than gg fusion, which confirms the dominance of gg fusion in $t\bar{t}$ production at LHC. The theoretical $t\bar{t}$ production cross section used in this thesis is listed in Tab. 5.1 of Section 5.2.

2.2.2 Top Quark Decay

Due to the GIM (Glashow-Iliopoulos-Maiani) mechanism, flavor changing neutral currents are suppressed. The top quark must hence decay through the weak charged currents. The LO partial widths are given in [31][32]:

$$\Gamma(t \to W^+ q) = \frac{G_F m_t^3}{8\sqrt{2}\pi}|V_{tq}|^2\left(1-\frac{m_W^2}{m_t^2}\right)^2\left(1+2\frac{m_W^2}{m_t^2}\right), \tag{2.31}$$

where G_F is Fermi constant, and V_{tq} is CKM matrix element. V_{tb} is $0.999146^{+0.000021}_{-0.000046}$ by global fits [8], together with the unitary assumption $|V_{tb}|^2 + |V_{ts}|^2 + |V_{td}|^2 = 1$, it can be concluded that top quark decays nearly 100% to a W boson and a bottom quark. If we use $m_t = 172$ GeV and $m_W = 80.4$ GeV in Eq. 2.31, $\Gamma(t \to W^+ b))$ is around 1.5 GeV corresponding to a lifetime of 0.5×10^{-24} s. Compared with time scale of hadronization which is $\Lambda_{\mathrm{QCD}}^{-1} \sim 1/200$ MeV$^{-1} \sim 10^{-23}$ s, top quarks, top quark lifetime is so short that it decays before forming any top-flavored hadrons or $t\bar{t}$-quarkonium-bound states [33].

Top pair events are categorized solely according to the decay products of the two W bosons, each of which has either leptons or quark pairs in the final state. There are three

decay channels: i) "di-leptons" where both W bosons decay into leptons and corresponding neutrinos, ii) "lepton+jets" where one W decays into a lepton pair and the other one decays into a quark pair iii) "all jets" where both W bosons decay hadronically. Fig. 2.5 shows all the decay modes and their approximate branching ratios. The "golden channel" in $t\bar{t}$ cross

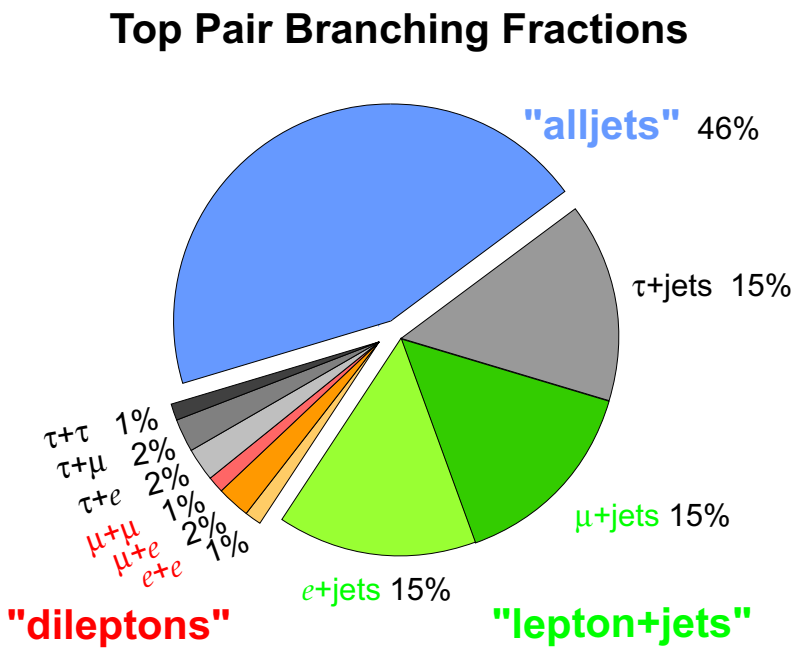

Figure 2.5: Top pair decay channels and the corresponding branching ratios, taken from [34].

section measurement is "lepton+jets" with lepton denoting e or μ. Such events are easier to trigger due to the lepton's high p_T and isolation, and the efficient and pure lepton selection can be employed to reject backgrounds. Moreover, this channel possesses a moderate branching ratio, leading to high statistics. At the LHC, the lower statistics of "dileptons" channel is compensated by a high luminosity, and thus also provides a precise measurement.

2.3 Motivation

The LHC is a top factory due to a large production cross section and high luminosity. The nature of the top quark can be measured to an excellent precision. My motivation to study the $t\bar{t}$ production arises because: i) the measurement of $t\bar{t}$ cross section allows a stringent test of perturbative QCD calculation at the LHC energy scale; ii) the differential cross section of $t\bar{t}$ with respect to jet multiplicity is particularly sensitive to initial state radiation (ISR). Such measurements can be compared with different MC generators in order to test our understanding of ISR.

Moreover, both the inclusive and differential cross sections of $t\bar{t}$ events are very sensitive to new physics that can get an extra contribution from anomalous $t\bar{t}$ production or lead to different cross section values for different top decay channels. For example, a heavy resonance Z' can strongly couple to top quarks and thus enhance $t\bar{t}$ production. The decay channel $t \to H^+ b$ would change the $t\bar{t}$ cross section in various channels because decay modes of a charged Higgs [35] depend on the ratio of the vacuum expectation values of the two Higgs doublets. Many models with R-parity violation predict $t\bar{t}$-like final states associated with extra jets which leads to an inflation in higher jet multiplicity e.g. $pp \to \tilde{g}\tilde{g} \to (t\tilde{t}^*)(\bar{t}\tilde{t}) \to t\bar{t} + jjjj$ [36] (j denotes jets). Last but not least, top pair events often constitute a major background for Higgs searches, and it is important to accurately estimate their production rate from data.

CHAPTER 3

The CMS Detector at the LHC

LHC, a superconducting hadron accelerator, is designed for probing new physics at the TeV energy scale. In its early running period, 2010-2011, the center of mass energy was 7 TeV. Four detectors are installed around the interaction points to observe the collisions. ATLAS and CMS are two general purpose detectors designed for Higgs boson and new physics searches. LHCb (LHC beauty experiment) studies bottom quark physics. ALICE (An LHC Heavy Ion Experiment) performs studies of the quark-gluon plasma. Data up to 5 fb^{-1}, used for the analysis in this thesis, is collected at $\sqrt{s} = 7$ TeV with the CMS detector in the 2011 run. This chapter summarizes the experimental setup. It begins with a description of LHC complex in Section 3.1, then it is followed by a concise overview of the CMS experiment in Section 3.2. Finally, the main features of the CMS trigger are summarized in Section 3.3.

3.1 Large Hadron Collider (LHC)

LHC is a 26.7 km circumference synchrotron proton-proton collider. It is hosted in a tunnel of 3.8 m diameter, 45 m to 170 m below the ground at European Organisation for Nuclear Research (CERN), near Geneva, Switzerland. LHC is designed to reach a nominal 14 TeV centre of mass energy (7 TeV per beam) with a peak instantaneous luminosity of 10^{34} $cm^{-2}s^{-1}$. This high luminosity is achieved by high frequency bunch crossings and a large number of protons per bunch.

The proton acceleration is completed in several stages in different accelerators. The chain of the CERN accelerator complex is shown in Fig. 3.1. Protons, produced by removing electrons from hydrogen atoms, are first accelerated in bunches to an energy of 50 MeV in a linear accelerator LINAC2. The beam, made of proton bunches, is then transferred to the Proton Synchrotron Booster (PSB) and accelerated to 1.4 GeV. Afterwards, the Proton Synchrotron (PS) accelerates six "booster" bunches to 25 GeV, and injects them into the Super Proton Synchrotron (SPS) including an abort gap that gives kicker magnets time to ramp (down) for beam injection (dumping). In SPS, their energy is further increased to 450 GeV. The proton beam are finally injected to the LHC ring, which has a capacity of 3564 bunches per beam. Due to the injection scheme and the properties of the dump system [37], each beam consists of 2808 bunches, each of which contains up to 10^{11} protons.

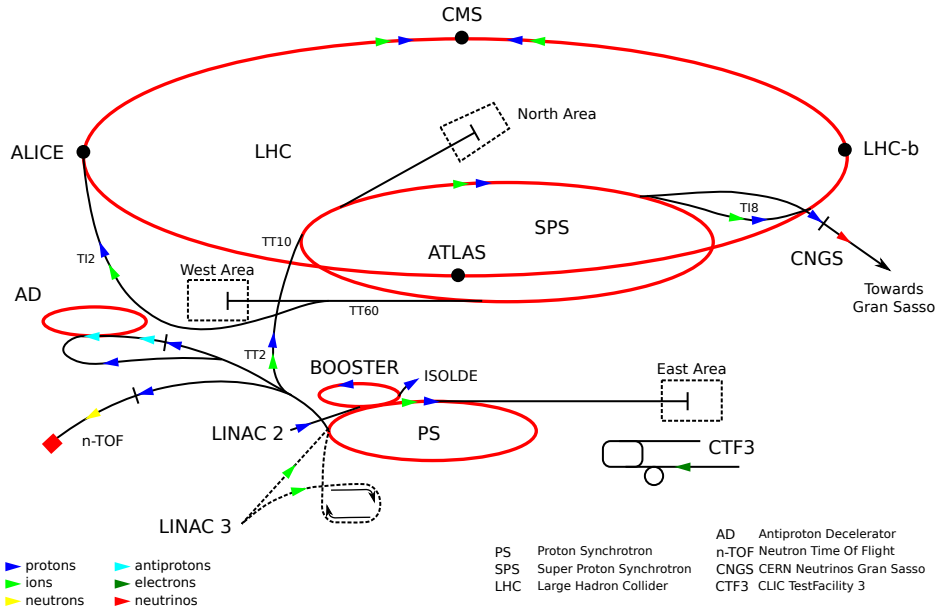

Figure 3.1: The CERN accelerator complex [38].

Inside the LHC, two independent beams are accelerated in two storage rings. 1232 dipole magnets, operated at a temperature below 2 K, provide a magnetic field of 8.3 T and bend the beams along the LHC ring. 858 quadruple magnets keep the beams focused in

order to maximize the possible number of collisions at the intersection points, where two beams cross. Bunch crossings are designed to happen every 25 ns, during the 2011 run they happened every 50 ns.

In addition to the center of mass energy, the instantaneous luminosity $\mathcal{L}$ delivered by the LHC machine is another important parameter, since the production rate of collision events is proportional to it, $\frac{dN}{dt} = \mathcal{L}\sigma$, where σ is the event production cross section. The LHC instantaneous luminosity depends on the proton beam parameters. By assuming a Gaussian distribution of the beam particles inside a bunch, it can expressed as [37][39]:

$$\mathcal{L} = \frac{N_b^2 n_b f \gamma}{4\pi\epsilon_n \beta^*} F, \tag{3.1}$$

where N_b is the number of protons per bunch, n_b is the number of bunches per beam, f is the revolution frequency, γ is the relativistic gamma factor, ϵ_n is the normalized transverse beam emittance, β^* is value of the beta function at the collision point, and F is the geometric luminosity reduction factor due to the crossing angle at the collision point. ϵ_n and β^* together describe the transverse movement of the beam particles, both of which have units of length. ϵ_n measures the spread of proton in position and in momentum phase space, which is the products of the RMS of particle position distribution and the RMS of the particle momenta distribution. It is determined by the initial conditions in SPS, and is a constant during the beam life. β^* describes the beam focusing, which can be reduced along the ring.

The instantaneous luminosity decreases throughout a given LHC fill due to several effects, such as the loss of particles in collisions, a slow emittance blow-up caused by the scattering of particles on residual gas and Touschek scattering[1] [40][41]. Thus a

[1] Touschek scattering describes a collision of two electrons inside a bunch with transfer of transverse momentum into longitudinal momentum. A large change in momentum can lead to the energy deviation of particles becoming larger than the energy acceptance of the ring, in which case the particles will be lost.

luminosity lifetime τ_L is introduced to account for the degradation, and is defined as the time for the luminosity dropping to $1/e$ of its peak. The average design luminosity lifetime for LHC is ~ 15 hours. Then the integrated luminosity L over the run time is $L = \mathcal{L}_0 \tau_L \left(1 - \exp\left(-T_{\text{run}}/\tau_L\right)\right)$, where $\mathcal{L}_0$ is the initial peak luminosity and T_{run} is the run time.

In 2011, data-taking started in the middle of March and finished at the end of October. Tab. 3.1 summarizes the typical machine parameters [42]. LHC delivered a total integrated luminosity of 6.13 fb^{-1} for experiments. CMS removed a small fraction of data which are taken in bad detector conditions, it recorded an amount of 5.55 fb^{-1} of data in 2011, as shown in Fig. 3.2[43].

Table 3.1: LHC machine parameters for a typical late 2011 proton-proton run, and design parameters at 14 TeV in the centre of mass [42].

Parameter	Unit	2011	Nominal
Beam energy	TeV	3.5	7
Dipole Field	T	4.17	8.33
Lorentz factor γ		3730	7461
Revolution Frequency f	Hz	11.25	11.25
Protons per bunch N_b	10^{11}	1.5	1.15
Bunch per beam n_b		1380	2808
Bunch separation	ns	50	25
normalised transverse emittance ϵ_n	μm	$1.9 - 2.3$	3.75
β^* at collision point	m	1	0.55
Instantaneous peak luminosity $\mathcal{L}$	cm^{-2}s^{-1}	3.6×10^{33}	10^{34}

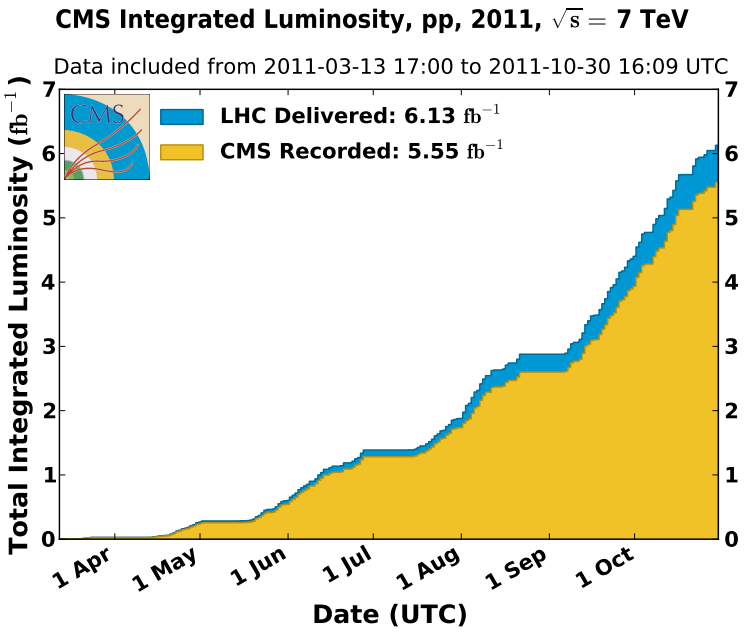

Figure 3.2: Total integrated luminosity delivered by the LHC and recorded by the CMS during the 2011 *pp* collisions running [43].

3.2 Compact Muon Solenoid (CMS)

The CMS detector is cylindrically symmetric along the beam axis, with a length of 21.6 m, a diameter of 14.6 m and a total weight of 12500 tons. A main feature of CMS is its superconducting solenoid. It provides a nearly homogeneous magnetic field of 3.8 T inside and a return field of 2 T in the muon system, which allows for the muon p_T measurement with a precision of 10% or better for 1 TeV muons. Inside the solenoid, there are the tracking system, the electromagnetic calorimeter (ECAL) and the hadron calorimeter (HCAL). The muon spectrometer is hosted by the iron return yoke of the magnet. Fig. 3.3[44] shows schematic view of CMS.

CMS adopts a right-handed coordinate system using the collision point as its origin. The x-axis points radially inward to the center of the LHC ring, y-axis vertically upwards, and the z-axis along the direction of the beam line. The azimuthal angle ϕ is measured

with respect to the x-axis, and the polar angle θ is measured from the z -axis. The pseudorapidity is defined as $\eta \equiv -\ln\tan(\theta/2)$, and is preferred over θ because it is nearly invariant under lorentz boosts along the beam axis[2]. Accordingly the angular distance is $\Delta R = \sqrt{\Delta\eta^2 + \Delta\phi^2}$. In the following sections, the sub-detectors will be briefly described.

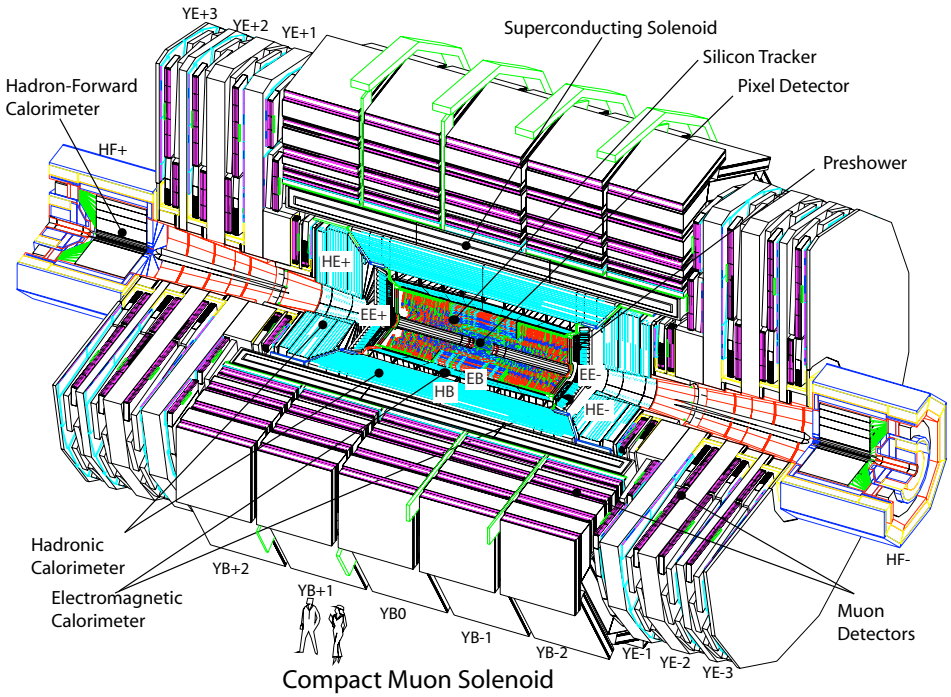

Figure 3.3: General view of the CMS detector [44].

3.2.1 Silicon Tracking System

The CMS tracking system is dedicated to reconstructing the trajectories and momenta of charged particles, as well as primary and secondary vertices. It is closest to the beam line and experiences a high flux of charged particles, where an average of 1000 particles from pp collisions traverse the tracker every bunch crossing (25 ns) at the nominal luminosity. The

[2]The rapidity y is a "lorentz invariant". In LHC the mass of a particle is negligible compared with its energy, thus η is a very close approximation to y.

tracking system is thus required to have a high granularity (or a low cell occupancy) to ensure a good spatial resolution for trajectories, a fast response to resolve the high frequencies of the bunch crossing, and to be radiation hard. These requirements motivated CMS to build an all-silicon tracking system. It consists of a pixel detector and a silicon strip tracker with a total length of 5.8 m and a diameter of 2.5 m, illustrated in Fig. 3.4[45]. To minimize the radiation damage for silicon sensors, both detectors are operated at a working temperature of -10 °C. Moreover, the material budget[3] degrades the track reconstruction due to the multiple scattering, bremsstrahlung, photon conversion and nuclear interactions. Therefore in the tracking system design, the material budget is minimized in order to limit these effects.

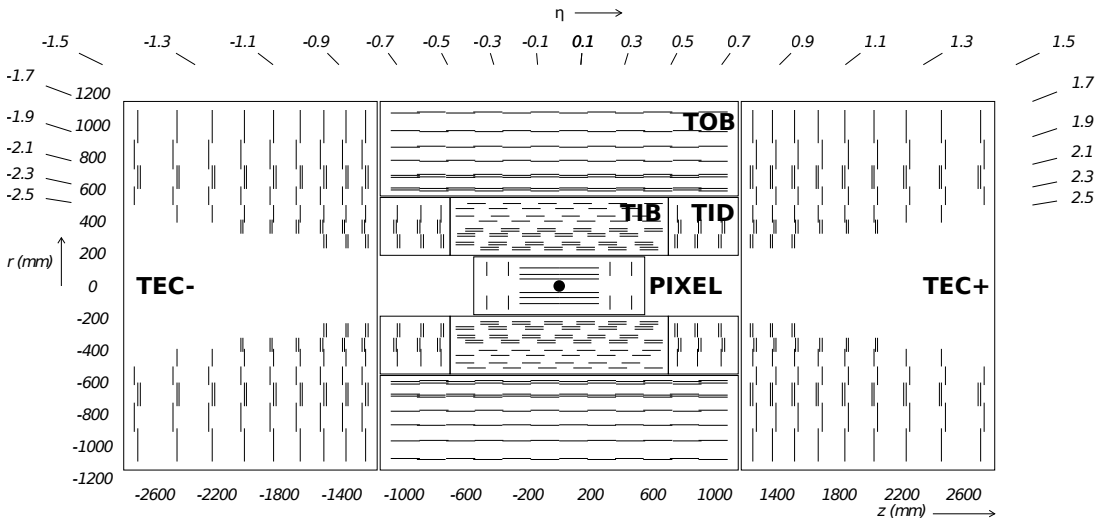

Figure 3.4: $r-z$ slice of the CMS tracking system, taken from[45]. The pixel and silicon strip tracker are illustrated by lines. Four components of CMS tracker are shown, which are Tracker Inner Barrel and Disc (TIB, TID), Tracker Outer Barrel and End Cap (TOB, TEC).

[3]The material budget includes a high density of on-detector electronics and cables/pipes of the readout and cooling system.

3.2.1.1 Pixel Detector

The innermost pixel detector, shown in Fig. 3.5, provides a fine granularity to precisely reconstruct charged tracks in three-dimension. It allows for track seeding of charged particles, vertex finding and flavor tagging. Three barrel layers are placed at radii of 4.4, 7.3, and 10.3 cm, each of which has a length of 53 cm; two endcap disks are placed on each side of the barrel at $z = \pm 34.5$ cm and $z = \pm 46.5$ cm with radii of 6 cm and 15 cm respectively. The blades of the endcap disks are tilted by 20 degrees with respect to the disk plane in order to induce charge sharing. The hit resolution is ~ 20 μm in the $r - \phi$ plane and ~ 30 μm in the z direction [46]. In the following, the pixel detector and data aquisition software is described in detail, since it constitutes the detector work which was done as part of my thesis work.

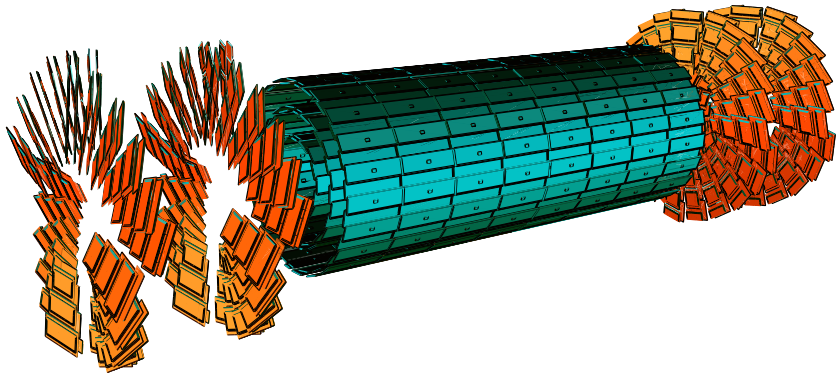

Figure 3.5: Schematic view of CMS pixel detector, taken from [47].

The building blocks are 1440 pixel modules, all together containing 66 million silicon sensors. There are 672 modules and 96 half-modules in the barrel part. As shown in Fig. 3.6(a), the main components of a barrel model are:

- 4160 silicon sensors (pixel): A pixel is formed by high dose n-implants introduced into a highly resistive n-substrate [44]. Its sensitive thickness is 295 μm, and the size

is 100×150 μm^2 in the $r - \phi$ plane. The resulting occupancy is in the order of 10^{-4} per pixel, low enough for an efficient tracking system.

- 8 (half model) or 16 (full model) readout chips (ROCs): A ROC is organized in 26 double columns of 2×80 pixel unit cells (PUC), each of which is bump bonded to one pixel. Each double column has a periphery equipped with time stamp buffers and data buffers. The peripheries control the readout and perform trigger validation. Fig. 3.6(b) shows the layout of a ROC.

- a High Density Interconnect (HDI):
  HDI are responsible for sending clock/trigger signals and voltages to all ROCs.

- a Token Bit Manager (TBM) chip:
  TBM coordinates the communication of a group of 8 or 24 ROCs.

The endcap disks consist of 672 detector modules called plaquettes. The plaquette has the similar components as the barrel model, but is manufactured in 5 different sizes in order to cover the trapezoidal panels without leaving cracks.

The readout chain, shown in Fig. 3.7(a), starts in the pixel. When a charged particle hits a pixel, the collected ionisation charge will induces a voltage signal in the PUC. The corresponding double-column periphery is notified once the amplified signal exceeds a programmable threshold. The address and analog signal of each hit pixel are transferred and stored in the data buffers, and the time information are stored in the time buffers. For each incoming Level-1 trigger (explained in Section 3.3), a token bit controlled by the TBM is passed on from one ROC to the next ROC and finally back to the TBM. TBM collects the information of hits that match the trigger bunch crossing. For each token bit, the TBM adds a header with an event number and a trailer with status information to each readout, as illustrated in Fig. 3.7(b).

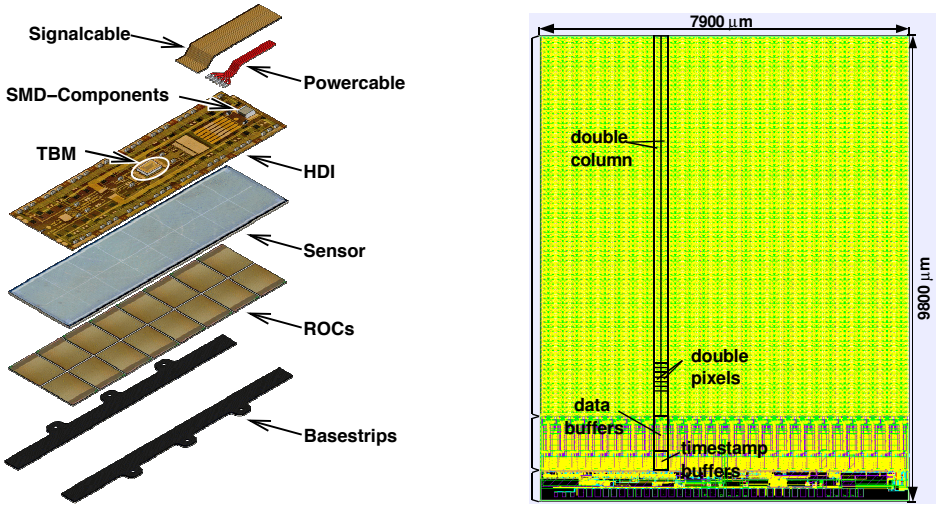

(a) (b)

Figure 3.6: 3.6(a) shows a barrel pixel detector full module, from [48]; and 3.6(b) shows the layout of a ROC with a size of 9.8×7.9 mm^2.

The analog signal from the TBM is translated by the analog optical hybrid (AOH). The optical signals is then transmitted to the off-detector electronics: Front End Drivers (FED) and Front End Controllers (FEC). The FED digitizes the input signals and sends them to the data acquisition system. The FEC sends the clock and trigger information to the front-ends, and also programs the TBM and ROCs over a fiber optic connection. The I2C protocol [51] is adopted by FECs for communication with the front-ends, which is fast to download the pixel thresholds. The Timing Trigger and Control (TTC) system is used to distribute the clock and trigger signals to all detector components.

During the data taking, the pixel online software (POS) controls and monitors the hardware of the pixel detector, as well as performs the online calibrations. The POS is a composition of the software tools, and is operated on a cross-platform framework called XDAQ. XDAQ is written in C++ and incorporates a web-server executable that allows the control and monitor the XDAQ-based application over the world wide web at the runtime [52].

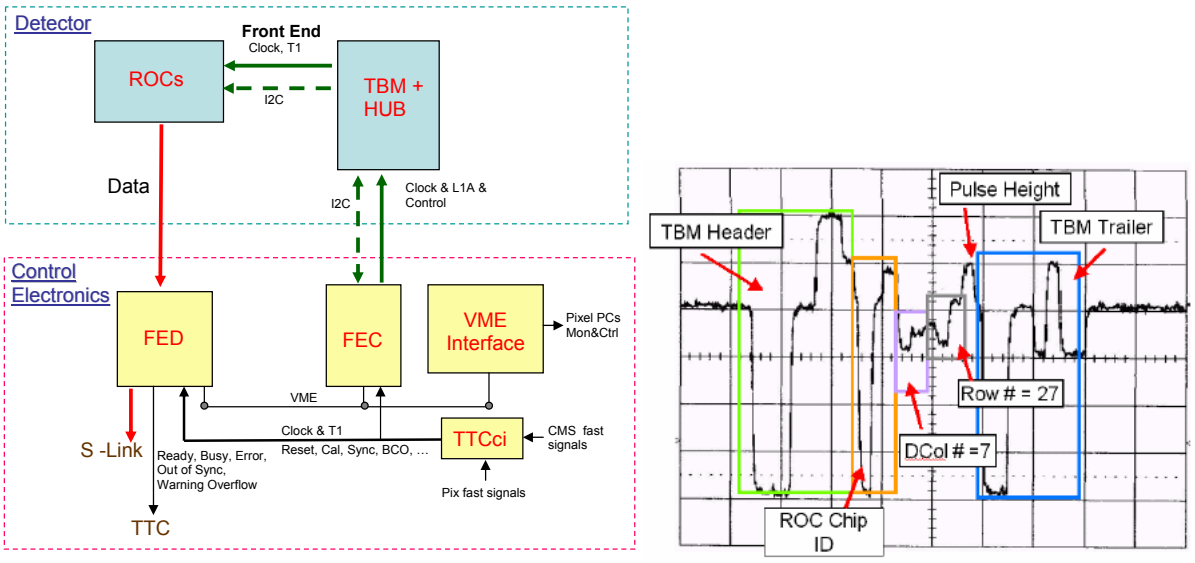

(a) (b)

Figure 3.7: 3.7(a) is a schematic diagram of the pixel readout system integrated to the CMS data acquisition system, taken from [49]. 3.7(b) is a analog data signal read from a single ROC, taken from [50].

The POS is built from a number of different applications called supervisors, and the architecture is shown in Fig. 3.8. The top level supervisor `PixelSupervisor` has two major functions. First, it receives requests from the CMS Run Control System (RCMS) and transforms these commands to the sub-systems like pixel FED and FEC via the SOAP (Simple Object Access Protocol) message. Such communication is mediated by a java application called Pixel Function Manager (PFM). PFM implements the finite state machine[4] and thus be able to carry out the task needed in state transitions of the run control. Another function is to coordinate the sub-level supervisors via sending SOAP messages, particularly during the detector configuration and calibration. The sub-level supervisors `PixelFEDSupervisor`, `PixelFECSupervisor` and `PixelTTCSupervisor` act as

[4]The finite state machine is a mathematical model of computation. It is conceived as an abstract machine that can be in one of a finite number of states i.e., starting, pausing, stopping, recovering in POS.

the interface for FED, FEC and TTC to communicate with the front-end electronics on the pixel detector respectively.

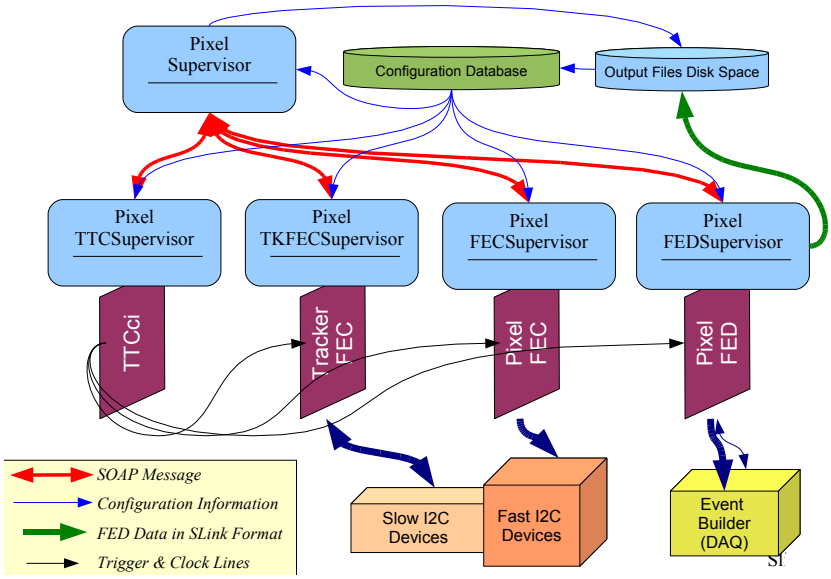

Figure 3.8: Scheme of the pixel online software architecture shows the dependencies among the supervisors, taken from [53].

The POS is mainly responsible for i) the hardware configuration during the run time and ii) the online calibrations, both of which are important in preparing the detector for operation. The configuration of the detector starts with a global key. The key encodes the set of configuration data which is encapsulated in 15 configuration data objects (C++ class). For examples, `PixelROCStatus` keeps track of the status of the ROCs and `PixelFEDConCard` stores the setting for one FED, etc., detailed in [54]. The design of these objects is to ensure a fast and reliable configuration, and to achieve an efficient way in data packaging. Configuration data is fetched from either the files or the database by an interface class `PixelConfigInterface`, and then is loaded into the detector hardware.

There are a large number of calibrations and the full list of calibrations are documented in [54]. The most fundamental ones are breifly introduced as following:

- Address Levels Calibration: The position of hits is encoded in 6 discrete analog levels from the TBM. This calibration determines the values used by the FED for decoding the hit address. The values are required to be near the intended levels and clearly separated from other levels. Fig. 3.9(a) shows the address levels of all pixels in a ROC received by the FED.

- "S-Curve" Calibration: The detection thresholds and noise of a pixel are important parameters as they affect the hit position resolution. This calibration measures the threshold and noise of a pixel by checking its response efficiency as a function of injected test charge (VCAL). The threshold is the VCAL value where signal shows 50% efficiency and noise is the width of the turn on range, as shown in Fig. 3.9(b)

- Gain Calibration: The signal response of a pixel is described by the pulse height which is measured in the ADC units. This calibration relates the amount of charge with the analog signal by studying the gain curve where the pulse height is plotted as a function of the injected test charge, as seen in Fig. 3.9(c). A plateau in the high signal region indicates the saturation in the amplifier. The gain curve is then fitted by a linear function to quantify the pulse height in the amount of charges.

The following is a detailed description of some of the POS development done during my Ph.D. 1) Addition of a tree structure to the calibrations. This was done to be able to view some important information directly via the Histoviewer application in the web browser. Two TTree[5] pointers (tree and tree_sum) are used to store the information of "pass"[6] and the summary information of calibrations. The implementation of this tree structure is to declare a C++ struct in the header file of each kind of the calibration class. In the struct

[5]TTree is a data structure defined the in ROOT package. As its name implies, it consists a list of independent branches. Each branch has its own buffer for data storing and retrieving.

[6]"pass" represents the valid condition of a calibration. The meaning of such condition is different for different calibrations, detailed in [54].

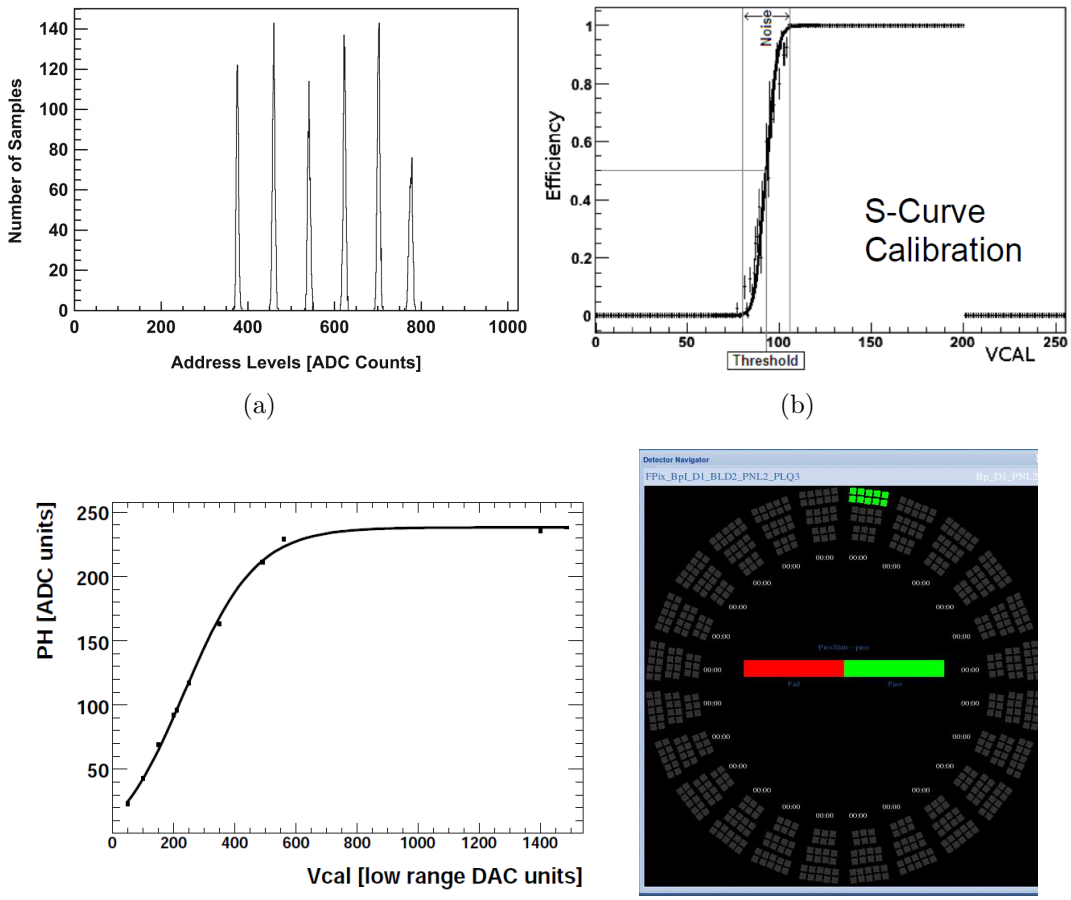

(a) (b)

(c) (d)

Figure 3.9: 3.9(a) is the distribution of address levels, 3.9(b) is the S-Curve marked with the turn-on region, and 3.9(c) is the gain curve, all of which are taken from [52]. 3.9(d) shows the pass information of ROCUBEqualization calibration of a forward pixel, viewed by the histoviewer application.

there is an array to store each ROC's name. It ensures that all the information can be viewed by Histoviewer. When using Histoviewer, the Detector Navigator view of HistoViewer provides a graphical view of the detector, as illustrated Fig. 3.9(d). This example shows the ROCs on a forward plaquette pass the ROCUBEqualization calibration which sets the ultrablack level of each ROC equal to the corresponding TBM's ultrablack level.

2) Development of a package called `Pixelb2inCommander` for sending b2in messages among supervisors. In SOAP message exchange, the calling thread of execution is blocked during the time of requesting. It means that only one message can be sent to one target application at one time. On the other hand, the b2in message exchange can be operated in parallel. It allows the host (one supervisor) to send several messages to different clients (target supervisors) and thus improve the efficiency of communication. This package is preferred when it comes to efficiency critical operation.

The message is stored in a parameter array and associated with a message ID. In the sender's side, there are three methods. `Pixelb2inCommander::send()` method is responsible for the message sending. It locates the target application and invokes the callback function in the receiver's side by a string variable. When a message is sent, its ID is locked till a return flag is received by the sender, indicating the messages have been received by the clients. `Pixelb2inCommander::waitForReply()` method is used to extract the return flag for a given message ID. Once the reception from the client is confirmed, the message ID is deleted by the `Pixelb2inCommander::removeMsgID()` method. In the receivers side, all b2in messages go into a single callback function. The receiver sends reply to the host by calling `Pixelb2inCommander::sendReply` method, noticing the reception of the message. This package has been tested for most calibrations and committed in the POS.

3.2.1.2 Silicon Strip Tracker

The particle flux is reduced in the outer region of the tracking system, thus allowing the use of a strip detector that has a lower granularity than the pixel detector. The layers of the silicon strip tracker are at the radial region between 20 cm and 116 cm, covering the pseudorapidity region $|\eta| < 2.5$. The detector is divided into four components, as shown in

Fig. 3.4. In the central region with $|z| < 110$ cm, the Tracker Inner Barrel (TIB) and the Tracker Outer Barrel (TOB) are composed of 4 and 6 concentric cylindrical shape layers respectively. The TIB is shorter than TOB, and is complemented by 3 Tracker Inner Disks (TID) at each side. Finally, 9 Tracker End-Cap (TEC) disks cover the forward and backward region with 120 cm $< |z| <$ 280 cm. 15148 detector modules with a total of 24244 sensors are distributed among these four components [55]. Fifteen types of sensors, varying in terms of strip length and pitch, are employed to ensure an occupancy lower than 1% [56]. Modules in the inner region (TIB, TID and four inner layers of TEC) use only one sensor to minimize the channel occupancy. TOB and 3 outer layers of TEC use modules having two silicon sensors with wider pitch, since the detector occupancy decreases along the radial direction. The spatial resolution is around $23 - 53$ μm in the $r - \phi$ plane and about $230 - 530$ μm in the z direction. Together with the pixel detector, the nominal momentum resolution is 0.7% (5.0%) at 1 (1000) GeV in the central region and the impact parameter resolution for high-momentum tracks is typically 10 μm [45].

3.2.2 Electromagnetic Calorimeter

The electromagnetic calorimeter (ECAL) precisely measures the energy of electrons and photons, and performs particle identification (especially the separation between electrons and charged pions). The CMS ECAL is designed to achieve a high energy and angular resolution, and thus to be sensitive to the particle resonances decaying to electromagnetic showers, such as $H \to \gamma\gamma$ decay mode. For this purpose, CMS built a hermetic and homogeneous ECAL, where the shower medium and light producer are the same material. The shower media is lead tungstate ($PbWO_4$) crystals. This choice is based on several considerations[57][58]: the $PbWO_4$ crystal has a fast scintillation response, typically 80% of the light is collected within a bunch crossing (25 ns); its high density (8.28

g/cm^3) and short radiation length[7]($X_0 = 0.89$ cm) allow a compact construction and thus the ECAL can be placed inside the CMS superconducting solenoid; its small Molière Radius[8] ($R_M = 2.19$ cm) ensures an efficient lateral shower containment, and therefore matches a very fine granularity. However, the light yield of $PbWO_4$ is relatively low (~ 30 photons/MeV) hence the photodetector must have a multiplication mechanism. The light yield also varies with the temperature (-2.1% °C^{-1} at 18 °C [59]): the temperature is hence required to be stabilized at 18 °C within 0.05 °C.

The ECAL is divided into a barrel (EB) and two endcaps (EE), the layout is illustrated in Fig. 3.10. EB (EE) is composed of 61200 (14648) taper shaped crystals, Tab.3.2 shows the comparison of crystal's parameters in EB and EE. In order to reduce the effect of cracks between adjacent crystals, crystals in EB (EE) are tilted by 3° ($2° - 8°$) in both η and ϕ with respect to the direction towards the nominal interaction point.

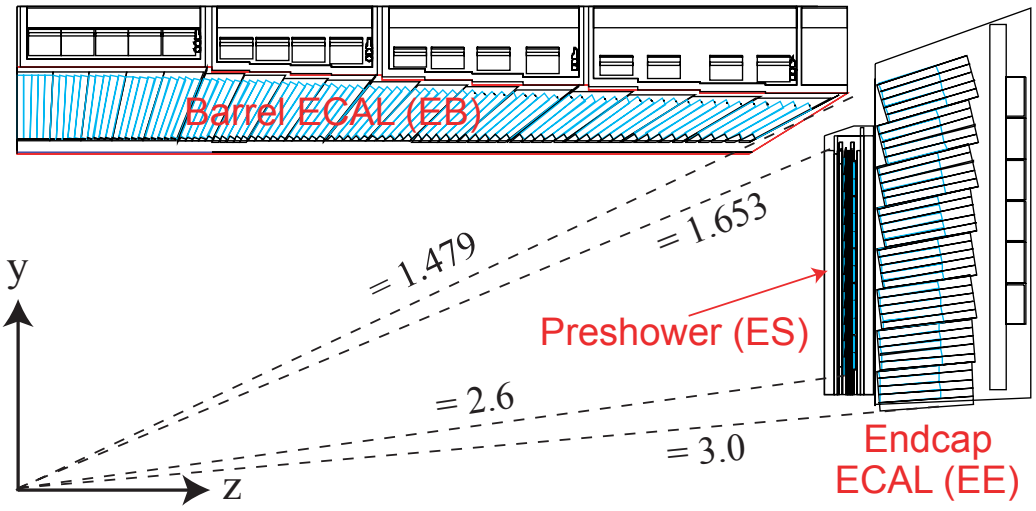

Figure 3.10: A schematic view of the CMS electromagnetic calorimeter (ECAL) in the $r - z$ plane, taken from [47].

[7]The radiation length (X_0) is the distance over which the electron energy is reduced by a factor of $1/e$ due to radiation losses only.

[8]The Molière Radius describes the transverse spreading of electromagnetic showers, defined as $R_M = 21\text{MeV} \cdot X_0/E_c$ where E_c is the electron energy for which ionization matches bremsstrahlung. Typically, the transverse granularity of ECAL is chosen to match R_M.

Table 3.2: The parameters of ECAL crystals in both barrel and endcap, the transverse granularity is corresponding to the front face cross-section.

	ECAL barrel	ECAL endcap
Front face cross-section (mm^2)	22×22	28.62×28.62
Rear face cross-section (mm^2)	26×26	30×30
Length (mm)	230 ($25.8X_0$)	220 ($24.7X_0$)
Arrangment	$\eta - \phi$ grid	$x - y$ grid
Transverse granularity $\Delta\eta \times \Delta\phi$	0.0175×0.0175	down to 0.05×0.05

EB covers the central pseudorapidity rapidity region $|\eta| < 1.479$, positioned at 1.24 m $< r <$ 1.86 m from the interaction point. A 5×2 array of crystals is assembled into an alveolar structure, of which 400 or 500 are mounted into a module[60]. Four modules form a supermodule, covering half of the barrel in η and 20° in ϕ. EB contains a total of 36 supermodules. EE, composed of two semi-circular aluminium plates (Dees), extends the coverage up to $|\eta| < 3$ and situates at 3.154 m from the interaction point. A 5×5 array of crystals forms a supercrystal and is mounted on the Dee. There are a total of 138 supercrystals in EE. The light emitted from the crystals is detected by avalanche photodiodes (APDs) in EB and vacuum phototriodes (VPTs) in EE.

In order to improve the $\gamma - \pi^0$ separation, a 20 cm thick preshower detector (ES) is installed in front of EE, covering $1.653 < |\eta| < 2.6$. This sampling calorimeter has two lead absorbers to initiate electromagnetic showers, each followed by a silicon strip detector for deposited energy measurement. The first (second) lead plane has $2X_0$ ($1X_0$) thickness, which allows 95% of single incident photons to start showering before reaching the second plane.

The ECAL energy resolution is given by

$$\frac{\sigma_E}{E} = \frac{a(\sqrt{\text{GeV}})}{\sqrt{E}} \oplus \frac{\sigma_N(\text{GeV})}{E} \oplus C, \tag{3.2}$$

where the unit of energy is GeV. a describes the stochastic fluctuations in scintillation, limited by photoelectron statistics; σ_N is the noise term from pileup events and electronics noise; and the constant C is mainly related to shower containment limitations, non-uniformities of the longitudinal light collection and the precision of the calibration. In the test beam study, the stochastic, noise, constant terms are measured as 2.8%, 0.415 and 0.3% respectively for electrons of 20 to 250 GeV[61]. At high energies the biggest contribution is from the constant term; the energy resolution thus strongly depends on the calibration. The ECAL calibration is performed with $\pi^0 \to \gamma\gamma$, $W \to e\nu$, and $Z \to ee$ data and achieve a precision of 0.6% in the central barrel [62].

3.2.3 Hadronic Calorimeter

Together with the ECAL, the CMS hadronic calorimeter (HCAL) measures jets and neutrinos/exotic particles resulting in missing transverse energy [47]. It is designed to cover as large an area around the interaction point as possible to measure all energy of an collision and thereby infer $\not{E}_{\mathrm{T}}$; and provide a sufficient containment to stop hadron showers that spread more laterally than electromagnetic showers[9]. The HCAL consists of a set of sampling calorimeters: the central HCAL composed of the barrel (HB) and the edcap (HE), outer (HO) and forward calorimeter (HF), as shown in Fig. 3.11.

The central HCAL (HB and HE) covers a total pseudorapidity range of $|\eta| < 3$, where HB covers $|\eta| < 1.4$ and HE covers down to $|\eta| = 3$. It is installed inside the solenoid. The choice of such placement avoids the performance degradation of the HCAL caused by the long absorption length of the solenoid (one hadron absorption length). Additionally, it also

[9]The hadronic shower developement is similar to the EM shower but more complex. High energy hadrons interact with nuclei producing secondary particles (mostly $\pi^{\pm}$, π^0), which in turn interact with further nuclei or decay. Approximately 1/3 of the pions produced are π^0s decaying to $\pi^0 \to \gamma\gamma$. Thus the cascades have two distinct components: hadronic and electromagnetic component.

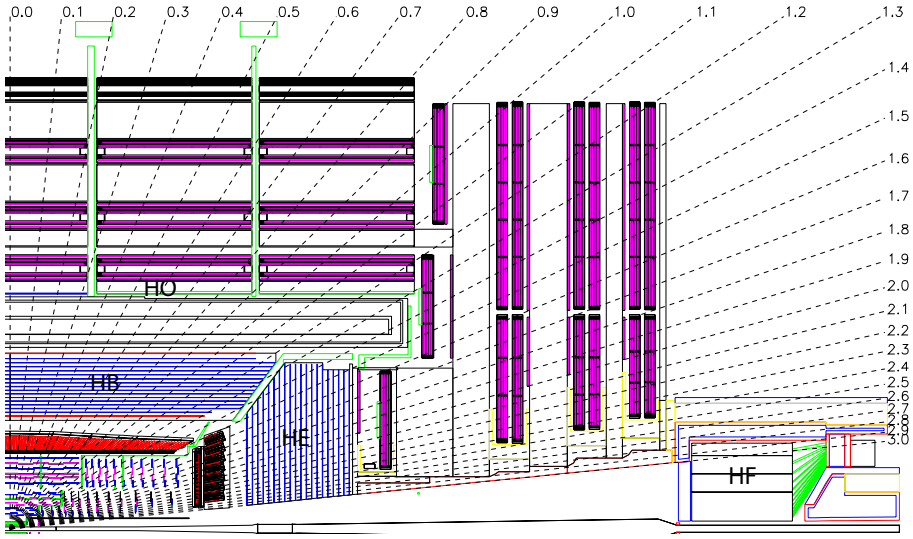

Figure 3.11: Longitudinal view in $r - z$ plane of the hadron barrel (HB), endcap (HE), outer (HO) and forward (HF) calorimeters, taken from [44].

increases the bending distance of muons, leading to a better momentum measurement of muons. Due to the small available space inside the solenoid ($\sim$ 1 m radially), the design aims to maximize the amount of the absorber. Brass (70% Cu and 30% Zn) absorber meets this requirement due to its short interaction length ($\lambda_I = 16.42$ cm)[10], short radiation length ($X_0 = 1.49$ cm), high density (8.53 g/cm^3) and non-magnetic property. Plastic scintillator tiles with embedded wave length shifting (WLS) fibers is chosen as the active medium [44]. The thickness of scintillators is 3.7 mm.

HB is divided into two symmetric cylinders, each of which consists of 18 identical wedges subtending 20° in ϕ. The wedge is made of 14 brass absorber plates parallel to the beam axis, each with a thickness of 5.5 cm, and two steel support layers (the innermost and outermost layer). The plates are interleaved with plastic scintillators, each of which is segmented into 72 and 16 sectors in ϕ and η direction respectively, resulting

[10]Analogy to X_0, the nuclear (interaction) length λ_I defines the fundamental scale of the hadronic shower, which is usually longer than X_0. It is given by $\lambda_I = 1/(n\sigma_{\text{total}})$, where n is the material's number density and σ_{total} is the cross-section of total interactions.

in a granularity of $\Delta\eta \times \Delta\phi = 0.087 \times 0.087$. The effective thickness, in terms of the interaction length, varies along η, which is $5.8\lambda_I$ at $|\eta| = 0$ and $10.6\lambda_I$ at $|\eta| = 1.3$. The ECAL crystals in front of HB adds about $1.1\lambda_I$ of material [44].

Each HE contains 16 wedges using the same absorber plates with a thickness of 7.9 cm and a 9 mm gap in between to insert the scintillators. It has a ϕ segmentation varying from 5° in the lower η regions to 10° in the higher η regions. The granularity $\Delta\eta \times \Delta\phi$ is 0.087×0.087 in the range of $|\eta| < 1.6$ matches the granularity in HB, and degrades to 0.17×0.17 for $|\eta| > 1.6$. The total thickness, including ECAL crystals, is about $10\lambda_I$ [44].

HO, covering $|\eta| < 1.26$, is placed outside the magnet in the barrel region as an additional "tail catcher" to sample the energy from penetrating hadron showers leaking through the rear of the central HCAL [47]. It consists of layers of scintillator with the same granularity as HB. The magnet, used as the additional absorber, contributes an additional $1.4\lambda_I$ thickness. Though the HO is constrained by the muon system, it increases the effective thickness to $11.8\lambda_I$ in the central region.

HF is constructed as a cylinder around the beam axis. It sits at 11.2 m from the interaction point, and extends the coverage to $|\eta| < 5$. In this very forward region, an average energy of 760 GeV is deposited in the detector per pp collision, compared with 100 GeV for the rest of the detector. To deal with this harsh radioactive environment, steel is chosen as an absorber, and radiation hard quartz fibers as the active medium. The material sums up to a total of $\sim 10\lambda_I$ absorption length. The steel absorber is composed of 5 mm thick grooved plates, and the fibers are placed into the grooves. The signal from Cherenkov light is emitted in the quartz and then channeled by the fibers to the photomultipliers. Due to the different responses of electrons and pions, HF uses fibers with two different lengths to distinguish the electromagnetic and hadronic showers. HF is azimuthally divided into 20°

modular wedges. The fibers are parallel to the beam line and bundled to form a granularity of $\Delta\eta \times \Delta\phi = 0.175 \times 0.175$ [44].

The energy resolution in the HCAL is worse than that in the ECAL due to its coarser granularity. Furthermore, hadron showers develop fewer secondary particles than electromagnetic showers, resulting in a larger statistical fluctuations, and sampling calorimeters have a larger stochastic term. The energy resolution of the HCAL has been measured using the test beam data [63][64]. Combined with the ECAL, it is given by

$$\frac{\sigma_E}{E} = \frac{85\%(\sqrt{\text{GeV}})}{\sqrt{E}} \oplus 7.4\%, \quad |\eta| < 3, \tag{3.3}$$

in the forward region, the energy resolution combined with ECAL is

$$\frac{\sigma_E}{E} = \frac{198\%(\sqrt{\text{GeV}})}{\sqrt{E}} \oplus 9.0\%, \quad 3 < |\eta| < 5. \tag{3.4}$$

3.2.4 Magnet

A strong magnetic field ensures a precise measurement of the transverse momentum of charged particles as the transverse momentum resolution depends on the magnetic field strength B and its length L: $\frac{\delta p}{p} \propto \frac{p}{BL^2}$. CMS chose a compact configuration but with a strong and uniform field strength of 3.8 T[11]. The magnet system consists of a superconducting solenoid and an iron return yoke. The superconducting solenoid has a length of 12.5 m, a diameter of 6 m and weights about 12,000 tonnes. It is housed in a vacuum cylinder and maintained at liquid helium temperatures ($\sim$ 4K). It utilizes 4 layers of winding made from a high-purity aluminium-stabilised NbTi conductor with a 18 kA current follow. The yoke, composed of 5 wheels and 2 endcaps each with 3 disks, preserves the residual magnetic field of 1.8 T in the central region. The return field is then used to curve the muons in the muon system for the measurement of muon momentum.

[11] Atlas is a bigger detector with a moderate magnetic field (2 T).

3.2.5 Muon System

Muon detection is important for CMS, as muons are present in many final states of Higgs boson decay or new physics. They can penetrate several meters of material and deposit only little ionizing energy[12], and thus cannot be stopped in any of CMS calorimeters. Therefore, the muon spectrometer is placed outside the magnet and embedded in the iron yoke such that the muon p_T measurement can benefit from the returned magnetic field. Its main purpose is to identify muons, precisely measure the momentum and charges of muons , and provide muon triggering. Due to the different radiation environments, the CMS muon system is organized into three types of gaseous detectors: the drift tube (DT) chambers in the barrel covering $|\eta|$ <1.2, the cathode strip chambers (CSCs) in the endcap covering $0.9 < |\eta| < 2.4$ and the resistive plate chambers (RPCs)in both barrel and endcap dedicated to triggering, as shown in Fig. 3.12.

DT chambers are used in the barrel due to the low hit occupancy (< 10 Hz/cm^2) and the low return magnetic field in this region. The barrel muon detector is installed on five wheels of the iron yoke, each with a length of ~ 2.5 m along the z axis. A wheel is organized into four concentric cylinder stations labeled as MB1 (innermost)−MB4 (outermost); each of which is in turn divided into 12 azimuthal sectors, as illustrated in Fig. 3.13. There are 12 chambers in each three inner layers per wheel; in the outermost layer, the top and bottom sector each have two chambers leading to a total of 14 chambers. The whole barrel muon detector thus has 250 DT chambers. The chambers in MB1-MB3 consist of 3 superlayers (SL), while MB4 have two SLs. Two outer SLs with wires parallel to the beam axis measure the bending in the $r - \phi$ plane, and the inner SL with wires

[12]When muons cross the detector, bremsstrahlung is suppressed by a factor of $(m_e/m_\mu)^2 \sim (1/200)^2$. They lose an average of energy of ~ 3 GeV in the tracker and calorimeters mainly via ionization.

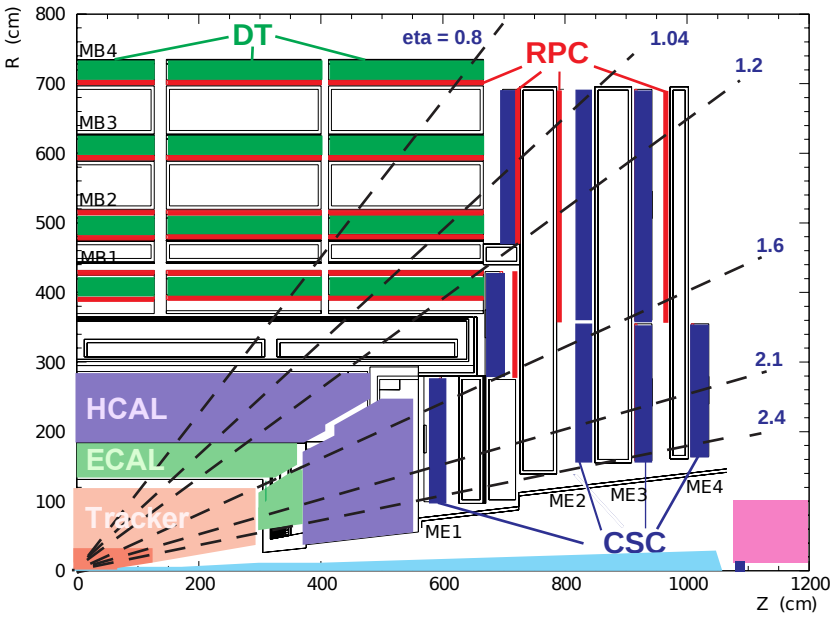

Figure 3.12: Longitudinal view of the muon system in the $r-z$ plane. DT is in the barrel region, and CSC in the endcap complemented with RPC, taken from [47].

perpendicular to the beam axis is for the z position measurement[13]. A SL is built out of 4 layers of rectangular DT cells staggered by half a cell.

The DT cell, filled with a gas mixture of Ar/CO_2, has a length of 2.4 m ($2-4$ m) for superclusters measuring the $r-\phi$ (z) coordinate and a cross section of 42×13 mm^2. An anode wire is in the cell center and the boundaries of the cell act as the cathode. Field shaping electrodes at the top and bottom of a cell improve the linear relationship between the drift time and path, which are essential for triggering capabilities. Such design ensures a negligible occupancy and a maximum drift time of 380 ns of the induced charges. The single hit position resolution is about 250 μm and the angular resolution in ϕ is about 1 mrad [65].

The endcap is exposed to a highly non-uniform magnetic field and an intense hit

[13]Chambers in MB4 have two SLs and thus only measure the $r-\phi$ coordinate.

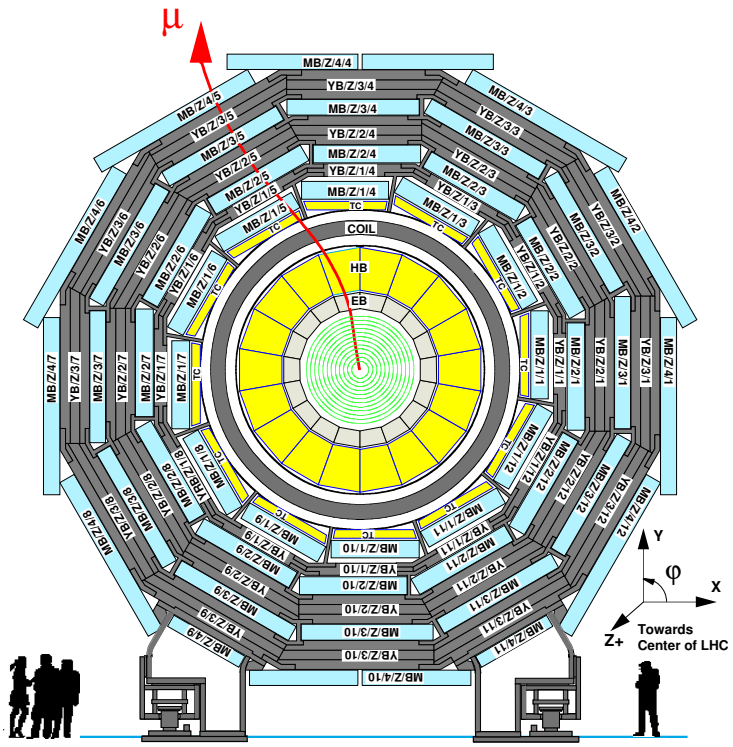

Figure 3.13: Layout of the CMS barrel muon DT chambers in one of the 5 wheels, taken from [44].

occupancy (up to 1000 Hz/cm^2). CSC is thus chosen in this region due to its fast response, fine segmentation, radiation hardness and ability to operate in a non-uniform magnetic field. Each of muon endcaps contains 4 stations of chambers (ME1−ME4), which are mounted on the disks enclosing the CMS magnet. The innermost station (ME1) consists of three concentric rings around the beam axis while the others have two. Each ring contains 36 trapezoidal shaped CSCs, except the innermost rings of ME2−ME4 each with 18 chambers. Apart from the outermost ring of ME1, CSCs in each ring are arranged with a small overlap in ϕ to avoid dead regions. The CSC is a multiwire proportional chamber. It is composed of 6 gaps, formed by 6 anode wires interleaved with 7 cathode panels and filled with a gas mixture of $Ar/CO_2/CF_4$. The wires are azimuthally oriented and thus used to measure the radial coordinate r. A cathode plane is segmented into strips perpendicular to

the wires, the interpolation of induced charges between the adjacent strips provides the information of ϕ position. The spatial resolution in $r-\phi$ plane varies from ~ 50 μm in ME1 to ~ 250 μm in ME4, and the angular resolution in ϕ is of order 10 mrad [66].

RPCs are featured by a fast response of a few nanoseconds, and are thus used as a muon trigger system for accurate bunch-crossing identification. They are coupled with both DTs and CSCs, with the layout matching the barrel and endcap segmentations. In the barrel, each of DT layers in two inner stations are embedded between two layers of RPCs which allows to trigger and reconstruct the low p_T muons, while a single RPC layer is placed on the inner side of DT layers of each two outer station. In the endcap, one RPC layer is integrated in each of the first three stations. RPCs consists of two 2 mm thick gaps made out of four parallel bakelite electrodes, with insulated readout strips placed in the middle. The double-gap configuration increases the charge induced on the strips. They work in the avalanche mode in order to sustain higher rates (up to 1000 Hz/cm^2). RPCs have a moderate space resolution of ~ 1 cm, and excellent time resolution of ~ 2 ns [67].

3.3 Trigger and Data Acquisition System

At LHC nominal luminosity (10^{34} cm^{-2}s^{-1}), an average of ~ 20 pp collisions occurs at the designed bunch crossing time of 25 ns. It leads to an event rate close to 10^9 Hz beyond the maximum processing rate of ~ 100 Hz. At nominal energy ($\sqrt{s} = 14$ TeV), out of total inelastic interactions with a cross section of ~ 60 mb, the most interesting events are rare with cross sections much smaller than 1 nb, as illustrated in Fig. 3.14[68]. Therefore, a trigger system has been developed to achieve a rejection factor of the order of 10^6, and at

the same time to keep a high efficiency on selecting interesting events[14]. It consists of two independent steps: Level-1 trigger (L1) and High-Level trigger (HLT).

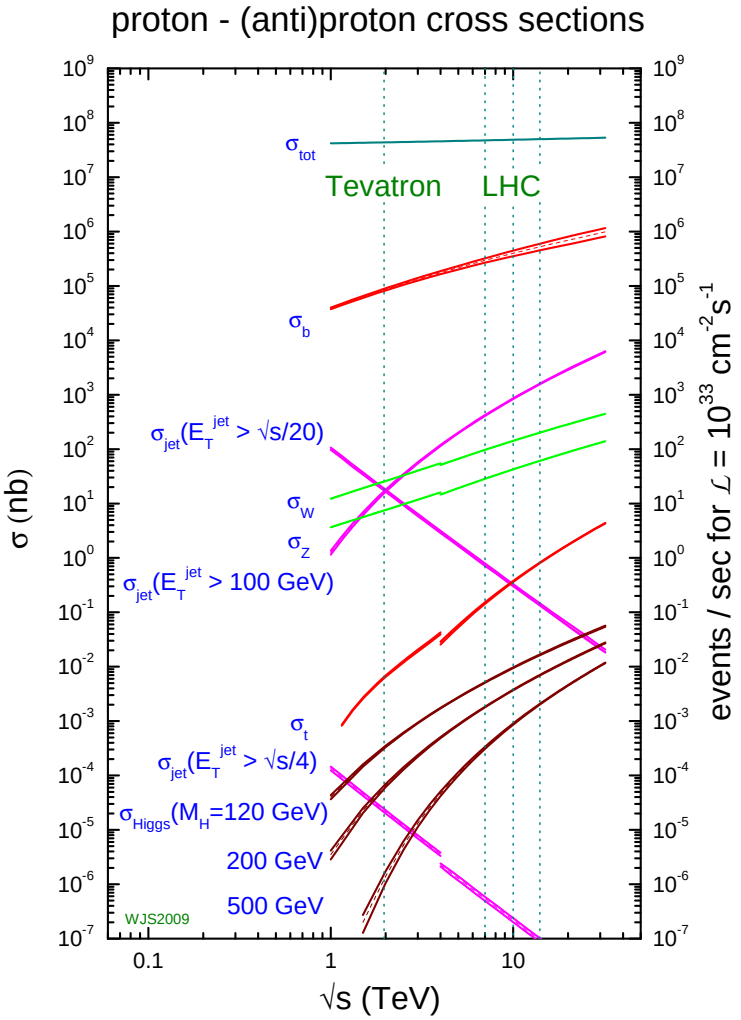

Figure 3.14: The figure shows cross sections of physics processes studied at the LHC, which span many orders of magnitude. It is taken from [68].

The CMS trigger and data acquisition (DAQ) system is illustrated in Fig. 3.15. The event data is stored in a front-end pipeline memory until the hardware-based L1 trigger produces an accept/reject decision within a trigger latency of 3.2 μs[15]. The limit of the

[14] At current luminosity ($\sim 10^{33}$ cm^{-2}s^{-1}), about one top pair event is produced per second, leading to about one semileptonic $t\bar{t}$ decay in every three seconds.

[15] The pipeline can store 128 bunch crossings corresponding to a latency of 128 $\times$ 25 ns= 3.2 μs. But, due to the transmission time, the time available for the L1 calculations is less than 1 μs.

output rate for the L1 trigger is designed to be 100 kHz, while in practice, it is about 30 kHz. The selected events are then processed by the software-implemented HLT, and the event data is further reduced to a 300 Hz output rate during 2011 data taking period.

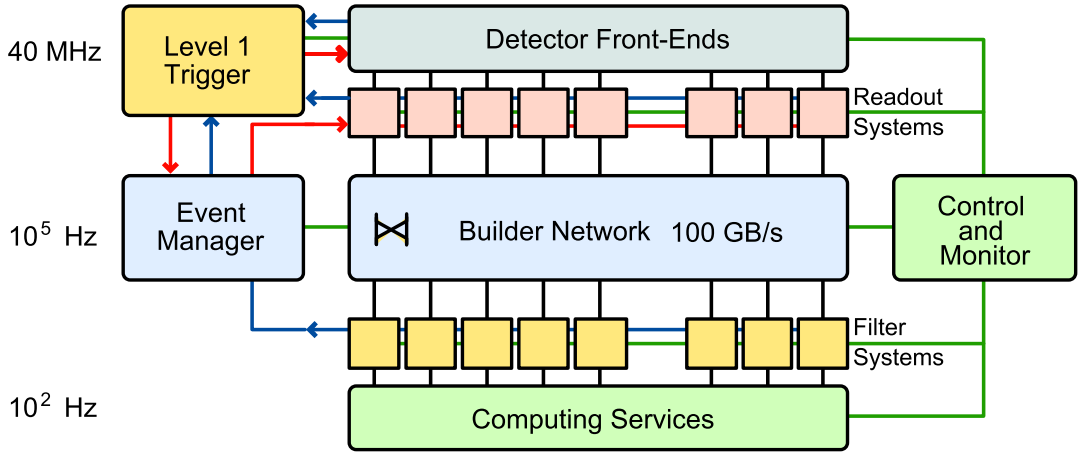

Figure 3.15: Data flow in CMS Trigger and DAQ system, taken from [69].

3.3.1 L1 Trigger

L1 trigger is based on coarsely segmented data from CMS calorimeters and muon system, consisting of three main subsystems: L1 calorimeter trigger, L1 muon trigger and L1 global trigger. L1 calorimeter/muon trigger subsystem has local, regional and global components. A schematic of the decision making process is shown in Fig. 3.3.1.

In L1 calorimeter trigger, the local triggers (trigger primitives) sum up the transverse energies deposited in each of trigger towers in the calorimeters[16], and also assign the correct bunch crossing to the trigger towers. The Regional Calorimeter Trigger (RCT) uses this information to find trigger objects, including isolated and non-isolated e/γ, tau, central and

[16] A trigger tower has a size of $\Delta\eta \times \Delta\phi = 0.087 \times 0.087$ in the region of $|\eta| < 1.8$, but a larger $\Delta\eta = 0.1 - 0.35$ beyond that region. The segmentation of trigger towers is the same for both ECAL and HCAL. In ECAL, it is a 5×5 crystals that matches a single HCAL tower.

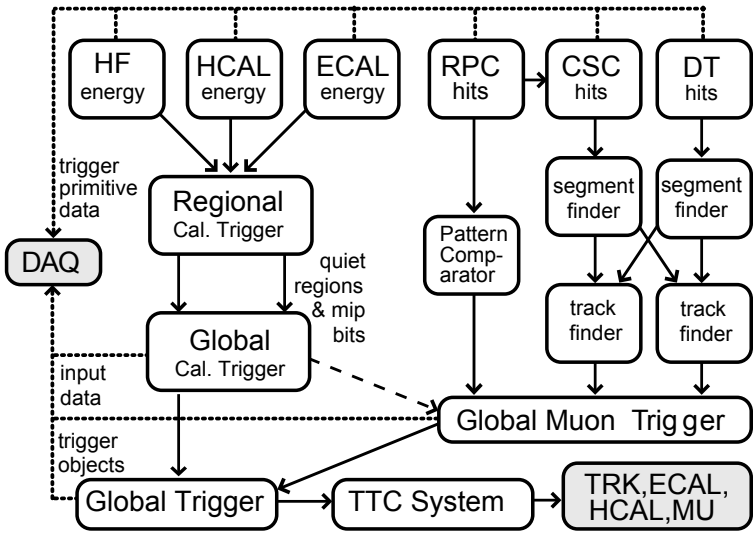

Figure 3.16: Overview of L1 trigger, taken from [69].

forward jet. The details of different algorithms for object determination are in [69]. It then gives each object candidate a rank based on its E_T and sends Global Calorimeter Trigger (GCT) the top four candidates for each trigger object. GCT sorts the trigger objects according to their rank, counts the jets and calculates the total E_T, $\not\!\!E_{\mathrm{T}}$ and scalar transverse energy sum of all jets above a given threshold (H_T). These outputs are then forwarded to L1 global trigger.

L1 muon trigger uses all three detectors of the muon system. The local triggers of both DT and CSC use the hit information to find track segments and assign the bunch crossing. DT provides track segments in ϕ projection and hit patterns in η projection, while CSC gives 3-dimensional track segments [44]. DT/CSC Track Finders, belonging to Regional Muon Trigger, match the segments to identify muon tracks, and determine their p_T, location (η, ϕ) and quality. The muon candidates are ranked by their p_T and quality. Four best muon candidates from each subsystem are sent to Global Muon Trigger (GMT). There is no local processing for RPC[17]; instead, a Pattern Comparator Trigger (PAC) finds the

[17]The measurements in each RPC chamber are simple points, so there is no local trigger [70].

coincidence in space and time between hits in several layers [70]. The number of coincident hits is used for muon tracks identification and p_T assignment. Four highest p_T muon candidates in both barrel and endcap are sent to GMT (a total of 8 candidates). GMT combines candidates from each sub-detectors, and assigns a quality code based on the number of sub-detectors that produce the same candidates, as well as on the quality of tracks. Additionally, it also correlates muon candidates with bits from calorimeters to check their isolation. The four highest quality muon candidates are sent to L1 global trigger.

L1 global trigger synchronises the input objects from the calorimeter and muon trigger system [71]. It generates L1 Accept signal (trigger decision) by applying programmable trigger requirements on the received objects, where a total of 128 algorithms can work in parallel. L1 Accept signal is then transmitted to all sub-detectors.

3.3.2 HLT

HLT operates on the events accepted by L1 trigger, and processes on a Event Filter Farm consisting of $\mathcal{O}(1000)$ CPUs. It has access to the full granularity of all sub-detectors, including the tracker that is unavailable in L1 trigger. As events only passing HLT are recorded permanently, HLT needs to meet some major requirements: it should be able to select events as inclusively as possible in order to keep potential events related to new physics; ensure a high efficiency of the physics objects from L1 trigger, use algorithms close to the offline reconstruction and include improvements from the offline reconstruction[18] [72].

HLT consists of a sequence of reconstructions and selections. The reconstruction is only implemented in the interesting regions of L1 trigger (regional) and will stop if there is

[18]For example, HLT began to include particle flow jets in 2011, before that HLT jet reconstruction only uses information from calorimeters.

enough information to remove an event (conditional). The selections are applied on the reconstructed physics objects such as muons, electrons/photons, jets, τ and b jets, detailed in [73]. The HLT menu consists of a set of trigger paths, and each path addresses a specific physics object selection.

The measurements described in this thesis are mainly based on the electron triggers. HLT electron selection contains three steps. First, the electron candidate is found by using only ECAL clusters and required to pass the same E_T thresholds as in L1 trigger. Next, hits in the Pixel detector are used to match with the electron candidate in the first step (if there are no matching hits in the clusters, the candidate is considered as a photon). Finally, the selection uses fullly reconstructed tracks, seeded from the pixel hits in the second step [74]. Details of the trigger paths are described in Section 5.3.1.

CHAPTER 4

Physics Objects Reconstruction

The physics objects involved in this analysis are reconstructed by the particle flow (PF) algorithm. This technique aims to reconstruct all stable particles in an event by combining information from all CMS sub-detectors, and thus provides a global event description. The PF reconstruction is detailed in Appendix A. In this chapter, the physics objects used in this thesis are presented, including the interaction vertices, leptons, jets, missing transverse energy and b quark jet identification.

4.1 Vertices

A pair of top quarks is created by a hard parton-parton scattering, and associated with a primary ("collision") vertex. The primary vertex is necessary for distinguishing prompt production of particles, and determining the event kinematics. The secondary ("decay") vertex is important for the identification of b jets from the top decay, as the decay length of b-hadron is boosted to the order of millimeters leading to a displaced vertex in the detector.

The primary and secondary vertex reconstruction uses tracks as input and involves two major steps: vertex finding and vertex fitting. First, tracks are filtered based on the number of hits in the tracker, the impact parameter with respect to the beam spot, and the normalized χ^2 of the track fit. The selected tracks are clustered according to their z impact parameters, within a group the tracks are separated in z no less than a distance $z_{\text{sep}} = 1$ cm from their nearest neighbor [75]. The resulting individuate clusters produce

vertex candidates. In the second step, tracks in the cluster are fit with an Adaptive Vertex Fit (AVF) [76]. AVF weights tracks according to their compatibility with the common vertex and gives the best estimate of the three-dimensional position of each vertex candidate. The resulting vertex candidates are sorted by the sum of the square of tracks' transverse momenta in the track cluster ($\sum P_T^2$), the first one is taken as the primary vertex. The primary vertex efficiency can achieve $\sim 100\%$ if at least two tracks have transverse momenta greater than 0.5 GeV in the vertex, and the resolution mainly depends on the number of tracks used in fitting the vertex and the p_T of those tracks, details are in [75]. The secondary vertex finding in b jets will be described in Section 4.6.

4.2 Electrons

This analysis explores the e+jets channel of $t\bar{t}$ events, so the reconstruction and identification of a hard electron is crucial in the signal selection. The electron reconstruction in CMS combines information from the pixel detector, the silicon strip tracker and the ECAL. When an electron traverses the silicon layers of the tracker, it interacts with the materials in front of the ECAL which sum up to $0.35 - 1.4$ radiation length depending on η. The electron radiates bremsstrahlung photons along its trajectory, illustrated in Fig. 4.1. Almost half of electrons radiate more than $\sim 50\%$ of their initial energy in this way. Due to the magnetic field, the electron energy reaches the ECAL with a significant spread in the azimuthal direction (ϕ direction). A further complication arises from the conversion of radiated photons in the tracking material.

The reconstruction strategy starts by the detection of energy clusters in the ECAL. To collect the radiated energy, multiple clusters are combined to form superclusters. Superclusters spread narrowly in η and more widely in ϕ due to bremsstrahlung. The

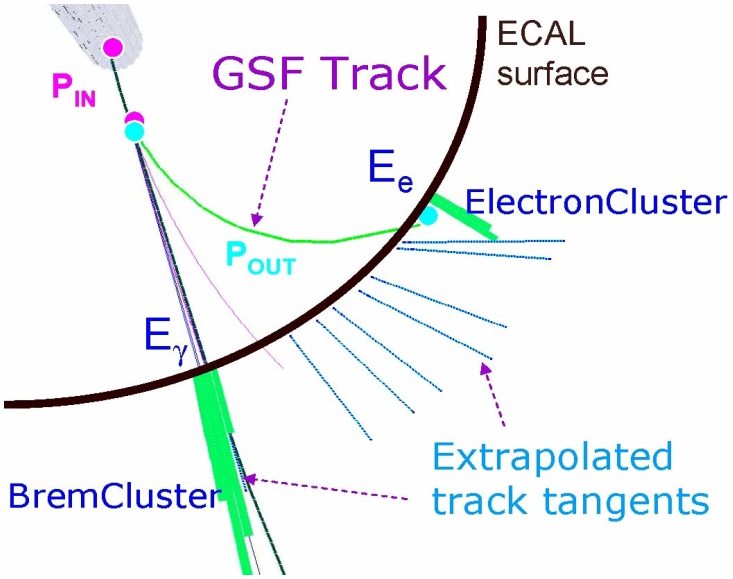

Figure 4.1: This cartoon illustrates an electron that loses energy by bremsstrahlung while traveling in the magnetic field, and leaves a signature in the ECAL [77].

different geometries of the EB and EE require the use of two distinct superclustering algorithms. Both algorithm starts with the seed crystals of relatively high energy, and perform the same task of grouping crystals associated with electromagnetic showers and collecting showers which are close in the η direction but in some larger window in ϕ.

To built electron tracks outward, superclusters with $E_T > 4$ GeV are selected, and then matched to track seeds that have two or three hits in the inner layers of the tracker. Two complementary algorithms are used at the track seeding stage. The cluster-driven seed finding strategy is optimised for isolated electrons in the p_T range relevant for Z or W decays down to ~ 5 GeV. The tracker-driven seeding is more suitable for low p_T electrons as well as performing better for electrons inside jets. Electron tracks are built from these tracker seeds by an iterative tracking approach described in A.1.1. Next, a pre-identification algorithm, based on track-cluster matching and on the track quality, is used to quickly identify the electron tracks. The pre-identification efficiency for single electrons is always greater than 95% with a pion mis-identification below 10% [78]. Their full trajectories are

established by performing a fit to these pre-identified tracks using Gaussian Sum Filter (GSF), which can model the highly non Gaussian bremsstrahlung energy loss.

An electron candidate is formed by linking the GSF track to the supercluster that matches its extrapolation to the ECAL. Electron candidates are also subject to a pre-selection to reduce rate of jets faking electrons. The pre-selection requires a minimum $\not{E}_{\mathrm{T}} > 4$ GeV, an η, ϕ geometrical matching and a cut on hadronic energy behind cluster. The electron momentum is a weighted mean of the supercluster energy and the track momentum, the weights are based on the uncertainties of each measurement.

The electron identification is performed by a simple cut-based method, which relys on shower shape variables and the ratio of energy deposited in the HCAL to the ECAL (H/E). For the offline electron selection, the electron identification contains cuts on $\sigma_{i\eta i\eta}$, $\Delta\eta$, $\Delta\phi$ and H/E. $\sigma_{i\eta i\eta}$ is the covariance of the supercluster shape in pseudorapidity, which is a measure of the supercluster width. $\Delta\eta$ and $\Delta\phi$ are used for spatial matching between supercluster and track direction at the vertex extrapolated to the ECAL. Moreover, a pair of conversion electrons is produced when photons interact with the dense material in front of ECAL. Since the conversion electrons have opposite charges, in the magnetic field, they will bend in opposite directions as seen in the ϕ plane. To reject such electrons, the track is required to have at least one hit in the innermost pixel layer. Conversion electron tracks are parallel to each other from the decay point and throughout the $r - z$ plane, the rejection can be further improved by cutting on two variables *Dist* and $\Delta \cot\theta$. *Dist* is defined as the 2D distance in the $x - y$ plane between the two tracks. For an ideal reconstructed conversion the tracks would be touching, so this quantity would be zero. θ represents the polar angles of the respective tracks [79]. Detailed cuts on electron identification and conversion rejection will be presented in Section 5.3.

4.3 Muons

To suppress the irreducible $t\bar{t}$ backgrounds from other decay channels ($e\mu$, $\mu\mu$, and μ+jets), we should be able to distinguish events containing muons. Muons mainly interact with the silicon detector through ionization and leave only a negligible amount of energy in the calorimeters, except when they are produced with an initial energy higher than about 100 GeV. They are reconstructed in the muon system and the silicon tracker separately, and then combined using two possible algorithms. In both the muon system and the tracker, the reconstruction of a muon track uses the similar seeding approach. It searches for a pattern of segments in the DT/CSC or two/three consecutive hits in the tracker. The pattern recognition is then performed by an iterative technique based on the Kalman-filter.

The *Global muon* reconstruction is based on an outside-in algorithm. The *stand alone muon* tracks are first reconstructed only in the muon detector [80]. Its trajectory is extrapolated back to the tracker, and then paired to a set of inner matching tracks. Then, a Kalman Filter is used again to fit hits belonging to each pair of stand alone muon track and the inner matching track. Based on the χ^2 of the fit, the best candidate is chosen, therefore, at most one global muon is reconstructed for a stand alone muon. About 1% of muon from collisions fail to find their matching track in the tracker. For muon $p_T > 200$ GeV the global fit improves the momentum resolution compared to the track only measurement.

The *Tracker muon*s are reconstructed using an inside-out algorithm. A track with $p_T > 0.5$ GeV and $p > 2.5$ GeV in the silicon tracker is extrapolated to the muon system [80]. The energy loss and uncertainty due to the multiple scattering are considered in the extrapolation. If the extrapolated track can be matched to at least one muon segment found from DT or CSC hits, a tracker muon is reconstructed. Compared with the

global muon, this algorithm is more efficient for reconstructing low p_T tracks as it requires only one single matched muon segment in the muon system.

The muon reconstruction described above is performed outside of the PF algorithm; and also provides additional information for muon quality selection and identification, such as track quality information: the number of track hits, the χ^2 of track fits, and the transverse impact paratmeter with respect to the primary vertex [80]. The results of these three algorithms in the muon reconstruction are merged into a single collection of muon candidates, which is then used as the main input for the identification of PF muons. PF algorithm optimized the selections provided by the muon reconstruction, together with the use of the energy measured in the calorimeter, to achieve a high efficiency (99%) and a few percent fake rate in identification [81].

4.4 Jets

Quarks and gluons cannot exist in a free form due to the color confinement as described in Section 2.1.2. Instead, they fragment and hadronize to form colorless hadrons that are roughly collinear to the initial parton due to the momentum conservation. When traveling through the detector, the resulting bunches of hadrons will deposit a broad of energy in the calorimeters and form the jets. The products of the $t\bar{t}$ final state always contain jets, moreover, the differential cross section is measured with respect to the jet multiplicity. Therefore, a reliable jet reconstruction and calibration is required. In the PF algorithm, jets are reconstructed by clustering all reconstructed PF particles with the anti-k_T algorithm. Therefore, the PF jets are much closer to jets in MC simulations than jets reconstructed solely in the calorimeters, and 90% of the jet energy can be reconstructed with a high precision both in value and direction [82].

4.4.1 Jet Clustering Algorithms

A jet algorithm defines jets as measurable physical objects describing parton level activity of an event, therefore, it should be efficient in clustering particles produced by the hadronization of a parton, such that the parton's momentum can be inferred by adding up the momenta of the clustered particles. Ideally, a jet algorithm is required to be insensitive to the emission of soft particles (infrared safety) and to collinear splitting of particles (collinear safety) in the event, termed "IRC safety". The IRC-safe property of the jet algorithm enables comparisons of the jets to theoretical calculations in any pertubative order.

The anti-k_T algorithm is a combination of k_T and Cambridge/Aachen algorithms [83], and is the default jet algorithm for most physics analysis at CMS. It takes the locally highest-momentum particle and iteratively cluster its nearby particles that are closest according to some distances measured in both position and momentum space, and thus reflects the process of parton showering. Two sets of distances are defined corresponding to the distance between any two particles (d_{ij}) and the distance between any particle and the beam (d_{iB}), respectively:

$$d_{ij} = \min\left(\frac{1}{k_{T_i}^2}, \frac{1}{k_{T_j}^2}\right)\frac{\Delta_{ij}^2}{R^2}, \tag{4.1}$$

$$d_{iB} = \frac{1}{k_{T_i}^2}, \tag{4.2}$$

where k_{T_i} is the transverse momentum, $\Delta_{ij}^2 = (y_i - y_j)^2 + (\phi_i - \phi_j)^2$ is the angular distance of particle i and j in $y \times \phi$ plane, the size parameter R is set to 0.5 in the presented study.

For a given list of particles, the anti-k_T algorithm looks for the smallest distance among all d_{iB} and d_{ij}. if the smallest is d_{iB}, then particle i is removed from the list and considered as a jet. If the smallest is a d_{ij}, particle i and j are recombined to form one

single new particle by adding their four-momenta, and all distances are recomputed. The procedure is repeated until no particles are left. The output does not change if any minor reconfiguration in the input list occurs such as adding a soft radiation. In PF algorithm, all particles without distinction of type and without any energy threshold, are clustered into PF jets using the anti-k_T algorithm.

4.4.2 Jet Energy Correction

The measurement of jet energies can be distorted by various effects. The largest one is from the non-linear response of hadronic calorimeter in p_T and η of the jets. In order to correctly map the kinematical properties of the reconstructed jets to the original partons, CMS adopts a factorized scheme for jet energy corrections. Different corrections are considered to be independent, such that the total correction is a series of multiplicative correction factors [84].

In the first step, `L1FastJet` correction accounts for the additional measured energy that does not belong to the hard processes, such as the energy from pile-up events or noises in the electronics. `L2Relative`, a relative correction, is to achieve a flat calibrated energy response in η using di-jets events. The partner jets are adjusted to have the same response as jets in the central region, as the the di-jets events are expected to be back-to-back in their center-of-mass frame. `L3Absolute` correction sets the absolute jet energy scale as a function of p_T. Using the γ+jet events, the recoiling jet p_T is balanced by a photon, since the photon measured in the ECAL has a much better energy resolution than the HCAL. Finally, `L2L3Residual` correction, applied to the data only, corrects the difference between the simulation and data, as the default jet energy corrections derived from MC systematically over-correct the jets in the data. The total jet energy correction depends on

p_T and η of jets which can reach $10\% - 20\%$ for $p_T = 20$ GeV in all detector regions [84]. The jet energy resolution is $\sim 10\%$ over the whole range of jet transverse momentum [85].

4.5 Missing Transverse Energy ($\not\!\!E_{\mathrm{T}}$)

When neutral weakly-interacting particles, such as neutrinos in the $t\bar{t}$ final state of e+jets channel, pass through the detectors, they do not produce any response in the detector elements. The momentum imbalance of all reconstructed objects in an event indicates the presence of such particles, since the net transverse energy of an event is zero for a head-on collision. At the hadron colliders, the boost of the initial partons parallel to the beam axis is not known, therefore the reconstruction of the missing energy measurement along this axis is not possible. Instead, the missing transverse energy $\not\!\!E_{\mathrm{T}}$ is used, which is the momentum imbalance in the plane perpendicular to the beam axis.

In the PF algorithm, $\not\!\!E_{\mathrm{T}}$ is calculated as the negative vector sum of all the transverse energy deposits in the detector: $|-\sum_i \vec{E}_T^i|$ where the sum runs over all particles reconstructed in an event. Jets used for $\not\!\!E_{\mathrm{T}}$ calculation with $p_T > 10$ GeV are corrected using the jet energy corrections described in Section 4.4.2 [86]. Jets p_T below 10 GeV are not corrected because of the large uncertainty of these corrections for such jets. These corrections can be up to a factor of two for the Calo $\not\!\!E_{\mathrm{T}}$, but less than 1.4 for the PF $\not\!\!E_{\mathrm{T}}$ [86]. Since the PF algorithm includes tracker information for charged hadrons, this global algorithm produces the best resolution such that the resolution of the PF $\not\!\!E_{\mathrm{T}}$ is improved by a factor of two with respect to the calorimeter based $\not\!\!E_{\mathrm{T}}$.

4.6 b Quark Jets Identification

The identification of b quark jets is a powerful tool for the background suppression because most of the non-$t\bar{t}$ processes do not contain heavy flavor quarks in the final states. Whereas, $t\bar{t}$ events produce two b quark jets from top decays. Several b-tagging algorithms in CMS explores distinguishing properties of B hadrons, such as their long lifetime ($\sim$ 1.5 ps), large mass ($\sim$ 5 GeV), and large decay fraction into leptons ($\sim$ 20%). For the analysis in this thesis, we apply a secondary vertex based algorithm. It takes advantage of the long lifetime of B hadrons together with the large relativistic boost. The resulting displaced distance is several millimeters on average, i.e., a 20 GeV B hadron decays after traveling 2 mm, as illustrated in Fig. 4.2. This algorithm thus searches for track vertices displaced with respect to the primary vertex.

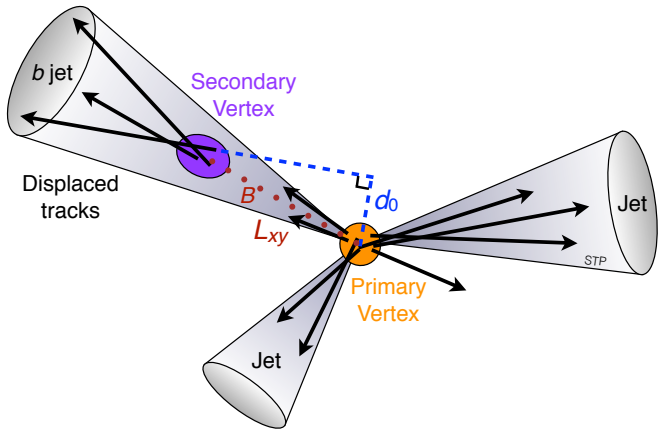

Figure 4.2: An illustration of a b-jet in the $r-\phi$ plane showing a secondary vertex w.r.t the primary, taken from [87].

A simple version, called "simple secondary vertex" (SSV) algorithm is based upon the reconstruction of at least one secondary vertex inside a jet. Vertex candidates, reconstructed from fitting tracks[1] via AVF as described in Section 4.6, are selected as secondary vertex

[1] ΔR between an input track the jet direction is required to be less than 0.3 in order to remove tracks from pileup.

candidates if they share less than 65% of their tracks with the primary vertex and the significance of flight distance in transverse plane exceeds 3σ. Moreover, the secondary vertex candidates are required to have a distance from the primary vertex in the transverse plane less than 2.5 cm, its invariant mass of charged particles associated to the vertex smaller than 6.5 GeV. Finally, the flight direction of each candidate also has to be within a cone of $\Delta R < 0.5$ around the jet direction [88]. The significance of the 3D-flight distance is used as a discriminating variable for this tagger.

A more complex approach, called "combined secondary vertex" (CSV) algorithm, is applied in the differential cross section measurement. This algorithm involves the use of secondary vertices together with other topological and kinematical variables, such as the impact parameter significance and 2D-flight distance significance, etc., detailed in [88]. This algorithm provides discrimination even when no secondary vertices are found. In such cases, a so called "pseudo vertex" category is created from charged particle tracks that have a signed transverse impact parameter significance greater than 2. Even when this is not fulfilled, a "no vertex" category resorts simply to track-based variables. The maximum possible b-tagging efficiency of CSV is thus not limited by the secondary vertex reconstruction efficiency.

In CSV algorithm, these variables are used as inputs to a Likelihood ratio to construct the discriminator. As c jets behave quite differently from the light jets (u, d, s jets and gluons), the Likelihood ratio contains two parts for the discrimination against the c jets and light jets [89] as following,

$$\mathcal{L}^{b,c,q} = f^{b,c,q}(\alpha) \times \Pi_i f_\alpha^{b,c,q}(x_i), \tag{4.3}$$

where α is the vertex category, x_i is the individual variable, q stands for light jets, $f^{b,c,q}(\alpha)$ is the probability to fall into category α of each jet flavor and $f_\alpha^{b,c,q}(x_i)$ is the corresponding

probability density function for variable x_i. The discriminator y is then defined as:

$$y = f_{BG}(c)\frac{\mathcal{L}^b}{\mathcal{L}^b + \mathcal{L}^c} + f_{BG}(q)\frac{\mathcal{L}^b}{\mathcal{L}^b + \mathcal{L}^q}, \tag{4.4}$$

where $f_{BG}(c)$ ($f_{BG}(q)$) is the expected prior for the c (q) content in non-b jets ($f_{BG}(c) + f_{BG}(q) = 1$). They are set to $f_{BG}(c) = 0.25$ and thus $f_{BG}(q) = 0.75$, such choice is from the flavor composition of hadronic W decays, but works well in general. For b quark jets, the discriminator y is close to one, as shown in Fig. 4.3. In the differential cross section measurement, y is chosen to be 0.679 which is the medium working point (explained later).

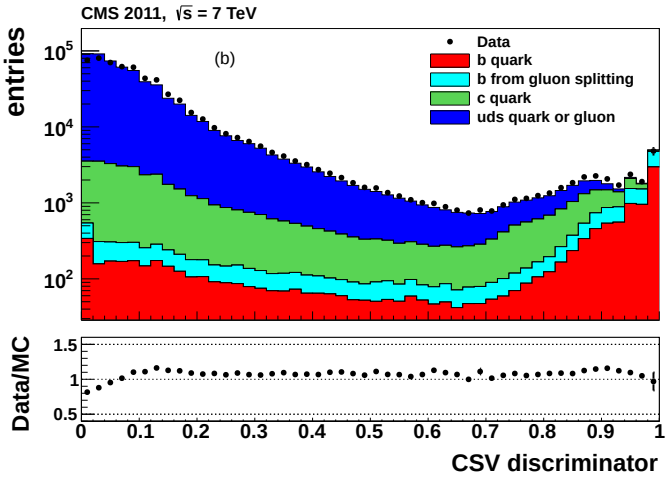

Figure 4.3: Distribution of the CSV discriminator, taken from [88]. The data sample corresponds to a trigger selection with jet $p_T > 60$ GeV and includes a "soft" muon with $p_T > 5$ GeV. MC are QCD multi-jets events.

A loose, medium and tight operating points are designed for all b jet identification algorithms in CMS. They are the minimum thresholds of tagger discriminators to achieve a mis-identification probability for light jets close to 10%, 1%, and 0.1% at an average jet p_T of about 80 GeV. From the performance study [88][90], CSV is the most effective algorithms with tagging efficiencies of 85.0%, 75% and 55% for loose, medium and tight operating points respectively, as shown in Fig. 4.4. The tagging efficiencies of the different algorithms

at these working point have been measured by different methods, i.e. "PtRel", system8, the reference lifetime method, detailed in [91][92][88]. The example of the efficiencies measured for the CSVM tagger is shown in Fig. 4.5. The measured b jet tagging efficiency is implemented by applying scale factor corrections to the MC simulation, details are in Section 5.3.

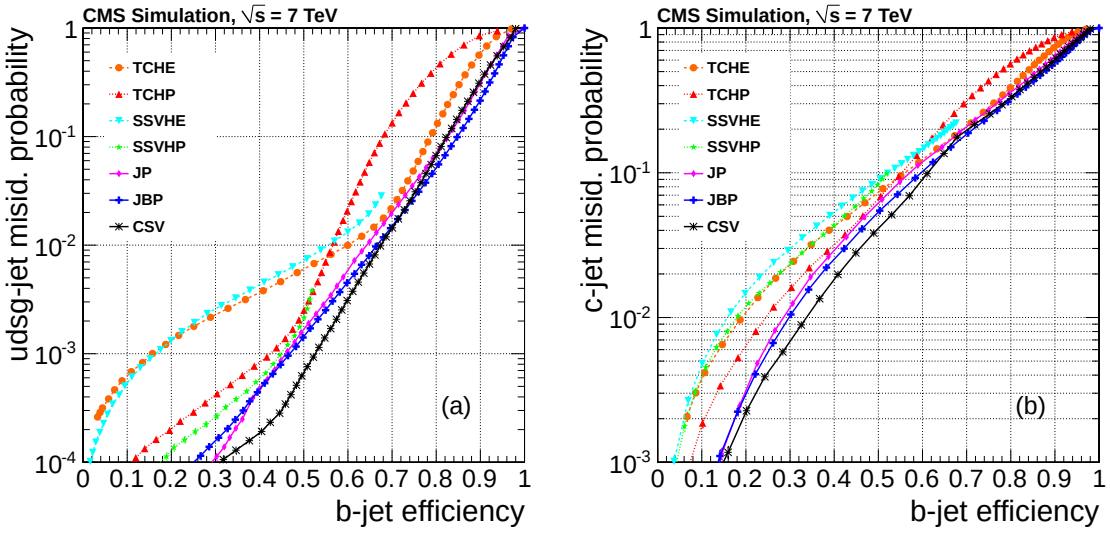

Figure 4.4: Performance curves: (left) light-parton and (right) c-jet misidentification probabilities as a function of the b-jet efficiency, taken from [88].

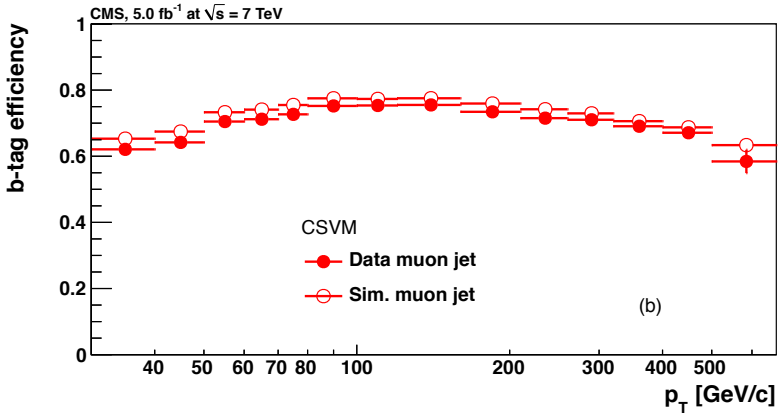

Figure 4.5: b-jets identification efficiency measured for the CSVM tagger using the reference lifetime method, taken from [88]. The data and MC samples are the same as in Fig. 4.3.

CHAPTER 5

Analysis Overview

In this chapter, the characteristics of the top signal final state is summarized in Section 5.1 together with a description of the main background processes. Section 5.2 lists the datasets used for the measurements of the $t\bar{t}$ inclusive and differential cross section. The MC simulation of both signal and background events are introduced as well. Based on the final state topology of signal, a reference event selection is developed and detailed in Section 5.3.1 and 5.3.2. The MC events reweighting and data/MC comparision are presented in Section 5.3.3 and 5.3.4.

5.1 Signal and Backgrounds

In this thesis, the production cross section of top pair is measured in the e+jets channel. Fig. 5.1 shows the tree-level Feynman diagram of this process. The signature of these events is comprised of an isolated electron with high transverse momentum (p_T), four high p_T jets containing two b jets originating from top decay and a large $\not{E}_{\mathrm{T}}$ due to the undetected neutrino.

Many physics processes have a similar signature as the $t\bar{t}$ signal. The dominant background contributions come from W+jets and QCD events.

1. The W+jets events consist of a real W boson in association with i) heavy (light) quarks from flavor excitation and creation or ii) gluons which then split into a pair of

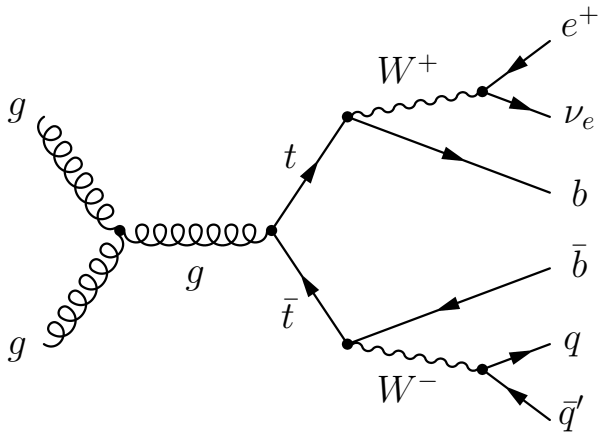

Figure 5.1: Tree-level Feynman diagram of a $t\bar{t}$ event in electron+jets channel. Both top quarks decay weakly into a W boson and a b quark. One of W bosons decays into an electron and a neutrino, the other one decays hadronicly into two quarks.

heavy (light) flavor quarks. W+heavy flavor events such as $Wb\bar{b}$, $Wc\bar{c}$ and Wc are an irreducible source of background, as illustrated in Fig. 5.2(a) and 5.2(b). W+light flavor events can reproduce the signal when a light jet is mis-tagged as a b jet, see in Fig. 5.2(c). This background contribution is estimated from a combination of data and simulation since the rate of $W+$ heavy flavor jets cannot be accurately calculated.

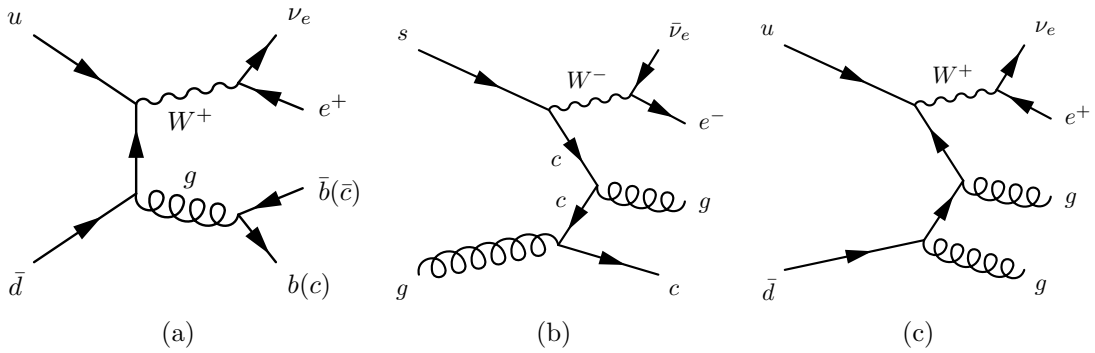

Figure 5.2: Feynman diagrams of $W+$jets events, 5.2(a) is $Wb\bar{b}$ ($Wc\bar{c}$) process with b (c) type quark from gluon splitting; 5.2(b) is Wc with c quark produced from quark gluon fusion and 5.2 is $W+$light flavor process.

2. QCD events can be selected as signal events when: i) the electron is faked by a

hadron; ii) electron is produced from a conversion or a semi-leptonic decay of a heavy flavor hadron. The large $\not\!\!E_{\mathrm{T}}$ can originate from a detector mis-measurement or from the neutrino of a semi-leptonic decay. Finally, the b-tagged jets can be due to an actual heavy flavor jet or a mis-tagged light flavor jet. This process has by far the largest production cross section, but its contribution can be suppressed to a manageable level by requiring a highly isolated electron. For the background estimation, we have to rely on the data as the heavy flavor content of QCD events is not well predicted and the mis-measurements are difficult to reproduce in the simulation. Fig. 5.3 shows two examples of QCD events with similar final states as the signal.

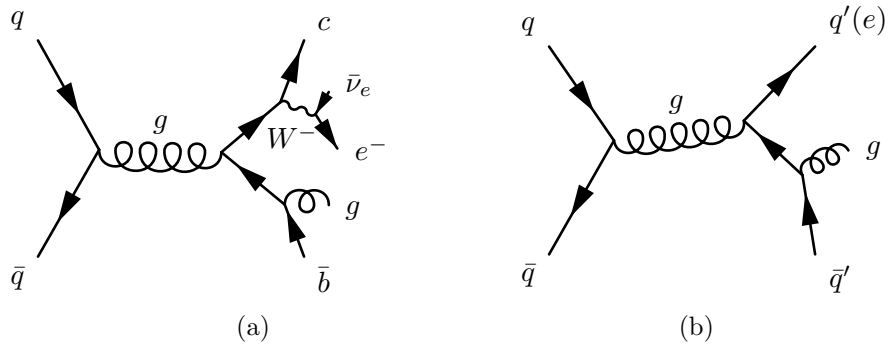

Figure 5.3: Example Feynman diagrams of QCD multijet events. In 5.3(a), b quark is produced via the strong interaction; in 5.3(b) the event contains only quarks and gluons in the final state but one of jets is misidentified as an electron.

3. Single top quarks are produced via the weak interaction, as opposed to the top pair production by the strong interaction. There are three single top quark production modes. Two of them have a b quark in the final state, called s and t channel; the other, called as tW channel, has a W boson produced by b quark and gluon fusion. Fig. 5.4 shows the Feynman diagrams of these three modes. Their contributions are estimated from simulation due to their negligible cross sections compared to the

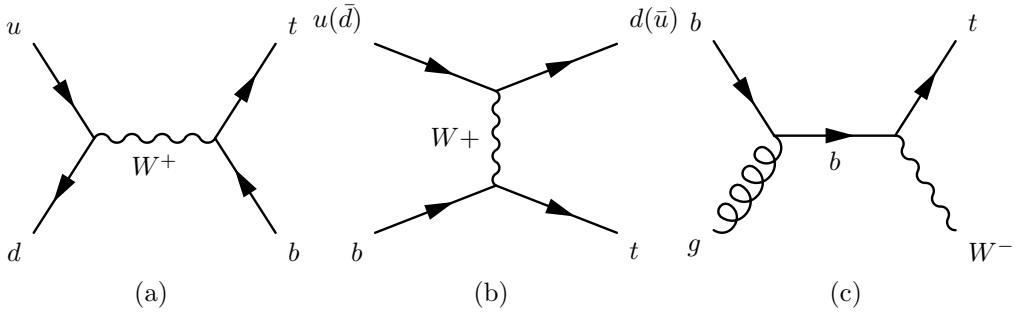

Figure 5.4: 5.4(a), 5.4(b) and 5.4(c) show the LO Feynman diagram of single top t, s and tW channel respectively.

W+jets and QCD. Moreover, the event selections described later can effectively discriminate $t\bar{t}$ signal from the single top backgrounds.

4. Electroweak (EWK) production modes contain Z+jets, WW, WZ and ZZ events. Z boson decays into two leptons in conjunction with several jets, also called Drell-Yan (DY) process. If one of leptons is misidentified (or missed), it will mimic the $t\bar{t}$ signature. WW and WZ have a charged lepton, a neutrino and heavy flavor quarks in the final state. ZZ production can be selected as signal when one lepton is not detected, resulting in increasing missing transverse energy. The contamination from such processes is limited by the low acceptance for Z+jets events passing the event selections and the low cross section of di-boson production, they are therefore estimated using MC.

In the $t\bar{t}$ cross section measurement, the main backgrounds are W+jets and QCD events. The simulations show that even after applying the event selection (explained in Section 5.3.1), W+jets and QCD events still dominate the data sample in $\sim 45\%$ and $\sim 20\%$ respectively while the signal ($t\bar{t}$) possesses $\sim 25\%$. Since these two backgrounds heavily affect the precision of the measurement and cannot be reliably modeled, they have to be estimated from data.

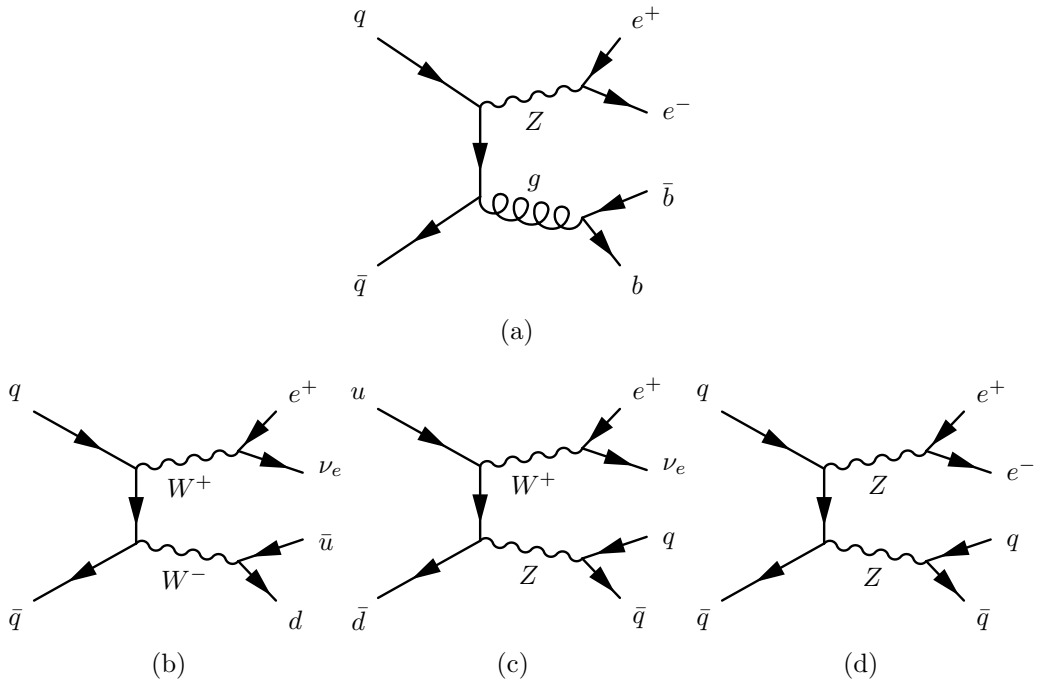

Figure 5.5: 5.5(a) is the Feynman diagram of Z+jets events. 5.5(c)−5.5(d) show the three modes of electroweak production.

5.2 Data Samples and Event Simulation

Two results, with different data samples, are reported in this thesis. The first result is a measurement of the total $t\bar{t}$ production cross section with data collected in the first half of the 2011 run. The corresponding luminosity is 857.7 pb^{-1}. In the second result, which is the differential cross section measurement, we increase the statistics to reach a total luminosity of 5.0 fb^{-1} with the full 2011 data. Data samples for these measurements are listed in Appendix B.1. We select data where none of the detector components showed errors according to the certified good-run lists (JSON files), see Appendix B.1.

1. The top pairs events are generated using MADGRAPH [93]. MadGraph is a tool for generating matrix elements[1] for high energy physics processes with up to three

[1]The matrix element represents the Feynman amplitude ($\mathcal{M}$) of a given process, detailed in [94].

additional partons. These $t\bar{t}$ events, with hard and well separated partons, are then fed into PYTHIA [95]. PYTHIA, unlike MadGraph for producing only hard processes, is able to perform parton showering and hadronization. The Kt-MLM matching prescription is used to avoid double counting of emissions in overlapping phase space [93]. The threshold of jet p_T for the matching procedure is set to 20 GeV. The renormalization and factorization scale (Q^2) is set to $Q^2 = (2m_t)^2 + (\sum p_T^{\text{jets}})^2$, where the top quark mass (m_t) is of 172.5 GeV. For systematic uncertainty studies, two MC samples are produced in the similar procedures as described above but with the varied Q^2 scales around the central choice by factors of 2 and 0.5. They are called Q^2 scale up and down respectively and listed in Appendix B.

2. The events of W/Z with extra jets are also produced by MADGRAPH with up to four additional partons. The parton level events are then passed to PYTHIA, using the same matching procedure but a different p_T threshold of 10 GeV. The W+jets events are generated inclusively with respect to jet flavors. Reconstructed jets are further matched to partons in the simulation [96]. Q^2 are also varied by factors of 2 and 0.5 around is central value $Q^2 = m_{W/Z}^2 + (\sum p_T^{\text{jets}})^2$ ($m_W = 80.4$ GeV, $m_Z = 91.2$ GeV) for systematic uncertainty studies.

3. QCD processes are simulated using PYTHIA. The generic QCD samples are huge and most of them cannot pass the event selection (described in Section 5.3). In order to increase the statistics of events passing the event selection, two different filters are applied on the generic QCD events to select samples including electrons. The EMenriched filter enriches samples with isolated electrons, and consists of two components. The first component operates on the energy clusters built from e, γ, $\pi^{\pm}$ and $K^{\pm}$ with $E_T > 1$ GeV within the tracker acceptance. The total E_T of the cluster is required to be greater than 20 GeV. The second component looks for single e, $\pi^{\pm}$

and $K^{\pm}$ with $E_T > 20$ GeV and $|\eta| < 2.5$. In both components, an isolation of both tracker and calorimeters is calculated and required to exceed a threshold. The BCtoE filter searches for events with electrons from the haronic decay of b or c quarks. Electrons are required to fall within the tracker acceptance with energy greater than 10 GeV. Each of EMenriched and BCtoE samples are divided into three p_T bins ($20-30$ GeV, $30-80$ GeV and $80-170$ GeV), leading to a total of six orthogonal QCD samples.

4. The single top and anti-top events are generated in the s, t and tW channel separately using POWHEG [97] and passed to PYTHIA for fragmentation and hadronization. The electroweak events are simulated using PYTHIA, these samples are only included in $t\bar{t}$ differential cross section measurement.

The generated events are interfaced to a detector simulation GEANT4 [98]. It models the interaction of particles with detector materials, such as bremstrahlung, multiple scattering, electromagnetic showering and haronic showering. The output events are reconstructed using the same algorithms as for data. The official MC samples used in this thesis are in Appendix B.2 and B.3. Tab. 5.1 lists the cross sections of each process, which are used to normalize the simulated events to the integrated luminosity of data for comparison with the measured distributions. It should be noted that the NNLO cross section of $t\bar{t}$, including soft-gluon corrections [99], is used in the differential cross section measurement.

5.3 Event Selection

In the e+jets channel, $t\bar{t}$ events contain a single high p_T, isolated electron accompanied by at least three energetic jets. The event selection follows a common event selection for the

Table 5.1: Summary of signal and background processes in the analysis, together with their cross sections. For QCD samples, the cross sections are expressed as the product of the total cross section in a given p_T^e range and the filter efficiency.

Process	Cross section [pb^{-1}]
$t\bar{t}$	157.5 (NLO) [100]/165.6 (NNLO) [99]
W+jets	31314.0 (NNLO) [101]
Z+jets	3048.0 (NNLO) [101]
single-t t	41.92 (NLO) [102]
single-t tW	7.87 (NLO) [103]
single-t s	3.19 (NLO) [104]
single-$\bar{t}$ t	22.65 (NLO) [102]
single-$\bar{t}$ tW	7.87 (NLO) [103]
single-$\bar{t}$ s	1.44 (NLO) [104]
WW	47.04 (NLO) [105]
WZ	18.57 (NLO) [105]
ZZ	7.67 (NLO) [105]
QCD 20to30_EMEnriched	236100000 $\times$ 0.0106 (LO)
QCD 30to80_EMEnriched	59440000 $\times$ 0.061 (LO)
QCD 80to170_EMEnriched	898200 $\times$ 0.159 (LO)
QCD 20to30_BCtoE	236100000 $\times$ 0.00059 (LO)
QCD 30to80_BCtoE	59440000 $\times$ 0.00242 (LO)
QCD 80to170_BCtoE	898200 $\times$ 0.0105 (LO)

Top Physics Analysis Group at CMS which is based on the observation of an electron and at least three jets [106]. The measurement of the inclusive $t\bar{t}$ cross section is limited by the low statistics (857.7 pb^{-1}), and the b-tagging technique is not applied in order to preserve the statistics in the control region for the background estimation. Since the differential cross section measurement uses more data (5 pb^{-1}), it is possible to employ b-tagging for removing backgrounds, especially QCD events.

5.3.1 Event Selection in Top Pair Cross Section Measurement

Trigger: Single electron triggers HLT_EleX_CaloIdVT_CaloIsoT_TrkIdT_TrkIsoT are applied first, where X is the trigger thresholds of electron p_T. VeryTight (VT) and Tight (T) working point are chosen for electron identification in calorimeters (Calo) and tracker (Trk) respectively using simple cuts on four variables[2]: $\sigma_{i\eta i\eta}$, H/E, $\Delta\eta$ and $\Delta\phi$, while the isolation (Iso) cut in both calorimeters and traker is chosen to be Tight (T), all of which are detailed in [107]. Tab. 5.2 shows the trigger list, electron p_T is raised up to 42 GeV in order to keep trigger rates at reasonable level.

Table 5.2: Single electron HLT trigger list.

names of data periods used for convenience	version	run range
HLT_Ele27_CaloIdVT_CaloIsoT_TrkIdT_TrkIsoT	v1	160404-161176
HLT_Ele27_CaloIdVT_CaloIsoT_TrkIdT_TrkIsoT	v2	161216-163261
HLT_Ele27_CaloIdVT_CaloIsoT_TrkIdT_TrkIsoT	v3	163286-163869
HLT_Ele32_CaloIdVT_CaloIsoT_TrkIdT_TrkIsoT	v3	165088-165633
HLT_Ele42_CaloIdVT_CaloIsoT_TrkIdT_TrkIsoT	v1	165970-166967

Pre-selection: We skim events by requiring at least one good quality primary vertex, which is not fake, has more than 4 degrees of freedom, an impact parameter with respect to the beam spot must be within $|\rho| < 2$ cm in the transverse plane and within $|z| < 24$ cm along the direction of the beam. We then require that events should have at least one PF electron candidate with $p_T > 15$ GeV and $|\eta| < 2.8$ and at least one PF jet with $p_T > 15$ GeV.

Electron Selection: After the pre-selection, we require exactly one isolated PF electron. The isolated electron candidates should pass several requirements:

[2]Definions of these variables are in Section 4.2

- $p_T > 45$ GeV
- $|\eta| < 2.5$. In addition, candidates in the ECAL barrel-endcap transition region are removed by rejecting events with $1.4442 < |\eta_{SC}| < 1.566$, where η_{SC} is the pseudorapidity of the ECAL supercluster.
- transverse impact parameter with respect to the beam spot $|d_B| < 0.02$ cm
- PF relative isolation < 0.1. PF relative isolation is defined as $I_{\text{rel}} = (I_{\text{charged}} + I_{\text{photon}} + I_{\text{neutral}})/p_T$, where the numerator is the scalar sum of the transverse energies of PF charged particles, PF photons and PF neutral particles in a cone of size $\Delta R = \sqrt{\Delta\phi^2 + \Delta\eta^2} < 0.3$ around the electron direction but excluding the electron, divided by electron p_T.
- pass the simple cut based electron ID [108]. The so-called working point 70 (wp70) is applied, which selects electrons at an efficiency of about 70% in Z boson events. The selections for wp70 are listed in Tab. 5.3.

Table 5.3: The simple cut based electronID at wp70 for electrons in the ECAL barrel and endcaps.

variable	ECAL Barrel	ECAL Endcaps
$\sigma_{i\eta i\eta}$	< 0.01	< 0.03
$\Delta\phi$	< 0.03	< 0.02
$\Delta\eta$	< 0.004	0.005
H/E	< 0.025	< 0.025

Muon Veto: To remove events from $e\mu$ channel in $t\bar{t}$ events, a loose muon veto is then applied where events containing one or more high p_T muons with the following properties are rejected:

- muon marked as a GlobalMuon,
- $p_T > 10$ GeV,
- $|\eta| < 2.5$,
- PF relative isolation < 0.2.

Z Boson Veto: A Z veto requirement reduces Z+jets background. Events containing di-electrons in the invariant mass window of the Z boson ($|m_{ee} - m_Z| < 15$ GeV) are rejected. These events have one good electron which passes the cuts defined in the electron selection and an additional loose electron. The loose electron fulfills the following requirements:

- $p_T > 20$ GeV,
- $|\eta| < 2.5$ excluding the EB-EE transition region ($1.4442 < |\eta_{sc}| < 1.5660$),
- PF relative isolation < 1.0.
- passes electronID at wp90 (corresponding to 90% selection efficiency), see Tab. 5.4.

Table 5.4: The simple cut based electronID at wp90 for electrons in the ECAL barrel and endcaps.

variable	ECAL Barrel	ECAL Endcaps
$\sigma_{i\eta i\eta}$	< 0.01	< 0.03
$\Delta\phi$	< 0.8	< 0.7
$\Delta\eta$	< 0.007	0.01
H/E	< 0.15	< 0.07

Photon Conversion Rejection: Events are rejected if the isolated electron originates from the conversion of a high p_T photon. First, the isolated electron candidate must have

no missing hits in the inner layers of the tracker, since photons travel through the tracker before producing a pair of electrons and thus leave no hits in layers of tracker between the beam line and the conversion vertex. Additionally, a rejection is also made using the partner track conversion veto with $|\Delta \cot\theta| < 0.02$ and $|\Delta Dist| < 0.02$ cm, where the definition of $\Delta \cot\theta$ and $Dist$ are in Section 4.2.

Jet Selection: PF Jets are required to have their $p_T > 30$ GeV and $|\eta| < 2.4$, in addition, they should pass the loose PF jet identification [109] as following:

- the number of constituents is larger than 1,
- the charged electromagnetic fraction (CEF) is smaller than 0.99,
- the neutral hadronic fraction (NHF) is smaller than 0.99,
- the neutral electromagnetic fraction (NEF) is smaller than 0.99,
- the charged hadronic fraction (CHF) is larger than 0,
- the number of charged hadrons is larger than 0. Finally, there are at least 3 PF Jets that pass the above criteria in the final state.

5.3.2 Event Selection in Top Pair Differential Cross Section Measurement

Trigger: During the 2011 data taking period, the instantaneous luminosity of LHC was continuously increased, giving rise to an increasing number of pileup events (explained in Section 5.3.3.1). Therefore the trigger rate needs to be increased to deal with this situation. For the single electron triggers, the trigger rate, with electron p_T thresholds relevant for top

quark physics studies, increased to a rate which could not be sustained. They are thus pre-scaled, which means that a fraction of events is not recorded, leading to a loss of signal. To use the full 2011 dataset, the HLT_Ele25_TriCentralJet30 is employed instead. It requires one online reconstructed electron with $p_T > 25$ GeV and three online reconstructed jets with $p_T > 30$ GeV and $|\eta| < 2.6$. Tab. 5.5 shows the trigger list applied on the full 2011 dataset for the differential cross section measurement.

Table 5.5: Electron-had HLT trigger list.

Sample Name	version	run range
HLT_Ele25_CaloIdVT_TrkIdT_CentralTriJet30	v1–v3	160404-163869
HLT_Ele25_CaloIdVT_TrkIdT_TriCentralJet30	v3	165088-165633
HLT_Ele25_CaloIdVT_CaloIsoT_TrkIdT_TrkIsoT_TriCentralJet30	v1–v5	165970-178380
HLT_Ele25_CaloIdVT_CaloIsoT_TrkIdT_TrkIsoT_TriCentralPFJet30	v2, v3	178420-180252

Primary Vertex Selection: There is no pre-selection in the differential cross section measurement. Events are selected with at least one good quality primary vertex as defined in Section 5.3.1.

Electron Selection: After the primary vertex selection, we also require exactly one isolated PF electron which follows the requirement in Section 5.3.1, but with electron $p_T > 30$ GeV. Meanwhile, the photon conversion rejection is not treated in a separate step but included in the election selection.

Dilepton Veto: In this step, muon veto as described in Section 5.3.1 is applied first. Then we reject events containing one or more loose electrons. The definition of loose electrons are the same as the one in Z veto, see Section 5.3.1.

Jet Selection: The selection criteria for jet candidates is almost the same as that in Section 5.3.1, but the threshold on jet p_T is raised to 35 GeV in order to be on the plateau of the HLT turn on curve. Events are required to have at least three selected PF jets.

b **Jet Tagging:** In the final state, at least two *b*-tagged jets is required. The combined secondary vertex *b*-tagging is applied and the medium working point (0.679) is chosen, which is explained in Section 4.6.

5.3.3 MC Events Reweighting

5.3.3.1 Pileup Reweighting

Pileup events are the additional interactions in each bunch crossing due to the high instantaneous luminosity. There were an average of ~ 15 pileup events per bunch crossing by the end of the 2011 run. The pileup distribution has been produced assuming a minimum bias cross section of 68 mb (taken from PYTHIA samples), which is the recommended value to be considered for 2011. However, the number of simulated pileup interactions cannot represent the real conditions due to the constant change of the luminosity. Therefore a reweighting procedure is performed only using the estimated number of in-time pileup interactions[3] per luminosity block, following the official recommendation [110]. The out-of-time pileup interaction[4] intrinsic of the Summer11/Fall11 MC production has been done for a pileup scenario similar to the 2011 running conditions. A total uncertainty of 5% covers the uncertainty from luminosity, total inelastic cross section and the physics modeling of pileup simulation.

The distribution of the number of primary vertices is sensitive to the pileup effect as events with two or more primary vertices are more likely to contain multiple interactions. Fig. 5.6 shows the distributions of the number of offline primary vertices before and after

[3] In-time pile interaction refers to the interactions that occur in the bunch-crossing firing the triggers.

[4] Out-of-time pileup interaction refers the interaction that occurs in a bunch-crossing earlier or later than the in-time interaction.

applying the pileup reweighting in e+jets measurement. The agreement with data in the offline primary vertices distribution is much improved by the pileup reweighting.

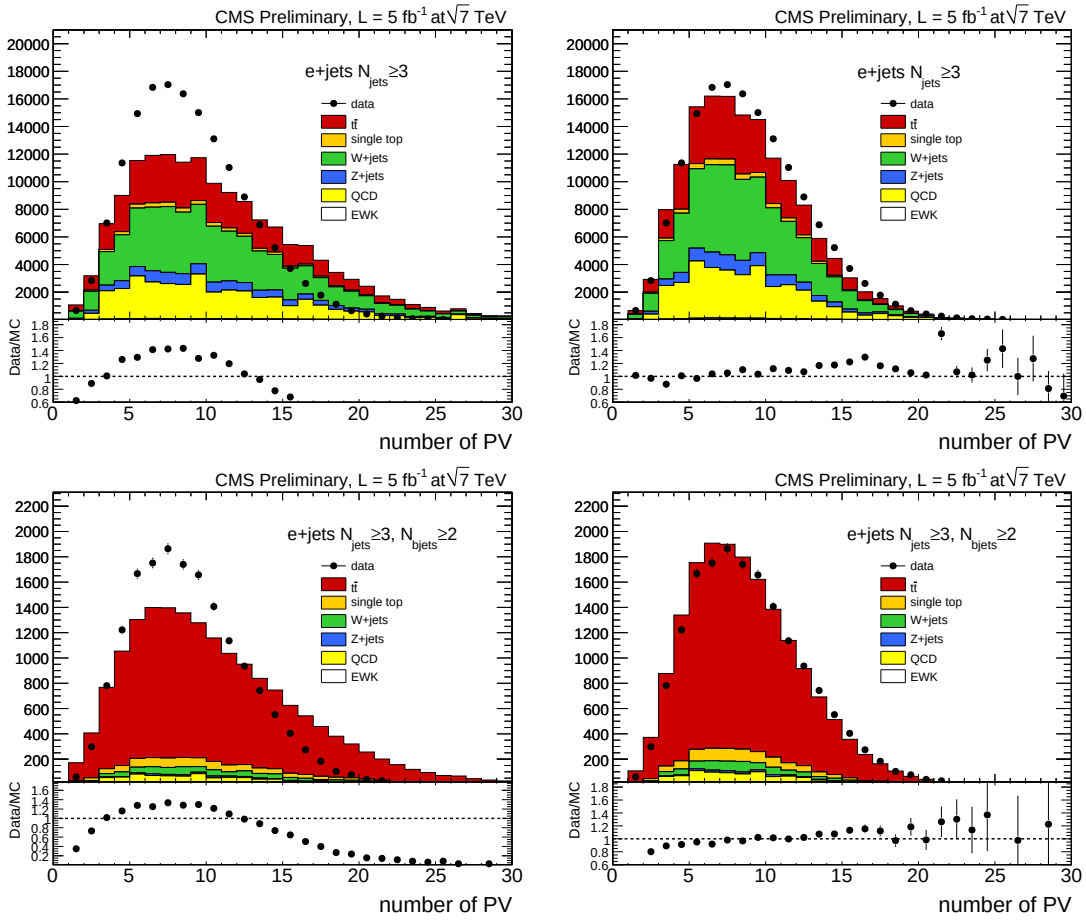

Figure 5.6: Top plots show the Data and MC comparison of the number of primary vertices for events passing the full event selection without b-tagging before (left) and after (right) applying pileup reweighting. The bottom plots show the same distributions with events passing the full event selection with b-tagging.

5.3.3.2 Electron Trigger Efficiency and ID/Isolation Efficiency

Tag-and-probe methods have been employed in the CMS TOP group to determine the electron trigger efficiency and selection efficiency (ID and isolation). In this method,

$Z \rightarrow ee$ events are selected from data by looking for a pair of electrons within an invariant mass close to the Z boson (91.2 GeV). A tag electron is required to pass all electron selections as well as trigger the events, another probe electron is selected using looser requirements. Using a sample of events containing both electrons, the efficiency is the ratio of the number of probes further passing selections (trigger or ID/isolation) divided by the number of total probes. This method is applied on both data and simulation to measure the electron efficiency, the difference is then taken as the scale factor to correct the simulation.

In the cross section measurement, we refer to the tag-and-probe efficiencies determined in [111]. A data-to-MC scale factor of 0.96 is then applied to the MC to account for differences in the single electron trigger efficiency (0.975 ± 0.015) and identification plus isolation (0.985 ± 0.025). In the differential cross section measurement, the leptonic and hadronic leg of the electron plus jets cross triggers are measured separately in another study [112]. A comparable single electron trigger HLT_Ele32_CaloIdVT_CaloIsoT_TrkIdT_TrkIsoT is used for the leptonic leg study, as HLT_Ele25 with the same ID and isolation requirement is not available in the later 2011 data taking period. For the haronic leg, events are required to pass the full event selection and the single electron trigger (HLT_Ele32), the efficiency of jet with N^{th} highest p_T in such events is measured for a HLT_Ele25_NCentralJet30 cross-trigger. Both are fully efficient, the scale factor is approximately close to 1 with a total of 1% uncertainty. The scale factors of electron selection (ID/isolation) with respect to η are applied on MC with 3% systematic uncertainty, also taken from [112].

5.3.3.3 b Jet Tagging Efficiency Modeling

Unlike pileup, trigger and electron selection efficiency, which are applied in both cross section analysis, the b-tagging efficiency modeling is only considered in the differential cross

section measurement. The measurements of the jet tagging efficiency in the 2011 datasets are undertaken by the B-Tagging and Vertexing Physics Object Group (B-Tagging POG). b-tagging scale factors that characterize the difference between the measured performance in data and the simulated performance in MC. They were found to be approximately constant in p_T range for both the forward and central regions of the detector [88][113].

The formula for the b-tagging scale factor SF_b for the CSVM tagger is given by Eq. 5.1, with the uncertainties listed in Tab. 5.6. Jets with $p_T > 670$ GeV are assigned a b-tagging uncertainty twice that of jets with 500 GeV $< p_T <$ 670 GeV. The scale factor for charm quark SF_c is the same as that for bottom ($SF_c = SF_b$) with twice the quoted uncertainty in Tab. 5.6. The scale factor for the light jet SF_l is studied as a function of jet p_T for several η bins, details are in [114]. Based on these studies, the efficiency with which each individual jet is identified as a b jet, ϵ_x (where x refers to the parton flavour: b, c, or $l \equiv u, d, s, g$) is obtained from MC and then corrected by the scale factors. The uncorrected efficiencies from $t\bar{t}$ and W+jets MC are shown in Fig. 5.7.

$$SF_b = 0.6981 \times \frac{1 + 0.414063 \times p_T}{1 + 0.300155 \times p_T} \tag{5.1}$$

Table 5.6: The uncertainties of SF_b for the CSVM tagger listed in [113] in bins of jet p_T.

jet p_T (GeV)	$30-40$	$40-50$	$50-60$	$60-70$	$70-80$
σ_{SF_b}	0.0295675	0.0295095	0.0210867	0.0219349	0.0227033
jet p_T (GeV)	$80-100$	$100-120$	$120-160$	$160-210$	$210-260$
σ_{SF_b}	0.0204062	0.0185857	0.0256242	0.0383341	0.0409675
jet p_T (GeV)	$260-320$	$320-400$	$400-500$	$500-670$	>670
σ_{SF_b}	0.0420284	0.0541299	0.0578761	0.0655432	0.1310864

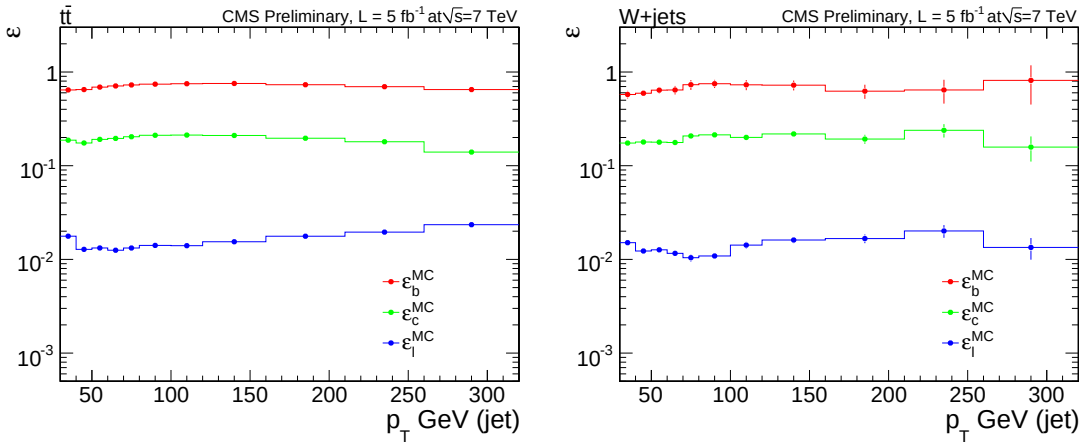

Figure 5.7: Jet tagging efficiency for b, c and light jets vs p_T for the CSV algorithm at the medium working point (discriminant > 0.679) for the $t\bar{t}$ (left) and W+jets (right) MC sample.

At the event level, we require two or more jets to be tagged in this manner. The probability to tag zero and one jet in an event is given by Eq. 5.2 and 5.3,

$$P(0 \text{ tag}) = \prod_{i}^{N_{\text{jets}}} (1 - \epsilon_i) \tag{5.2}$$

$$P(1 \text{ tag}) = \sum_{i}^{N_{\text{jets}}} \epsilon_i \prod_{j;\, j \neq i}^{N_{\text{jets}}} (1 - \epsilon_j) \tag{5.3}$$

where N_{jets} is the total number of jets in the event, and ϵ_i is the jet tagging efficiency. In the probability model, the efficiency to tag two or more jets is then given by Eq. 5.4,

$$\begin{aligned} P(\geq 2 \text{ tag}) &= 1 - P(1 \text{ tag}) - P(0 \text{ tag}) \\ &= 1 - \sum_{i}^{N_{\text{jets}}} \epsilon_i \prod_{j;j \neq i}^{N_{\text{jets}}} (1 - \epsilon_j) - \prod_{k}^{N_{\text{jets}}} (1 - \epsilon_k) \end{aligned} \tag{5.4}$$

For every event passing the 2 b-tag selection a tagging weight is applied on each event as following:

$$w = P^{\text{data}}(\geq 2 \text{ tag}) / P^{\text{MC}}(\geq 2 \text{ tag}), \tag{5.5}$$

where $P^{\text{data}}(\geq 2 \text{ tag})$ ($P^{\text{MC}}(\geq 2 \text{ tag})$) is calculated via Eq. 5.4 with (without) jet tagging efficiency ϵ_i corrected by the scale factor SFs. The uncertainty on the b-tagging SFs

quoted in Tab. 5.6 are taken into account as systematic uncertainty. To test the probability model, a "closure test" is performed on the $t\bar{t}$ MC, shown in Fig. 5.7. The selected events without applying b tagging are multiplied by the tagging weight defined in Eq. 5.5, and plotted in the red dot (called "$t\bar{t}$ counted"). The blue dot (called "$t\bar{t}$ reconstructed") is for the selected events which pass the b tagging requirement. The overall difference between the "$t\bar{t}$ counted" and "$t\bar{t}$ reconstructed" events is only around 0.2%.

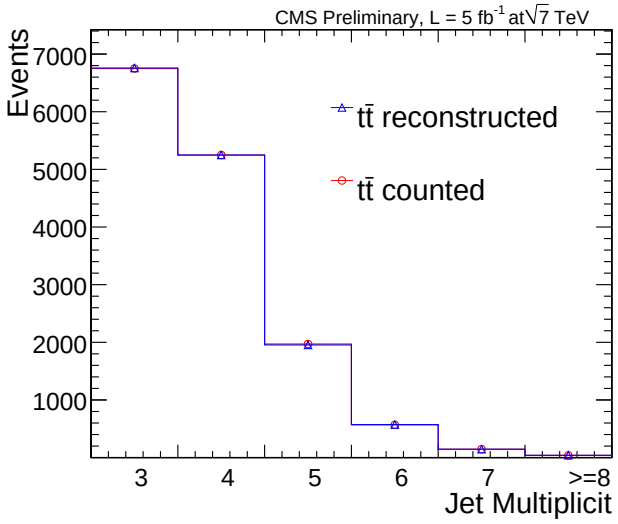

Figure 5.8: Jet multiplicity distribution of $t\bar{t}$ events passing full event selection. "counted" ("reconstructed") is for events with (without) applying the tagging weight.

5.3.4 Data and MC Comparison

After applying the weights on MC processes, as described in Section 5.3.3, we compare data and MC events after each selection cut. Tab. 5.7 and 5.9 show the expected number of each MC process after scaling to 857.7 pb^{-1} and 5 fb^{-1} respectively. Tab. 5.8 and 5.10 show a comparison of the observed number of events in data and total number of events expected from MC normalized to 857.7 pb^{-1} and 5 fb^{-1} respectively. In the differential cross section measurement, the signal is counted in each jet bin, therefore we compare the data and MC

of events passing the offline event selection in $N_{\text{jets}} = 3,\ 4,\ 5,\ 6,\ 7,\ \geq 8$, as shown in Tab. 5.11. Notice that dominant backgrounds such as QCD and W+jets are heavily suppressed after requiring at least two b-tagged jets in the final state.

Table 5.7: Event numbers of $t\bar{t}$ signal, single top, W+jets, Z+jets and QCD backgrounds surviving after each selection which are normalized to 857.7 pb^{-1}, only the statistic errors are quoted.

	$t\bar{t}$	W+jets	Z+jets	single top	QCD
PreSel.	9925.7 ± 19.4	483641 ± 496.5	189831 ± 119.3	2327.2 ± 4.8	179235 ± 4558.9
==1 ISO ele	8954.0 ± 18.4	455749 ± 481.9	164863 ± 111.1	2275.7 ± 4.7	97716.5 ± 3396.0
μ Veto	8032.1 ± 17.5	455719 ± 481.9	164718 ± 111.1	2227.7 ± 4.7	97701.1 ± 3395.9
Z Veto	7927.8 ± 17.3	455702 ± 481.9	69024.2 ± 71.9	2216.6 ± 4.7	97701.1 ± 3395.9
γ Con rej	7707.2 ± 17.1	442243 ± 474.7	66727.2 ± 70.7	2154.8 ± 4.6	75047.6 ± 2958.7
≥ 3 jets	5621.9 ± 14.6	10437 ± 72.9	2298.7 ± 13.1	583.9 ± 2.4	3810.8 ± 525.3

Table 5.8: Number of obsereved and expected events in a data sample of 857.7 pb^{-1}, only the statistic errors are quoted. The number in the brackets show the relative cut efficiency.

# Events	Data	Total MC
PreSel.	997601 ± 998.8	865130 ± 4587.4
==1 ISO ele	850551 ± 922.3 (0.85)	729609 ± 3431.8 (0.84)
μ Veto	848941 ± 921.4 (0.998)	728397 ± 3431.8 (0.998)
Z Veto	753097 ± 867.8 (0.89)	632572 ± 3430.8 (0.87)
γ Con rej	680127 ± 824.7 (0.90)	593880 ± 2997.4 (0.94)
≥ 3 jets	25533 ± 159.8 (0.04)	22752.3 ± 530.7 (0.04)

Fig. 5.9 shows the data-MC comparison plots of jet multiplicity distributions, p_T and η of isolated electrons (jets), and missing transverse energy, all MC processes are normalized to 857.7 pb^{-1}. Similar plots are made for the 2011 full datasets, as shown in Fig. 5.10 and 5.10. Data is always larger than MC predication before applying b-tagging due to the fact that we do not simulate enough QCD events (but this background is estimated from data). After using b-tagging, data and MC have a good agreement.

Table 5.9: Event numbers of $t\bar{t}$ signal, single top, W+jets, Z+jets and QCD backgrounds surviving after each selection. The numbers are normalized to 5.0 fb^{-1}, only the statistical errors are quoted.

	$t\bar{t}$	single top	W+jets	Z+jets	QCD	EWK
==1 Iso ele	46647.5 ± 25.7	3999.6 ± 17.5	58643.6 ± 339.2	20960.2 ± 94.9	34774.1 ± 2746.2	1331.6 ± 7.6
muon veto	43798.6 ± 24.9	3892 ± 17.2	58595.8 ± 339.1	20876.8 ± 94.7	34774.1 ± 2745	1305.4 ± 7.5
loose electron veto	42619.6 ± 24.6	3845.5 ± 17.1	58503.8 ± 338.8	10129.3 ± 65.9	34641.6 ± 2735.1	1146.8 ± 7.3
b-tagging	14720.7 ± 14.5	917.7 ± 8.1	648.8 ± 35.7	140.4 ± 7.8	904.5 ± 259.9	25.5 ± 0.9

Table 5.10: Number of observed and expected events in a data sample of 5.0 fb^{-1} in the measurement, only the statistical errors are quoted. The number in the brackets show the relative cut efficiency.

# Events	Data	Total MC
==1 Iso ele	174323 ± 417.5	166357 ± 2768.9
muon veto	$171266 \pm 413.8(98.2\%)$	$163243 \pm 2767.7(98.1\%)$
loose electron veto	$158118 \pm 397.6(92.3\%)$	$150887 \pm 2757(92.4\%)$
b-tagging	$16966 \pm 130.3(10.7\%)$	$17357.6 \pm 263(11.5\%)$

Table 5.11: The table shows the number of events passing the offline event selection in $N_{\text{jets}} = 3,\ 4,\ 5,\ 6,\ 7,\ \geq 8$, MC samples are normalized to 5.0 fb^{-1}

	$t\bar{t}$	single top	W+jets	Z+jets	QCD	EWK	Total MC	Data
3	6737 ± 9.8	599 ± 6.4	463.4 ± 30.2	98.4 ± 6.5	904.5 ± 449.3	18.7 ± 0.8	8821 ± 450.5	8297 ± 91.1
4	5272.5 ± 8.7	236.8 ± 4.2	135.3 ± 16.3	33.2 ± 3.8	0.0 ± 0.0	5.5 ± 0.4	5683.3 ± 19.3	5836 ± 76.4
5	1968.2 ± 5.3	63.6 ± 2.3	41.4 ± 9	6.4 ± 1.7	0.0 ± 0.0	1.0 ± 0.2	2080.6 ± 10.8	2113 ± 46
6	565.1 ± 2.8	15.1 ± 1.2	8.7 ± 4.1	2.1 ± 0.9	0.0 ± 0.0	0.2 ± 0.1	591.2 ± 5.2	562 ± 23.7
7	$140. \pm 1.4$	3.0 ± 0.5	0.0 ± 0.0	0.3 ± 0.4	0.0 ± 0.0	0.1 ± 0.1	143.4 ± 1.6	126 ± 11.2
≥ 8	37.8 ± 0.7	0.2 ± 0.1	0.0 ± 0.0	0.0 ± 0.0	0.0 ± 0.0	0.0 ± 0.0	38 ± 0.7	32 ± 5.7

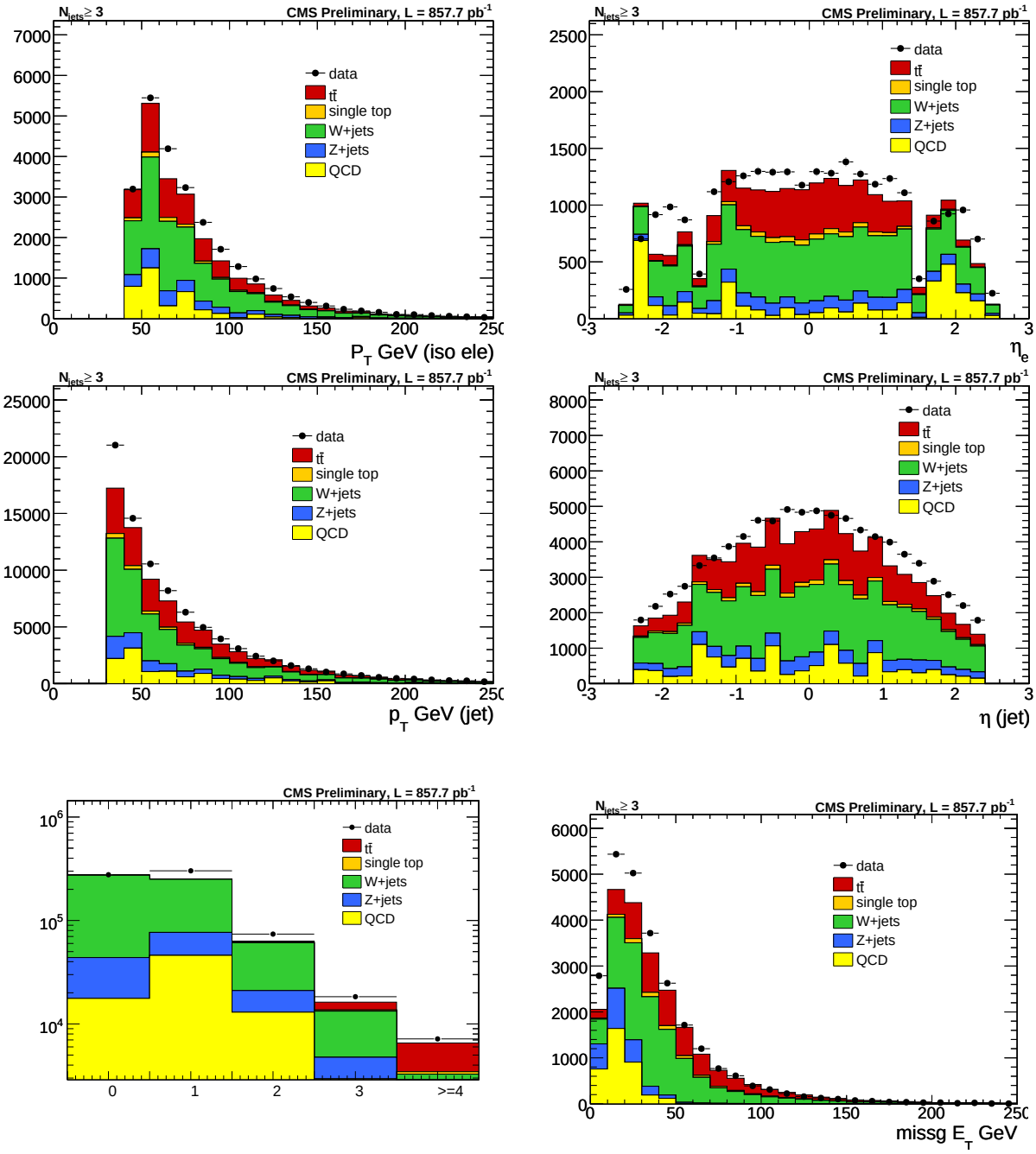

Figure 5.9: Data-MC comparison of jet multiplicity and different kinematic variables for events passing the full event selection, MC events are normalized to 857.7 pb^{-1}.

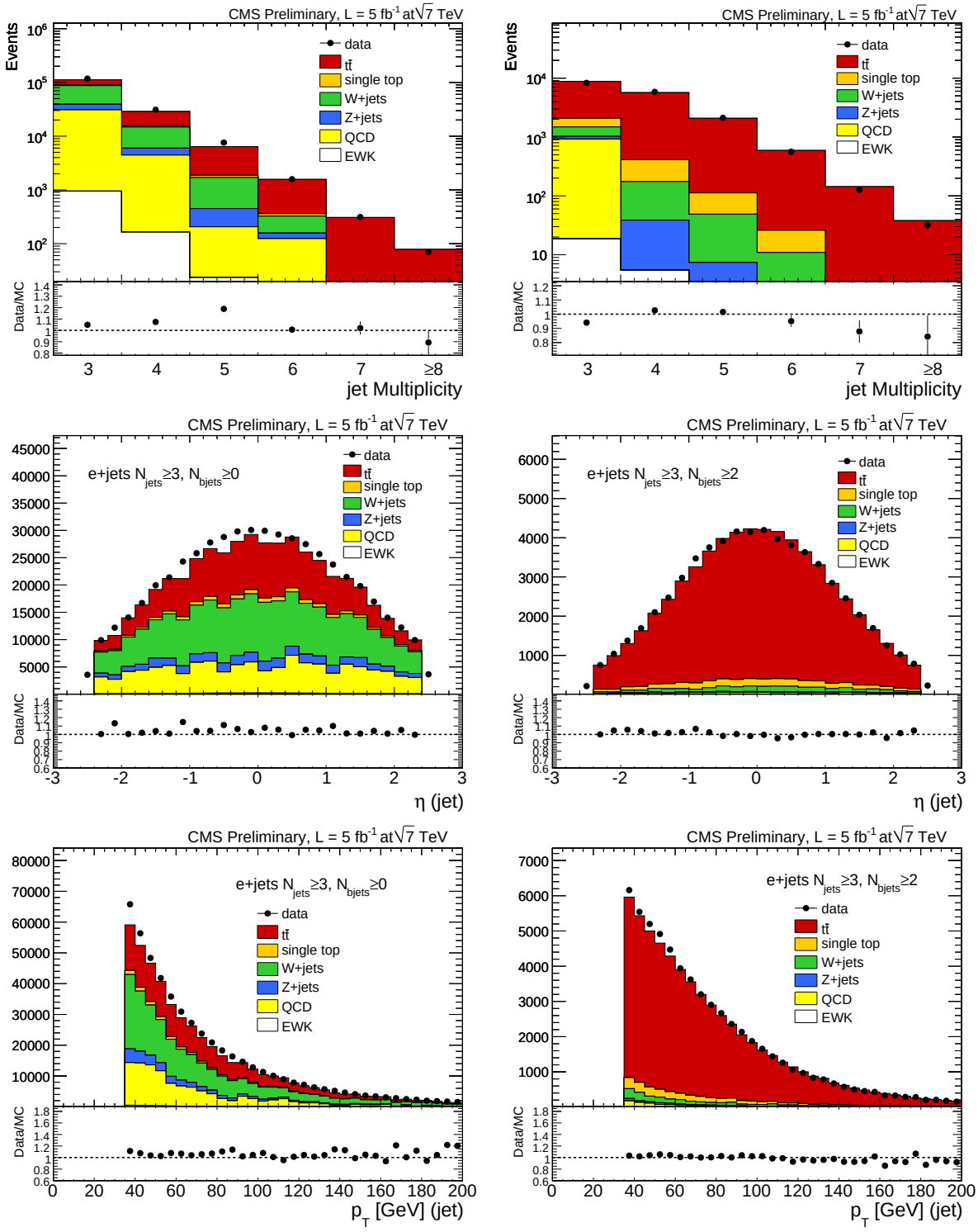

Figure 5.10: Data-MC comparison of jet multiplicity and different kinematic variables. MC events are normalized to 5 fb^{-1}. In the left (right) plot, the events pass the full event selection without (with) requiring at least two b-tagged jets.

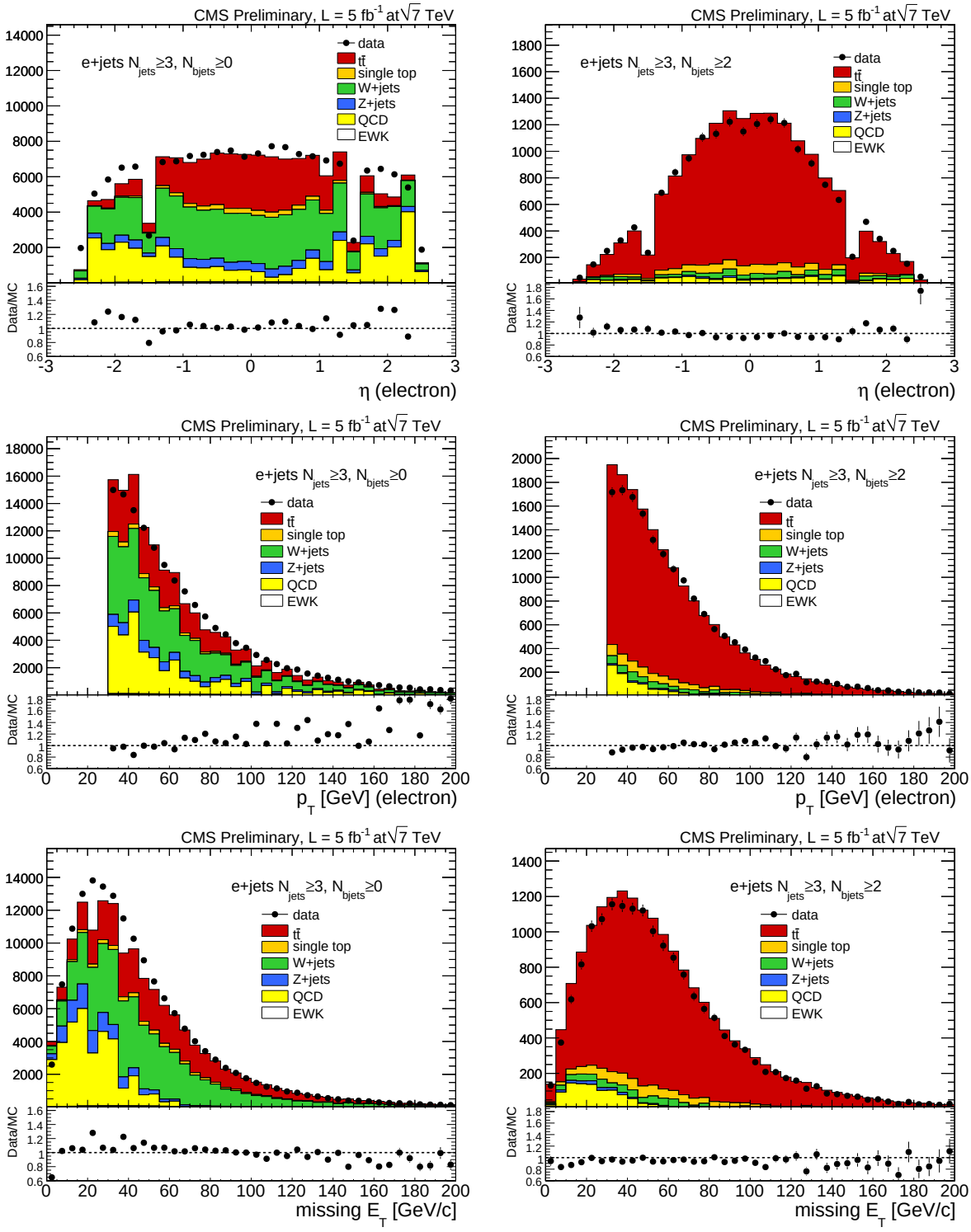

Figure 5.11: Data-MC comparison of different kinematic variables. MC events are normalized to 5 fb^{-1}. In the left (right) plot, the events pass the full event selection without (with) requiring at least two b-tagged jets.

CHAPTER 6

Top Pair Cross Section Measurement

The top pair cross section is extracted by fitting a discriminant distribution $|\eta_e|$ in data using a superposition of templates of signal and backgrounds, where $|\eta_e|$ is the absolute pseudorapidity distribution (explained in Section 3.2) of isolated electrons. In $t\bar{t}$ and single top events, electrons are prompt, i.e. very isolated and have large p_T. They are more likely to travel in the barrel region of the tracker system and be stopped in EB. $|\eta_e|$ of $t\bar{t}$ thus peaks at zero and decreases drastically along $|\eta_e|$. We therefore treat the $t\bar{t}$ and single top together as the signal in the template fit. However, electrons in W+jets and Drell-Yan processes tends to be produced uniformly in all directions, resulting in a flat $|\eta_e|$ distribution. Most electrons in QCD events are "soft" and move towards to the forward region, leading to a maximum in the large $|\eta_e|$ region.

Based on the difference of $|\eta_e|$ between signal and backgrounds, we measure the $t\bar{t}$ cross section by applying a binned likelihood fit on $|\eta_e|$ distribution of data which pass the event selections described in Section 5.3.1. We minimize the logarithm of the likelihood (LL) defined as following:

$$LL(\{\lambda_i, d_i\}) = -2 \log \left(\prod_i \frac{\lambda_i^{d_i} \cdot e^{-\lambda_i}}{d_i!} \right) = -2 \sum_i \log \left(\frac{\lambda_i^{d_i} \cdot e^{-\lambda_i}}{d_i!} \right), \tag{6.1}$$

where the sum runs over all bins of the distribution and λ_i (d_i) are the expected (observed) number of events in each bin i. The expected pseudorapidity distribution λ_i is modeled by process-dependent templates $\theta_j := \{\theta_j^i\}$ i.e. $j = t\bar{t}$, single top, W+jets, Drell-Yan, QCD;

and normalization factors N_j, such that

$$\lambda_i = \sum_j N_j \theta_j^i, \text{ with } \sum_i \theta_j^i = 1 \; \forall \, \text{process } j. \tag{6.2}$$

The free parameters are the normalization factors for each contributing process, i.e. top processes ($t\bar{t}$ and single top, N_{top}), W+jets ($N_{\text{W+jets}}$), Drell-Yan process (N_{DY}) and QCD (N_{QCD}). In the likelihood fit, we assign Gaussian constraints on the ratio of N_{DY} to $N_{\text{W+jets}}$ within 5% uncertainty of its expected value, as well as N_{QCD} within 100% of its MC prediction. These constraints allow the fit to give a physically reasonable estimation of each parameter while ensure that N_{QCD}, $N_{\text{W+jets}}$ and N_{DY} are mainly determined from the data. The constrained terms are the following

$$\frac{\left(N_{\text{DY}}/N_{\text{W}} - N_{\text{DY}}^{\text{MC}}/N_{\text{W}}^{\text{MC}}\right)^2}{(0.05 \cdot N_{\text{DY}}^{\text{MC}}/N_{\text{W}}^{\text{MC}})^2} + \frac{\left(N_{\text{QCD}} - N_{\text{QCD}}^{\text{MC}}\right)^2}{(1 \cdot N_{\text{QCD}}^{\text{MC}})^2} \tag{6.3}$$

The number of signal events $N_{t\bar{t}}^{\text{fit}}$ is obtained by subtracting the single top events ($N_{\text{single-top}}^{\text{MC}}$) from the fitted number of top-like events N_{top}. Based on a frequentist procedure, we build pseudo experiments to extract $t\bar{t}$ cross section using $N_{t\bar{t}}^{\text{fit}}$, at the same time we extract the systematic and statistic uncertainty.

In Section 6.1, different data driven methods, developed to estimate $|\eta_e|$ from dominant background processes, are presented. The main sources of systematic uncertainties are discussed in Section 6.2. The frequentist procedure is introduced in Section 6.3 and the final results and intepretation are detailed in Section 6.4.

6.1 Construction of Fit Templates

One problem that arises with the template fitting method is how to select clean background templates. Below I outline the methods for extracting templates for various backgrounds.

6.1.1 W+jets Template

LHC is a pp collider, therefore it produces more W^+ than W^-. Unlike the signal and other backgrounds which have almost equal contribution from electrons and positrons, W+jets background contains more positrons than electrons. Based on this charge asymmetry property, we can extract a relatively pure W+jets sample from data by subtracting the distribution of $|\eta_{e^-}|$ from $|\eta_{e^+}|$. The charge subtraction distribution Δ_e^i, and charge sum Σ_e^i distribution which corresponds to W+jets template after normalization, are defined as following:

$$\Delta_e^i = \#(|\eta_{e^+}|)^i - \#(|\eta_{e^-}|)^i, \quad \Sigma_e^i = \#(|\eta_{e^+}|)^i + \#(|\eta_{e^-}|)^i, \tag{6.4}$$

where $\#(.)^i$ denotes the number of events in the i^{th} bin of either $|\eta_{e^+}|$ or $|\eta_{e^-}|$. In order to derive Σ_e^i from Δ_e^i, we should correct Δ_e^i by a bin-by-bin correction factor c_W^i such that the product of Δ_e^i and c_W^i is Σ_e^i ($\Sigma_e^i = c_W^i \times \Delta_e^i$). Accordingly, c_W^i is constructed as

$$c_W^i = \left(1 + \frac{2}{R_i - 1}\right), \tag{6.5}$$

where R_i is defined as the ratio of the expected rate of W^+ to W^- in i^{th} bin,

$$R_i = \left(\frac{d\sigma_{\mathrm{W^+}}}{d|\eta_\mu|}\right)_i \left(\frac{d\sigma_{\mathrm{W^-}}}{d|\eta_\mu|}\right)_i^{-1}. \tag{6.6}$$

Eq. 6.6 can be simplified by using normalized differential distributions $d\tilde{\sigma}/d\eta_e$, the overall cross section ratio $R = \sigma_{W^+}/\sigma_{W^-}$, and the ratio of the efficiencies $\rho_\varepsilon = \varepsilon_{W^+}/\varepsilon_{W^-}$, as

$$R_i = R\frac{\varepsilon_{W^+}}{\varepsilon_{W^-}} \left(\frac{d\tilde{\sigma}_{W^+}}{d|\eta_e|}\right)_i \left(\frac{d\tilde{\sigma}_{W^-}}{d|\eta_e|}\right)_i^{-1} = R\,\rho_\varepsilon\,\rho_i, \tag{6.7}$$

where the ratio of the normalized differential cross sections ρ_i is defined as $\left(\frac{d\tilde{\sigma}_{W^+}}{d|\eta_e|}\right)_i \left(\frac{d\tilde{\sigma}_{W^-}}{d|\eta_e|}\right)_i^{-1}$. Then the correction factor c_W^i becomes $c_W^i = \left(1 + \frac{2}{R\rho_\varepsilon\rho_i - 1}\right)$.

R is found to be dependent on jet multiplicity [115][116]. In different decay modes, there is $10\% - 20\%$ difference between measuring R in $N_{\text{jets}} \geq 1$ and $N_{\text{jets}} \geq 3$ [116]. As

the template in $N_{\text{jets}} \geq 3$ is derived by using the charge subtraction in $N_{\text{jets}} = 1||2$, we therefore choose $R = 1.41 \pm 0.29\,(20.6\,\%)$ which is measured in $N_{\text{jets}} \geq 3$ [116]. Its inflated uncertainty is appropriate to cover the impact from the dissimilar kinematic regimes.

To estimate the shape-correction factor ρ_i and efficiency ratio, we use the NLO MC program MCFM [117] which is a parton level generator. The detector simulations and showering/hadronization effects are not considered, as such effects are cancelled out in the ratio. ρ_i and ρ_ε are calculated by running MCFM with the same cuts on electron p_T and η as in our event selection. Uncertainties on ρ_i and ρ_ε are much smaller than the uncertainty on R and thus are neglected. Fig. 6.1(a) and 6.1(b) show ρ_i and the correction factor c_W^i estimated from MCFM with uncertainties propagated from R, and their values are listed in Tab. 6.1. Notice that the magnitude of correction factor c_W^i reflects the fact that Δ_e^i has naturally less entries than Σ_e^i.

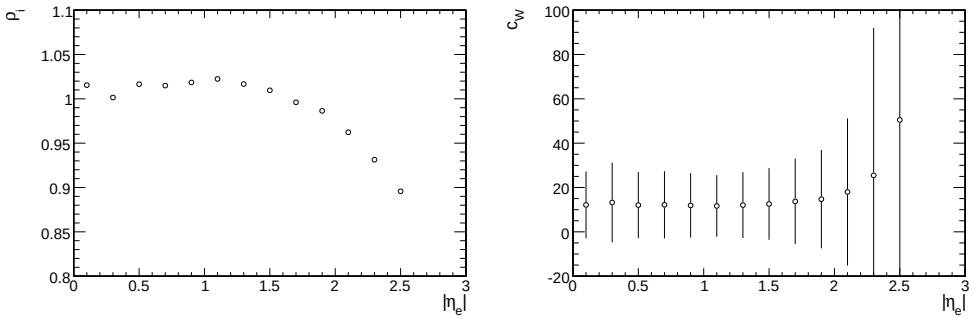

(a) (b)

Figure 6.1: 6.1(a) and 6.1(b) show the ratio of normalized differential cross sections ρ_i and correction factor c_W^i as a function of $|\eta_e|$.

Table 6.1: ρ_i and c_W^i used for the extraction of W+jets template.

Bin	1	2	3	4	5	6	7	8	9	10	11	12	13	≥ 14
ρ_i	1.015	1.001	1.017	1.015	1.018	1.022	1.017	1.010	0.996	0.986	0.962	0.931	0.896	0
c_W^i	12.145	13.2533	12.0647	12.1807	11.928	11.6598	12.0571	12.5815	13.7408	14.7186	17.9885	25.4515	50.474	0

Distributions of $|\eta_{e^+}|$ and $|\eta_{e^-}|$ for jet multiplicities $N_{\text{jet}} = 1||2$ are shown in Fig. 6.2(a) and 6.2(b), and for the multiplicities $N_{\text{jet}} \geq 3$ in Fig. 6.2(c) and 6.2(d). As already observed in Section 5.3.4, MC predictions underestimate data significantly. However, we are only interested in the template shape from data not the total normalization.

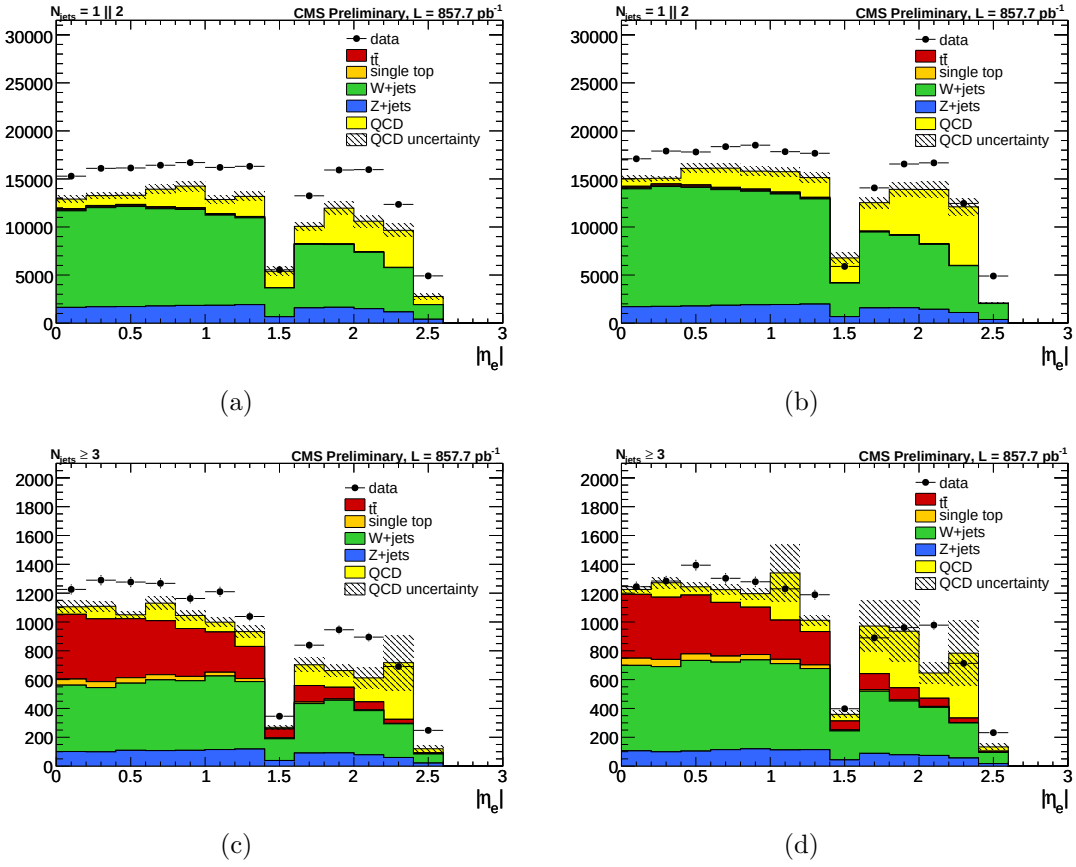

Figure 6.2: 6.2(a) (6.2(c)) and 6.2(b) (6.2(d)) show $|\eta|$ of negatively and positively charged electrons respectively in $N_{\text{jet}} = 1||2$ ($N_{\text{jet}} \geq 3$).

Distributions of Δ_W^i in $N_{\text{jet}} = 1||2$ and $N_{\text{jet}} \geq 3$ are shown in Fig. 6.3(a) and 6.3(b) respectively. After the subtraction, the agreement between data and MC is much better, indicating that the discrepancy between data and MC in $|\eta_{e^+}|$ and $|\eta_{e^-}|$ is not from a

wrong modeling of the W+jets background process. The large uncertainty comes from the limited statistics of QCD MC[1]. The data are consistent with the W+jets MC estimation.

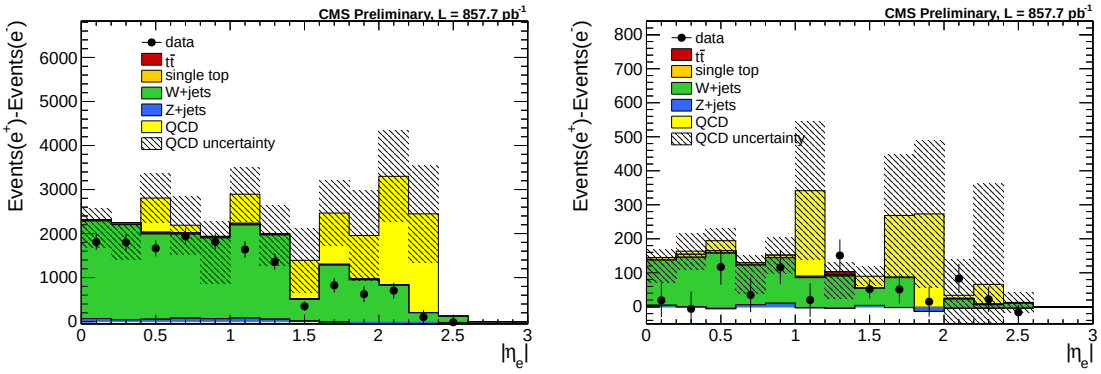

(a) (b)

Figure 6.3: 6.3(a) and 6.3(b) show distributions of Δ_W^i in $N_{\text{jet}} = 1||2$ and $N_{\text{jet}} \geq 3$ respectively.

Due to the limited statistics of Δ_W^i in $N_{\text{jet}} \geq 3$, Δ_W^i in $N_{\text{jet}} = 1||2$ is used to extract the W+jets template in the signal region ($N_{\text{jet}} \geq 3$). Additionally, the contamination from other processes are neglected as it is very small[2] compared to the statistical uncertainty of the observed data, and is largely dominated by the limited statistics of QCD MC. A "closure test" is firstly performed on MC to check the procedure of this method, where Δ_W^i from W+jets MC is multiplied by the correction factor c_W^i, and then compared with MC distributions of $|\eta_e|$ in $N_{\text{jet}} = 1||2$ and in $N_{\text{jet}} \geq 3$, as seen Fig. 6.4(a) and Fig. 6.4(b). The resulting template describes the actual shape very well within uncertainties. The closure test is considered as a validation of the template extraction procedure. The template is constructed using the same way. Fig. 6.4(c) and 6.4(d) show the comparison between W+jets template extracted from data in the $N_{\text{jet}} = 1||2$ charge-subtracted region and the MC predictions of W+jets process in $N_{\text{jet}} = 1||2$ and $N_{\text{jet}} \geq 3$ respectively. There is a good

[1]The simulated QCD events are ~ 100 times less than the theoretical prediction. It is indicated in Tab. 5.7. The statistic uncertainty should be $\sqrt{N_{\text{QCD}}} \sim 420$ if we simulated the same number of QCD events as the theoretical prediction. However, the uncertainty is 4558.9.

[2]From MC study, the contamination from other processes, except QCD, is around $\sim 2\% - 5\%$.

agreement. The W+jets template entries as well as the bin-wise uncertainties are listed in Tab. 6.2. Finally, it should be remarked that the shortcomings of this method such as large uncertainties due to limited statistics and possible systematic difference between shapes in different jet-multiplicities, will naturally disappear with increasing collected statistics.

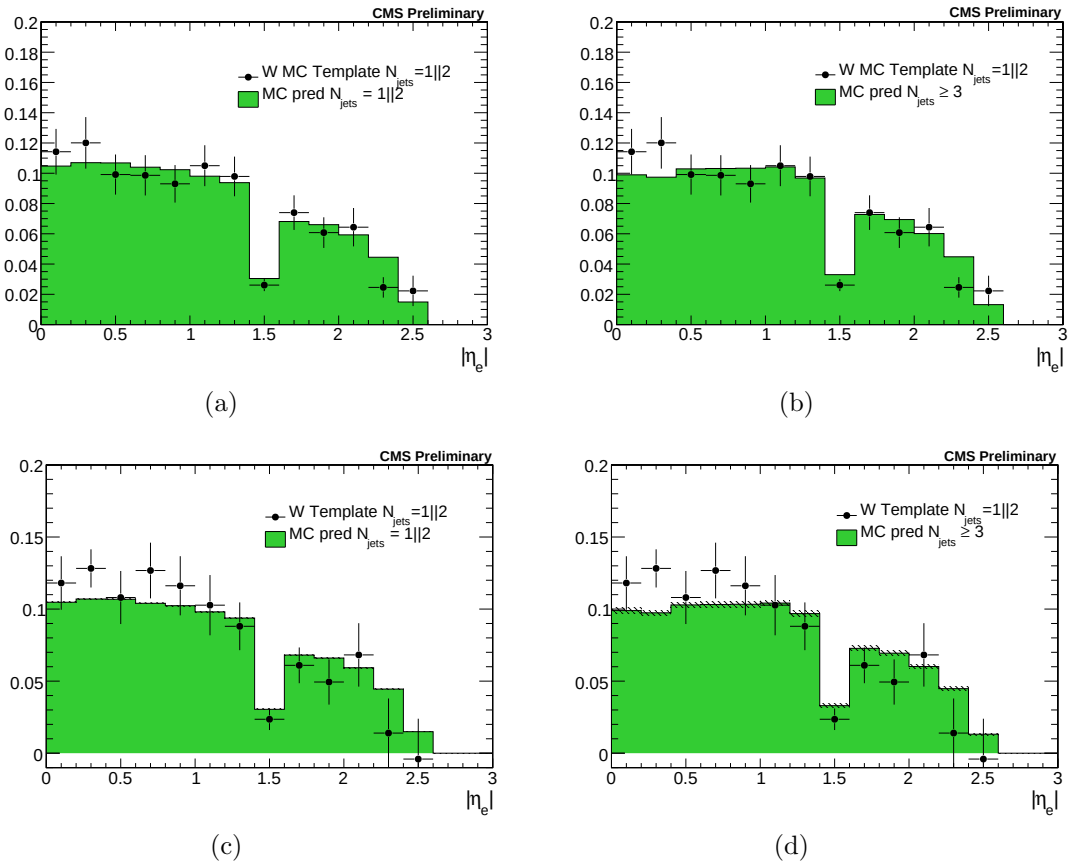

Figure 6.4: 6.4(a) and 6.4(b) show W+jets MC template extracted in $N_{\text{jet}} = 1||2$ and compared to MC predictions in $N_{\text{jet}} = 1||2$ and $N_{\text{jet}} \geq 3$. In 6.4(c) and 6.4(d), W+jets template is extracted from data in $N_{\text{jet}} = 1||2$.

Table 6.2: Entries and uncertainties of W+jets template.

Bin	1	2	3	4	5	6	7	8	9	10	11	12	13	≥ 14
Value	0.118	0.128	0.108	0.127	0.116	0.103	0.088	0.024	0.061	0.049	0.068	0.014	-0.004	0
unc. [%]	15.7	10.3	17.0	15.3	17.7	20.4	18.8	31.7	20.3	31.7	32.3	171.9	-687.7	0

6.1.2 QCD Template

Most electrons in QCD events are emitted along the beamline with small p_T and thus less isolated, therefore, a QCD sample can be extracted from data by inverting the relative isolation (relIso) criteria on the selected electron, i.e. instead of applying relIso<0.1, demanding relIso>0.2. Fig. 6.5(a) and 6.5(b) show the distribution of $|\eta_e|$ after inverting electron relIso requirement in $N_{\text{jets}} \geq 2$ and $N_{\text{jets}} \geq 3$ respectively, indicating the dominance of QCD process in these regions. The shape from the convert-isolation region has a peak around $1 < |\eta_e| < 1.4$ since the isolation selection is more effective around $|\eta_e| = 1.5$ and becomes less effective at large $|\eta_e|$[3]. We choose relIso>0.2 and $N_{\text{jets}} \geq 2$ as the control region since there is more statistics than in $N_{\text{jets}} \geq 3$ with the same relIso cut. Moreover, from MC predictions, the relative contamination from other processes is much smaller $(3\% - 6\%)$ than the uncertainty due to statistical limitations and rather stable along $|\eta_e|$, therefore, such contamination can be neglected.

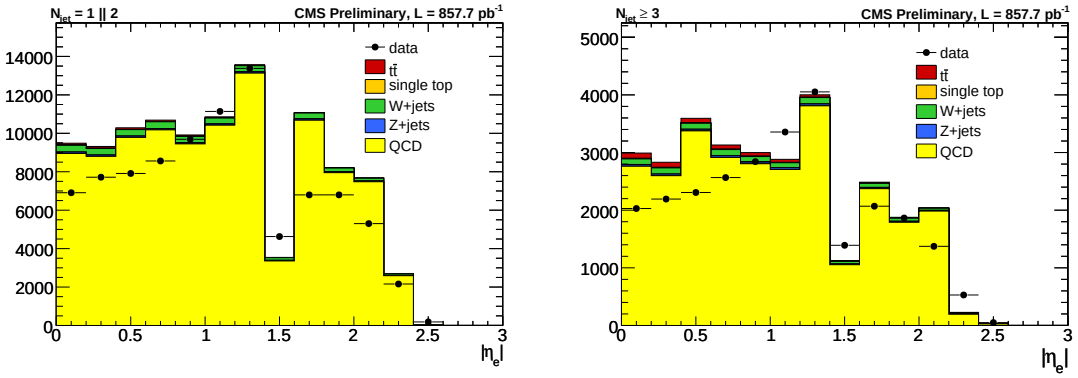

(a) (b)

Figure 6.5: 6.5(a) and 6.5(b) respectively show distributions of $|\eta_e|$ in $N_{\text{jet}} \geq 2$ and ≥ 3 with electron relIso>0.2.

The efficiency of the relative isolation selection ($\varepsilon_{\text{relIso}} = N^{\text{events}}_{\text{relIso}<0.1}/N^{\text{events}}_{\text{total}}$) increases

[3]This behavior of isolation selection is studied by looking at all six cuts in the electron selections [118][119]. The distributions of $|\eta_e|$ are plotted for electrons passing only five cuts and show that isolation selection is more effective around $|\eta_e| = 1.5$.

along $|\eta_e|$ since most electrons in QCD process are soft and move into the forward region, as seen in Fig. 6.6(a), as seen in Fig. 6.5. We therefore correct the distribution of $|\eta_e|$ taken in the control region by a correction factor $C_f = N^{\text{Events}}_{\text{relIso}<0.1}/N^{\text{Events}}_{\text{relIso}>0.2}$, where $N^{\text{Events}}_{\text{relIso}<0.1}$ is the number of events passing the offline event selection described in Section 5.3.1 in $N_{\text{jets}} \geq 2$, and $N^{\text{Events}}_{\text{relIso}} > 0.2$ is the number of events with relIso> 0.2, but keep all other cuts the same. This correction factor accounts for the difference of the relative isolation efficiency $\varepsilon_{\text{relIso}}(|\eta_e|)$ in the control and signal region. Fig. 6.6(b) shows C_f as a function of $|\eta_e|$.

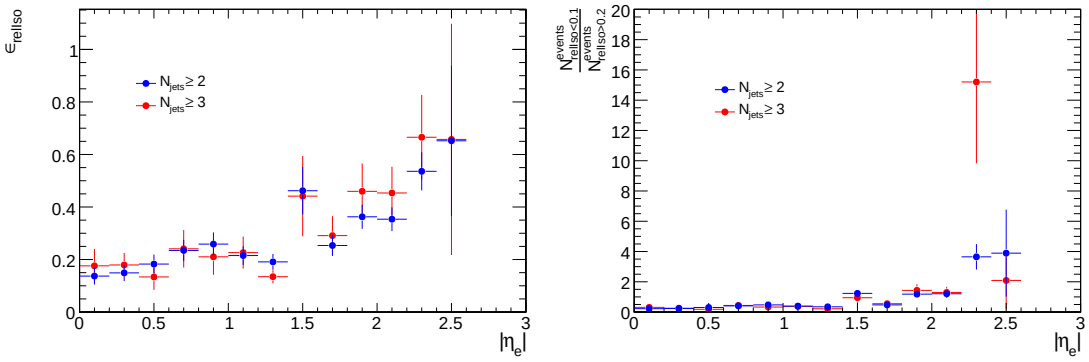

(a) (b)

Figure 6.6: 6.6(a) and 6.6(b) show $\varepsilon_{\text{relIso}}$ and C_f as a function of $|\eta_e|$ respectively.

The QCD template is obtained by normalizing the corrected distribution of $|\eta_e|$ in the control region. Fig. 6.7(a) and 6.7(b) compare the QCD data driven template with the MC predictions in $N_{\text{jets}} \geq 2$ and $N_{\text{jets}} \geq 3$, from which we can see a good agreement between data and MC. The normalized template entries, together with the uncertainties due to statistical limitations are show in Tab. 6.3.

Table 6.3: Entries and uncertainties of QCD template.

Bin	1	2	3	4	5	6	7	8	9	10	11	12	13	≥ 14
Value	0.028	0.033	0.044	0.064	0.084	0.079	0.085	0.104	0.059	0.147	0.117	0.144	0.013	0
Unc. [%]	23.1	20.4	19.4	16.5	16.2	15.7	14.9	18.7	15.9	13.2	14.5	19.7	73.3	0

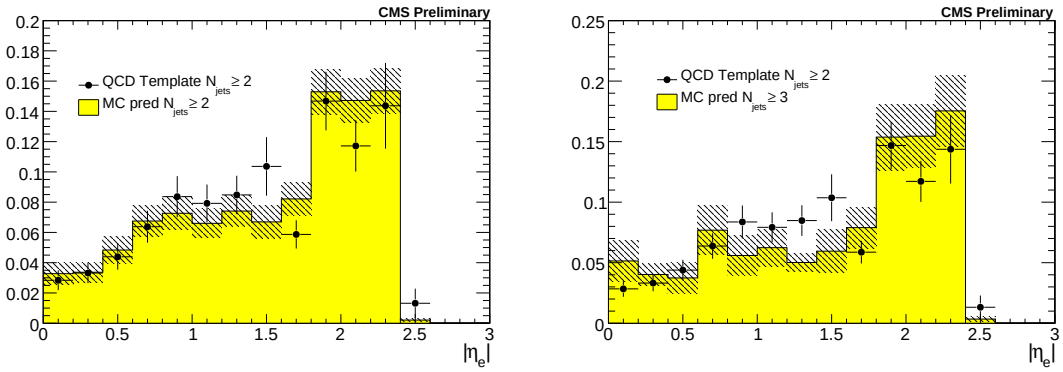

(a) (b)

Figure 6.7: QCD data driven template compared with MC prediction in $N_{\text{jet}} \geq 2$ (6.7(a)) and $N_{\text{jet}} \geq 3$ (6.7(b)).

6.1.3 Drell-Yan (Z+jets) Template

Drell-Yan events can be reconstructed from data by selecting electron pairs with invariant mass falling into the Z boson mass window. To select them, we invert Z veto cut described in Section 5.3.1. Event are required to have: i) one isolated electron with $p_T > 45$ GeV, $|\eta| < 2.5$, PF relIso< 0.1 and ii) invariant mass of isolated electron and another loose electron ($p_T >$20 GeV, PF relIso< 1.0) between $[76, 106]$ GeV. After inverting Z veto cut, distributions of $|\eta_e|$ in $N_{\text{jet}} = 1||2$ and $N_{\text{jet}} \geq 3$ are shown in Fig. 6.8(b) and 6.8(b). The plots show that the selection yields a pure Drell-Yan process with a $\sim 1\%$ contamination from other processes. To enhance statistics reason, the Drell-Yan template is fit in the $N_{\text{jet}} = 1||2$ region.

Since a "Z-veto" is applied on data in the offline event selection, the distribution of $|\eta_e|$ from Drell-Yan selection efficiency is then corrected by Z veto selection efficiency in each bin using MC, as shown in Fig. 6.8(c). The Drell-Yan template is obtained by normalizing the corrected distribution of $|\eta_e|$. Fig. 6.8(d) and 6.8(e) show the data driven Drell-Yan

template compared with MC predictions in $N_{\text{jets}} = 1||2$ and $N_{\text{jets}} \geq 3$ respectively, the entries and statistic uncertainties in each bin are listed in Tab. 6.4.

Table 6.4: Drell-Yan template entries and uncertainties.

Bin	1	2	3	4	5	6	7	8	9	10	11	12	13	≥ 14
Value	0.086	0.090	0.087	0.094	0.097	0.097	0.098	0.035	0.081	0.085	0.079	0.053	0.019	0
Unc. [%]	1.92	1.88	1.93	1.89	1.92	2.01	2.11	3.97	2.69	2.76	3.02	3.91	6.90	0

6.2 Systematic Uncertainties

6.2.1 Background Processes

Since the templates of all background processes are extracted from data with some theoretical predictions, the systematic uncertainties considered for the background estimation come from the statistical limitations of data, and theoretical predictions. All of them are uncorrelated, and summarized in the following:

- W+jets background: Each bin has i) a bin-wise uncorrelated uncertainty originated from statistical limitations of the charge subtraction method described in Section 6.1.1, and ii) uncertainty from the correction factor. The relative uncertainties per bin are shown in Tab. 6.2, with a typical range of $15\% - 30\%$.

- QCD background: The only uncertainty is the statistical uncertainty for each bin as listed in Tab. 6.3, which for most bins are greater than 15%.

- Drell-Yan background: The bin-wise uncorrelated uncertainties due to limited statistics and uncertainty of the correction factors are listed in Tab. 6.4, with a typically range between 0.2% and 0.5%.

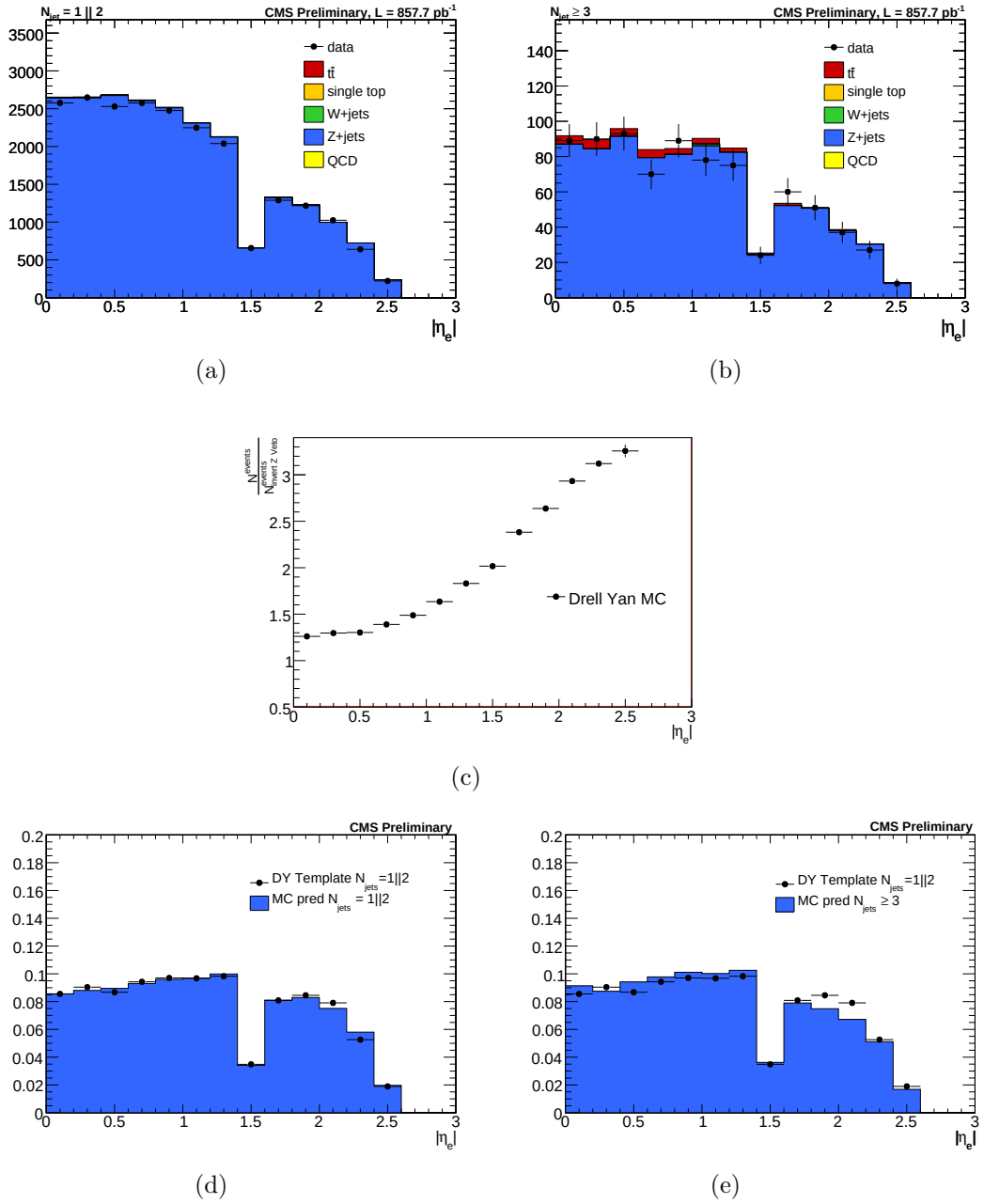

Figure 6.8: 6.8(a) and 6.8(b) are distributions of $|\eta_e|$ in $N_{\text{jet}} = 1||2$ and $N_{\text{jet}} \geq 3$ after inverting Z veto. 6.8(c) shows the correction factor C_f for $|\eta_e|$ from Drell-Yan selection. 6.8(d) and 6.8(e) show the comparison of the data driven Drell-Yan template with MC predictions in $N_{\text{jet}} = 1||2$ and $N_{\text{jet}} \geq 3$ respectively.

6.2.2 Signal Processes

We reply on MC predictions to obtain the template for signal processes ($t\bar{t}$ and single top) and various sources of systematic uncertainty are associated with the simulation. Tab. 6.5 summarizes the main sources and includes a brief description of the expected effect by check-marks, each of which will be discussed in details.

Table 6.5: Source of systematic uncertainties considered.

Source	Effect on $t\bar{t}$			Effect on single top		
	shape	efficiency	rate	shape	efficiency	rate
Jet energy scale (JES)	√	√		√	√	
Factorization scale (Q^2 scale)	√	√				
Matching threshold	√	√				
Single-Top xs						√
Luminosity			√			√

6.2.2.1 Jet Energy Scale (JES)

As explained in Section 4.4.2, the measured jet energy is different from the energy of its original particle, and so jet energy corrections have to be applied on the raw jet momenta to achieve a uniform jet energy response (or jet energy scale) in p_T and η. The uncertainty on the JES depends on jet p_T and η, which is approximately 3% in $|\eta| < 3$ [84]. This JES uncertainty has potentially an impact on both shapes of $t\bar{t}$ and single top templates, as well as on selection efficiencies. To understand these effects, we simultaneously vary four-momenta of all jets by either $+1\sigma$ or -1σ, where σ is the jet uncertainty provided for the standard jet energy corrections. We parametrize JES using a strength-parameter $\delta_{\text{JES}} \in [-1, +1]$, where $\delta_{\text{JES}} = +1(-1)$ corresponds to $+1\sigma$ (-1σ) variation of the jet momenta.

We first study the effect of varying JES scale on the predictions of $|\eta_e|$ for both $t\bar{t}$ and single top processes. The relative difference between the nominal JES and the varied values are shown in Fig. 6.9, where 6.9(a) is for $t\bar{t}$ process and 6.9(b) for single top process. In both cases the differences (points) are well below 1% and the uncertainty is actually driven by the limited statistics in the MC samples (colored bands). All observations are compatible with a zero hypothesis and thus we assume that the JES uncertainty does not affect the template shapes of signal.

The effect of varying JES on the selection efficiency for $t\bar{t}$ and single top processes are shown in Fig. 6.9(c) and 6.9(d) respectively. Three points show the ratio of efficiency to the nominal efficiency ($\delta_{\text{JES}} = 0$). This efficiency ratio is parametrized using a linear function, which gives a reasonable estimate of the efficiency ratio in this region. The resulting functional dependency for $t\bar{t}$ and single top is

$$\frac{\epsilon^{t\bar{t}}(\delta_{\text{JES}})}{\epsilon^{t\bar{t}}(0)} = 0.031\delta_{\text{JES}} + 0.999 \quad \frac{\epsilon^{\text{single-top}}(\delta_{\text{JES}})}{\epsilon^{\text{single-top}}(0)} = 0.062\delta_{\text{JES}} + 1.000 \tag{6.8}$$

When determining the full uncertainty using pseudo experiments, the above individual uncertainty will be included by picking a value for δ_{JES} normally distributed around 0 with a width of 1, and the resulting efficiency is computed using Eq. 6.8. The procedure will be detailed in Section 6.3.

6.2.2.2 Factorization Scale and Matching Threshold

To estimate systematic uncertainties due to the choice of the factorization scale (Q^2) and ME-PS matching threshold, we investigate their effects on the shape of $|\eta_e|$ and the selection efficiency for $t\bar{t}$ process by varying the corresponding parameters in MC simulations. Strength-parameters δ_P, $P \in \{Q^2, \text{th}\}$, are defined as

$$P(\delta_P) = P_0 \times e^{\delta_P} \tag{6.9}$$

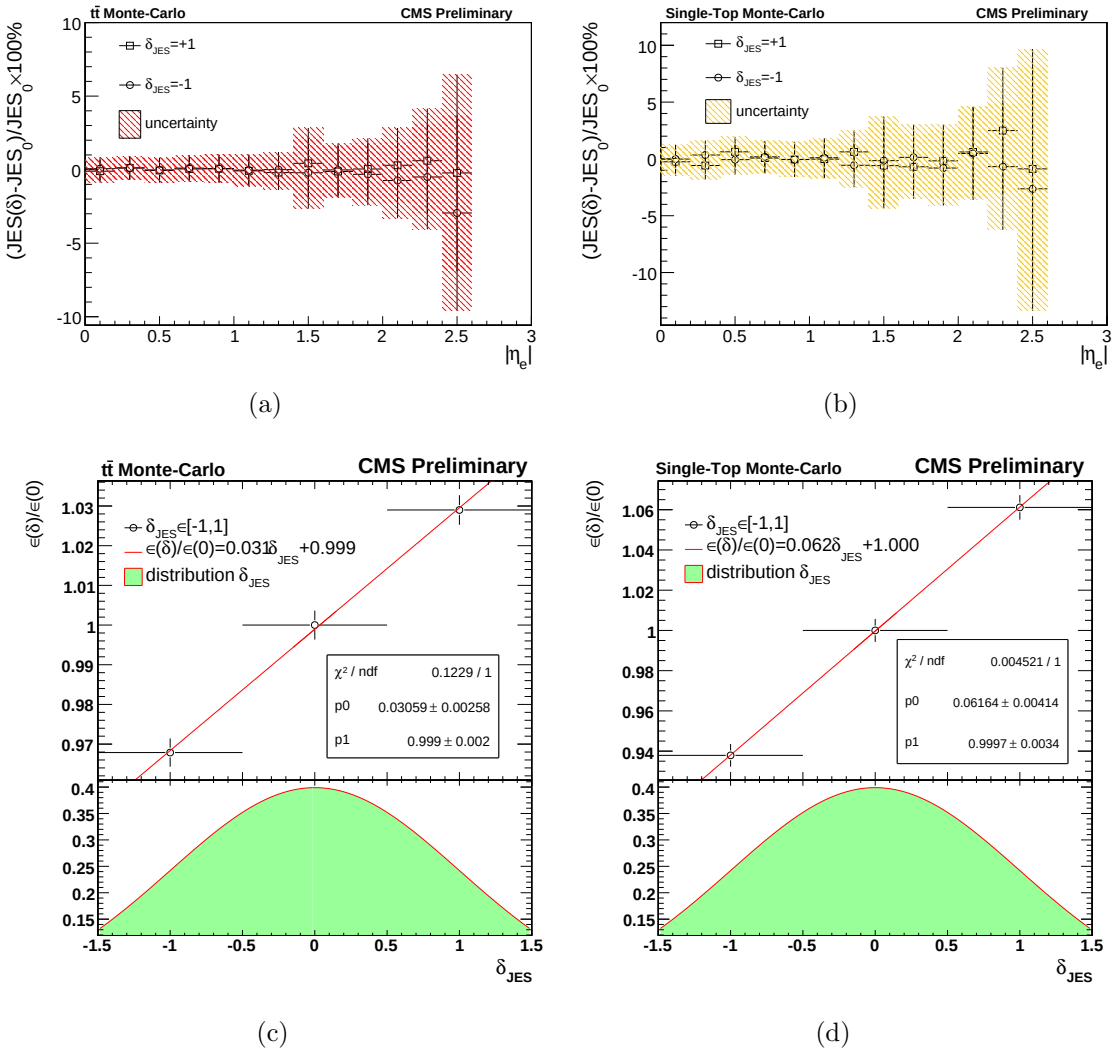

Figure 6.9: 6.9(a) and 6.9(b) show the relative shape uncertainty due to JES variations for $t\bar{t}$ and single top respectively respectively. 6.9(c) and 6.9(d) show the relative uncertainty on the efficiency due to JES variations for $t\bar{t}$ and single top MC predictions. In both cases the variation is parametrized using a linear fit.

where $\delta_P \in \{\log 0.5, 0, \log 2.0\}$. For Q^2 scale and the matching threshold, this variation has the physical meaning of varying parameters in the range of $[P_0/2, 2P_0]$.

The effect of varying Q^2 scale on $|\eta_e|$ is shown in Fig. 6.10(a). The relative differences for each bin with respect to the default scale Q_0^2 are marked as circles, and the uncertainty

due to statistical limitations as colored bands. The hypothesis that the variation of Q^2 scale has no impact on the shape of $|\eta_e|$ is consistent within statistical limitations. We therefore will not include any systematic uncertainty on the shape due to Q^2 scale variation. In Fig. 6.10(b), the effect of varying Q^2 scale on the $t\bar{t}$ selection efficiency is parametrized

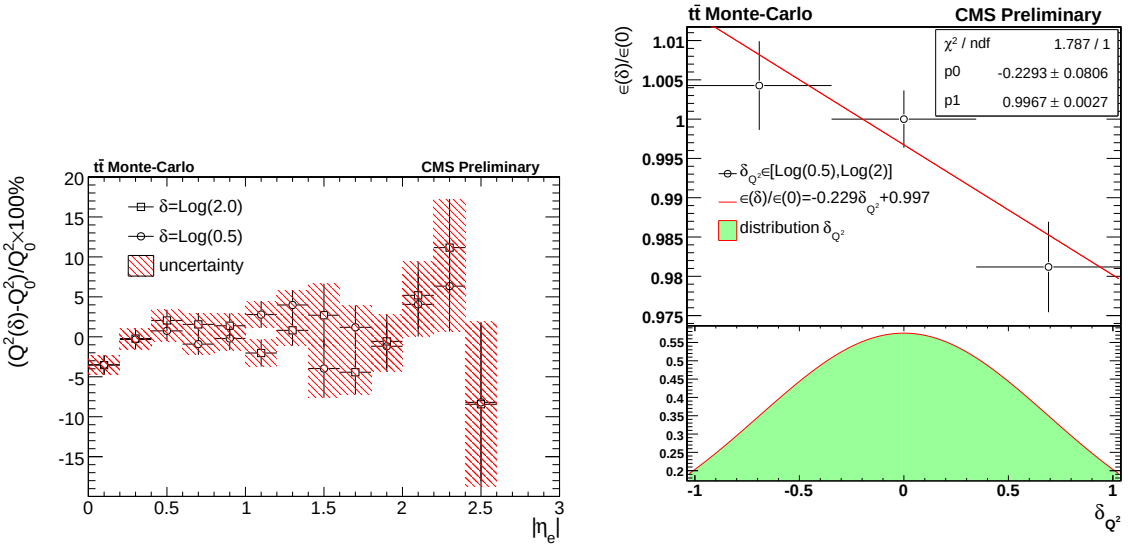

(a) (b)

Figure 6.10: 6.10(a) and 6.10(b) respectively show the relative uncertainty on the shape and the selection efficiency due to variations of Q^2 scale in the $t\bar{t}$ process.

using a linear fit, which is

$$\frac{\epsilon^{t\bar{t}}(\delta_{Q^2})}{\epsilon^{t\bar{t}}(0)} = -0.229\delta_{Q^2} + 0.997. \tag{6.10}$$

The situation is very similar for the uncertainty due to the matching threshold. The corresponding results are shown in Fig. 6.11(a) and 6.11(b), where the large uncertainty comes from the limited statistics in simulation. Again we assume it does not affect the shape of $|\eta_e|$. Within uncertainties, a linear fit is considered to be valid in parameterization of the effect on selection efficiency

$$\frac{\epsilon^{t\bar{t}}(\delta_{th})}{\epsilon^{t\bar{t}}(0)} = -0.013\delta_{th} + 1.007. \tag{6.11}$$

In pseudo experiments, uncertainties from Q^2 scale and matching threshold are taken

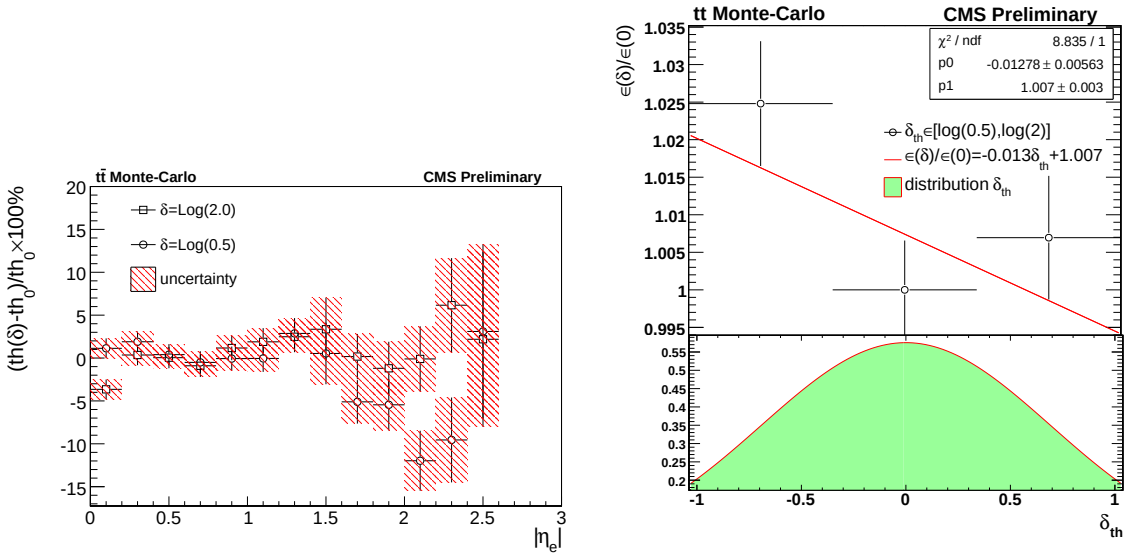

(a) (b)

Figure 6.11: 6.11(a) and 6.11(b) respectively show the relative uncertainty on the shape and one the selection efficiency due to variations of matching threshold in $t\bar{t}$ process.

into account as that from JES. A value of δ_{Q^2} (δ_{th}) is randomly picked using a normal distribution with mean zero and a width of $\log 2$. The corresponding efficiency is calculated using Eq. 6.10 (Eq. 6.11).

6.2.2.3 Luminosity and Single Top Cross Section

The luminosity enters at several places in the determination of the $t\bar{t}$ cross section. First, it appears in the function used to extract $t\bar{t}$ cross-section from the number of fitted events (see later in Eq. 6.14). Second, when constructing pseudo experiments, the actual number of expected signal ($t\bar{t}$ and single top) are constructed by the product of theoretical cross sections and the luminosity. We thus include the uncertainty arising from the error on the

measured luminosity and define an additional strength-parameter $\delta_{\mathcal{L}}$ in Eq. 6.12, where $\mathcal{L}_{\rm nom}$ is 857.7 pb^{-1}.

$$\mathcal{L}(\delta_{\mathcal{L}}) = \mathcal{L}_{\rm nom} \times (1 + \delta_{\mathcal{L}}). \tag{6.12}$$

The actual luminosity is then constructed in each pseudo experiment by picking numbers for $\delta_{\mathcal{L}}$ normally distributed around 0 with a width of 0.022, which corresponds to the 2.2% uncertainty of luminosity. The uncertainty on single top cross section is treated in the similar way. A sensitivity of $\sim 30\%$ from single top cross section is applied in this $t\bar{t}$ cross section measurement. The corresponding strength parameter δ_{st} is defined as

$$\sigma_{\rm Single-Top}(\delta_{st}) = \sigma_{\rm single-top} \times (1 + \delta_{st}), \tag{6.13}$$

and in each pseudo-experiment δ_{st} is randomly picked from a normal distribution with a mean of zero and a width of 0.3.

6.3 Neyman Construction

The Neyman construction is used for the determination of cross section and full uncertainty. This frequentist method constructs a confidence band for the measurement by performing pseudo-experiments, where the systematic uncertainties are treated as nuisance parameters. The procedure of construction is explained in this section.

The fitted $t\bar{t}$ cross section is computed from the fitted number of events $N_{\rm top}^{\rm fit}$ as following,

$$\sigma_{t\bar{t}}^{\rm fit} = \left(\frac{N_{\rm top}^{\rm fit}}{\epsilon_{t\bar{t}}\mathcal{L}} - \sigma_{\rm single-top} \frac{\epsilon_{\rm single-top}}{\epsilon_{t\bar{t}}} \right). \tag{6.14}$$

The actual $t\bar{t}$ cross section is derived from $\sigma_{t\bar{t}}^{\text{fit}}$ via a *frequentist* Neyman construction scheme [120][121]. In particular, we vary the following parameter

$$\beta_{t\bar{t}} = \frac{\sigma_{t\bar{t}}}{\sigma_{t\bar{t}}^{\text{nominal}}} \quad (\sigma_{t\bar{t}}^{\text{nominal}} = 157.5 \text{ pb}). \tag{6.15}$$

in the range $\beta_{t\bar{t}} \in [0.2, 2.]$ and construct an ensemble of 100K pseudo experiments for every $\beta_{t\bar{t}}$. In each pseudo experiment, we perform the same template fit on the pseudo data as we did for the real data, and derive the value of $\beta_{t\bar{t}}^{\text{fit}}$ from fitting, which is in return defined as

$$\beta_{t\bar{t}}^{\text{fit}} = \frac{\sigma_{t\bar{t}}^{\text{fit}}}{\sigma_{t\bar{t}}^{\text{nominal}}}. \tag{6.16}$$

This method produces a conditional probability density distribution $P(\beta_{t\bar{t}}^{\text{fit}}|\beta_{t\bar{t}})$ of variable $\beta_{t\bar{t}}^{\text{fit}}$ given each input value $\beta_{t\bar{t}}$. The central value $\beta_{t\bar{t}}^{\text{fit}}(0)$ is defined as the median value, i.e. the value of $\beta_{t\bar{t}}^{\text{fit}}$ for which the probability to get a smaller or larger value are equal. The upper and lower 1σ (2σ) bands are defined as values $\beta_{t\bar{t}}^{\text{fit}}(\pm n \cdot \sigma)$, with $n = 1, 2$, for which the following equations

$$1 - \frac{p_{n\cdot\sigma}}{2} = \int_{\beta_{t\bar{t}}^{\text{fit}}(+n\cdot\sigma)}^{\infty} P(\beta_{t\bar{t}}^{\text{fit}}|\beta_{t\bar{t}}) d\beta_{t\bar{t}}^{\text{fit}} = \int_{-\infty}^{\beta_{t\bar{t}}^{\text{fit}}(-n\cdot\sigma)} P(\beta_{t\bar{t}}^{\text{fit}}|\beta_{t\bar{t}}) d\beta_{t\bar{t}}^{\text{fit}}|\beta_{t\bar{t}}, \quad n = 1, 2, \tag{6.17}$$

hold with the 1 and 2 σ probabilities defined as

$$p_{1\sigma} = 68.2\% \quad p_{2\sigma} = 95.4\%. \tag{6.18}$$

From this procedure we can construct the inverted mapping of $\beta_{t\bar{t}}^{\text{fit}} \rightarrow \left(\beta_{t\bar{t}} + \Delta_{t\bar{t}}^{+} - \Delta_{t\bar{t}}^{-}\right)$ to finally obtain the cross section and the uncertainties as

$$\sigma_{t\bar{t}} = \sigma_{t\bar{t}}^{\text{nominal}} \times \left(\beta_{t\bar{t}} + \Delta_{t\bar{t}}^{+} - \Delta_{t\bar{t}}^{-}\right). \tag{6.19}$$

6.3.1 Construction of Pseudo Experiments

In pseudo experiments, distributions of $|\eta_e|$ are constructed by throwing Poisson numbers around the expected number of events in each bin. For the sake of simplicity, distributions

for each sub-process are constructed independently and then added together to form the final pseudo-observed $|\eta_e|$. The construction of the background distributions follows the procedures below:

- In each bin, a random number is generated based on a normal distribution with mean of the expected number of events and width correpsonding to the shape uncertainty.
- In each bin, a Poisson number is picked around mean constructed in the above step.

However, there is a large uncertainty ($\sim 15\%$ in each bin) on the QCD template due to the limit of statistics in applying the correction of relIso cut. The QCD component is therefore fixed in pseudo-experiments, helping to stabilize the pseudo-data. To deal with the uncertainty from QCD template, we vary $|\eta_e|$ distribution of our corrected QCD samples by its upper and lower errors and then normalize them. With these two QCD templates, the real data is fitted again. The resulting cross sections are then compared with the central value obtained by using the original QCD template. The difference is accounted for the systematic error from QCD template.

The construction of the signal pseudo-data is a little more involved since we have to take into account each source of systematic uncertainties and their impact on the expected number of signal in each bin, as well as on the efficiencies entering Eq. 6.14. We include all their effects by using strength-parameters for each source of systematic uncertainties defined in Section. 6.2.2. The variation of each strength-parameter δ_i affects either or possible both of the following:

- mean of the expected selection efficiency of $t\bar{t}$ process
- mean of the expected selection efficiency of single top process

These quantities have been parametrized as functions of strength-parameters δ_i, such that we can proceed as follows:

- For each systematic uncertainty source i, δ_i is supposed to be distributed normally around its mean expected value with a width corresponding to its uncertainty. When doing this, we restrict δ_i to physical values, i.e. the negative efficiency is not valid.
- According to the rules discussed in Section 6.2.2, the signal templates are not affected. Therefore, the expected shapes of $|\eta_e|$ for $t\bar{t}$ and single top processes are purely extracted from MC.
- The expected number of $t\bar{t}$ and single top events are computed by using

$$N^{\text{exp}}_{t\bar{t}(\text{single-top})} = \mathcal{L} \times \sigma_{t\bar{t}(\text{single-top})} \times \epsilon_{t\bar{t}(\text{single-top})}, \tag{6.20}$$

  where $\mathcal{L}$ and the efficiency ϵ are again computed from the given choice of strength parameters as defined in Section 6.2.2.
- In each bin, a Poisson number is throwed around mean constructed in the above steps.

The pseudo-data distributions are the simple sum of the distributions of all sub processes. These pseudo distributions are fitted using the maximum likelihood method as explained in the begining of Chapter 6, where the templates are the same as for fitting the real data. The fitted cross section $\sigma^{\text{fit}}_{t\bar{t}}$ is then calculated using Eq. 6.14.

6.4 Results

The binned likelihood fit is performed on the distribution of $|\eta_e|$ from data. Fig. 6.12(a) shows the signal templates obtained from MC and the data driven background templates as

described in Section 6.1. The number of events for each process extracted from the fit are shown in Tab. 6.6. In Fig. 6.12(b), the electron pesudorapidity of each process is derived from normalizing the templates by the number of events from the fit. The stacked distributions are compared with data, showing a good agreement.

Table 6.6: Expected number of events from MC (before fit) and number of events from the fit for each process.

Sample	Top ($t\bar{t}$ and single top)	W+jets	Drell-Yan	QCD	Total
MC estimation	6205.8 ± 15.3	10437 ± 72.9	2298.7 ± 13.1	3810.8 ± 525.3	22752.3 ± 530.7
Fit result	6532.2 ± 632.1	8741.5 ± 585.2	2872.6 ± 279.3	7384.9 ± 270.3	25531.2 ± 945.0

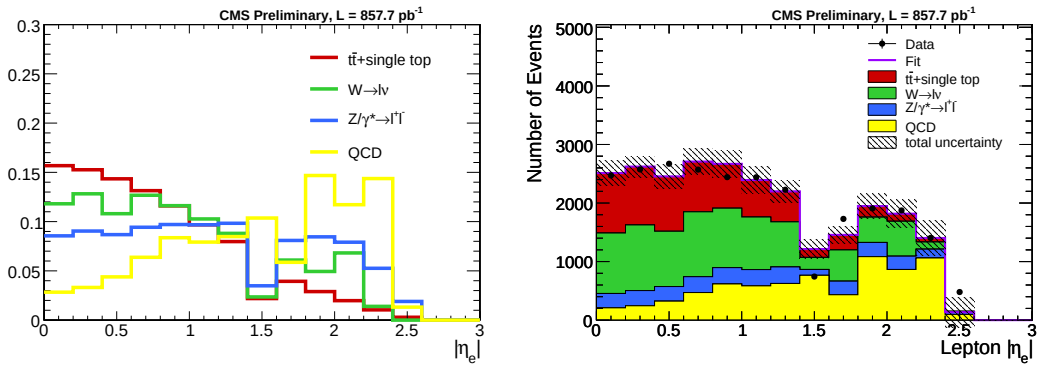

(a) (b)

Figure 6.12: 6.12(a) shows templates used in the binned likelihood fit. 6.12(a) shows the distribution of $|\eta_e|$ for each process which normalized to the number of events obtained in the fit, and the stacked histograms are compared with data.

Using the number of top events extracted from the fit in Eq. 6.14, the resulting $t\bar{t}$ production cross section is $\sigma_{t\bar{t}}^{\text{fit}} = 166.7 \pm 17.7$ pb, where the uncertainty is only due to fit statistics. Then an ensemble of 100K pseudo experiments are constructed for each value of $\beta_{t\bar{t}}$ in the set $\beta_{t\bar{t}} \in \{0.2, 0.5, 0.7, 0.9, 1.0, 1.2, 1.4, 1.8, 2.0\}$. The central value and $1/2\sigma$ error bands are built according to Neyman scheme as explained in Section 6.3. The results are summarized in Tab. 6.7. Fig. 6.4 shows the projection of $P(\beta_{t\bar{t}}^{\text{fit}}|\beta_{t\bar{t}})$ in

$\beta^{\text{fit}}_{t\bar{t}} - \beta_{t\bar{t}}$ plane, in which all lines (central values and the error bands) follow nicely a linear behavior. We therefore construct linear functional dependencies for $\beta_{t\bar{t}} + \Delta^{+}_{t\bar{t}} - \Delta^{-}_{t\bar{t}}$. The red horizontal line in Fig. 6.4 represents $\beta^{\text{fit}}_{t\bar{t}}$ extracted from fitting the real data distribution, which is $\beta^{\text{fit}}_{t\bar{t}} = 1.06$. It intersects with lines of central value and error bands, the $\beta_{t\bar{t}}$ components of the crossing points give the final results of $t\bar{t}$ cross section, which is $\sigma_{t\bar{t}} = 166.7^{+78.2\ (46.9\%)}_{-69.3\ (-41.6\%)}$ pb.

Table 6.7: Values of $\beta^{\text{fit}}_{t\bar{t}}$ for several input $\beta_{t\bar{t}}$ choices.

$\beta_{t\bar{t}}$	0.2	0.5	0.7	0.9	1.0	1.2	1.4	1.8	2.0
$\beta^{\text{fit}}_{t\bar{t}}(-2\sigma)$	-0.627	-0.345	-0.159	0.021	0.117	0.285	0.459	0.801	0.963
$\beta^{\text{fit}}_{t\bar{t}}(-1\sigma)$	-0.225	0.075	0.267	0.453	0.549	0.735	0.927	1.293	1.473
$\beta^{\text{fit}}_{t\bar{t}}(0)$	0.195	0.501	0.699	0.897	0.999	1.197	1.401	1.803	2.007
$\beta^{\text{fit}}_{t\bar{t}}(+\sigma)$	0.621	0.933	1.137	1.353	1.461	1.671	1.887	2.325	2.547
$\beta^{\text{fit}}_{t\bar{t}}(+2\sigma)$	1.047	1.377	1.593	1.809	1.929	2.151	2.391	2.859	3.087

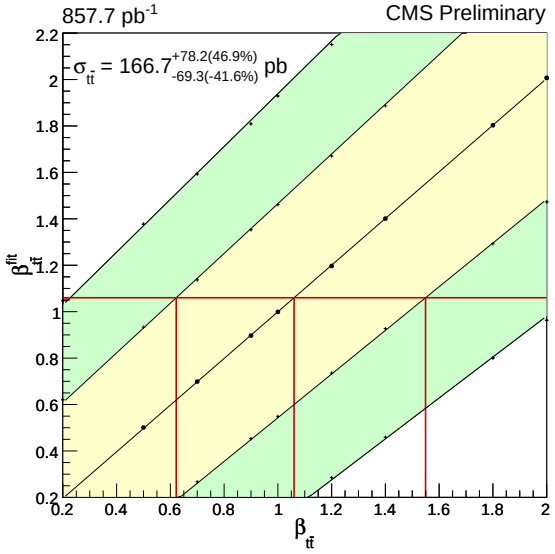

Figure 6.13: Functional dependence between $\beta^{\text{fit}}_{t\bar{t}}$ and $\beta_{t\bar{t}}$ with corresponding 1σ (yellow) and 2σ (green) uncertainty. The red lines correspond to the Neyman construction for the measured $t\bar{t}$ cross section.

The contribution from various individual sources of uncertainty can be identified by only including its contribution in pseudo experiments. The same Neyman scheme is then applied to extrapolate $\pm 1\sigma$ at $\beta_{t\bar{t}}^{\text{fit}} = 1.06$. The breakdown of the contribution for the individual uncertainties is shown in Tab. 6.8. The dominant sources are due to the statistical uncertainties of W+jets template and the Q^2 scaling uncertainty. The systematic errors from the background templates will be improved with increased statisics.

Table 6.8: Breakdown of systematic and statistical uncertainties in $t\bar{t}$ cross section measurement.

sources	$\delta(-1\sigma)$ pb (%)	$\beta_{t\bar{t}}^{\text{fit}}(0)$	$\delta(+1\sigma)$ pb (%)
W+jets Temp Stat.	-62.3 (-37.4%)	1.047	+70.8 (+42.5%)
DY Temp Stat.	-6.8 (-4.1%)	1.011	+7.0 (+4.2%)
QCD Temp Stat.	-23.3 (-14.0%)		+23.3 (+14.0%)
All BG stat.	-66.9 (-40.1%)	1.011	+74.9 (+44.9 %)
JES	-5.0 (-3.0%)	1.011	+5.0 (+3.0%)
Q^2 scale	-25.2 (-15.1%)	1.011	+25.7 (+15.4%)
matching threshold	-4.3 (-2.6%)	1.023	+4.7 (+2.8%)
luminosity	-7.0 (-4.2%)	1.011	+7.8 (+4.7%)
single top xsect.	-5.0 (-3.0%)	1.011	+5.0 (+3.0%)
stat.	-11.0 (-6.6%)	1.011	+11.7 (+7.0%)
syst. $\oplus$ stat.	-69.3 (-41.6%)	1.050	+78.2 (+46.9%)

6.5 Summary of $t\bar{t}$ Cross Section Measurement

We have extracted a $t\bar{t}$ production cross section of $166.7^{+78.2\ (46.9\%)}_{-69.3\ (-41.6\%)}$ pb in the e+jets channel using 857.7 pb^{-1} of CMS data. The result is one of the first top cross section measurements at $\sqrt{s} = 7$ TeV, and is in agreement with the perturbative QCD NLO

prediction, and included in Phys. Let. B 720 (2013) 83-104. Though suffering from a large uncertainty due to the limitation of statistics, this method explores a data driven method in extracting W+jets samples, which is used again in the differential cross section measurement. The similar binned template fit method is also utilized in extraction of QCD background in the differential cross section measurement.

CHAPTER 7

Top Pair Differential Cross Section Measurement

While in the previous measurement we use the template fit method, we now measure the normalized $t\bar{t}$ differential cross section with respect to the jet multiplicity using a simple counting method. In addition, the measurement is now performed using a b-tagging requirement described in Section 5.3.2. As shown later, it increases the ratio of signal to background considerably. We switch the methods and adding b-tagging in the signal selection for the following considerations

- The differential cross section measurement is a precision measurement. A clean signal sample is thus highly desirable.
- The data statistics increases to 5 fb^{-1}, which is large enough even after requiring at least two b jets in the final state.
- The same control region ($N_{\text{jets}} = 1||2$) as used in the cross section measurement does not exist. Instead we use the electron plus jets cross trigger, which requires at least three online reconstructed jets with $p_T > 30$ GeV and $|\eta| < 2.6$.

In this analysis, the inclusive cross section is first calculated from the number of selected events after background subtraction, and corrected for detector and reconstruction efficiencies, as

$$\sigma_{t\bar{t}} = \frac{N_{\text{data}} - N_{\text{BG}}}{A_{t\bar{t}}\mathcal{L}}. \tag{7.1}$$

The event yield N_{data} is the number of events in data passing the full event selection. The background events number N_{BG} is estimated either directly from MC simulation or from

data driven methods for different processes. $A_{t\bar{t}}$ is the acceptance from $t\bar{t}$ MC where the correction from PU, b-tagging, electron ID/relIso and trigger efficiency are considered. $\mathcal{L}$ is the integrated luminosity corresponding to 5 pb^{-1}.

The normalized differential cross section $\frac{1}{\sigma}\frac{d\sigma}{dN_{\text{jets}}}$ is measured as a function of number of jets. For each $N_{\text{jets}} \in \{3, 4, 5, 6, 7 \geq 8\}$, the measurement is performed separately as following

$$\frac{1}{\sigma_{t\bar{t}}}\frac{d\sigma_{t\bar{t}}^{\text{measured}}}{dN_{\text{jets}}} = \frac{1}{\sigma_{t\bar{t}}} \cdot \frac{N_{\text{data}}^{i} - N_{\text{BG}}^{i}}{\Delta_{X}^{i}\epsilon^{i}\mathcal{L}}. \tag{7.2}$$

In each bin i, the number of signal events after background subtraction ($N_{\text{data}}^{i} - N_{\text{BG}}^{i}$) is scaled to the integrated luminosity $\mathcal{L}$. Δ_{X}^{i} is bin width, which is 1. $\sigma_{t\bar{t}}$ is the measured total cross sections defined in Eq. 7.1. In general, the bin-wise efficiency $\epsilon_{\text{uncor}}^{i}$ is defined as $\frac{N_{\text{reco}}^{i}}{N_{\text{reco-total}}^{i}}$, where N_{rec}^{i} ($N_{\text{reco-total}}^{i}$) is the number of events passing (without passing) the full selection while containing i reconstructed jets. However, for the differential measurements, events that are actually produced in one bin might be measured in another bin due to the effects of the finite experimental resolution. Therefore, a modified efficiency ϵ^{i} is introduced to correct the bin-to-bin migration in the following way

$$\epsilon^{i} = \epsilon_{\text{uncor}}^{i}\frac{N_{\text{reco-total}}^{i}}{N_{\text{gen-total}}^{i}} = \frac{N_{\text{reco}}^{i}}{N_{\text{reco-total}}^{i}} \times \frac{N_{\text{reco-total}}^{i}}{N_{\text{gen-total}}^{i}} = \frac{N_{\text{rec}}^{i}}{N_{\text{gen-total}}^{i}}, \tag{7.3}$$

where $N_{\text{gen-total}}^{i}$ is the total number of events with i generated jets with $p_T > 35$ GeV and $|\eta| < 2.4$, such requirement on p_T and η are the same as the reconstructed jets. In Eq. 7.3, $\frac{N_{\text{reco-total}}^{i}}{N_{\text{gen-total}}^{i}}$ used to correct $\epsilon_{\text{uncor}}^{i}$ is in a range of $0.92 - 1.06$. Fig. 7.1 shows the 2D distribution of $N_{\text{gen-total}}^{i}$ v.s. $N_{\text{reco-total}}^{i}$ of $t\bar{t}$ events normalized to 5 pb^{-1}, indicating that most of events generated with i jets contain i reconstructed jets ($i, j \in 3, 4, 5, 6, 7, \geq 8$).

In this chapter, data driven methods used to model QCD and W+jets backgrounds are detailed in Section 7.1, and MC are used to estimate the smaller backgrounds i.e. single top,

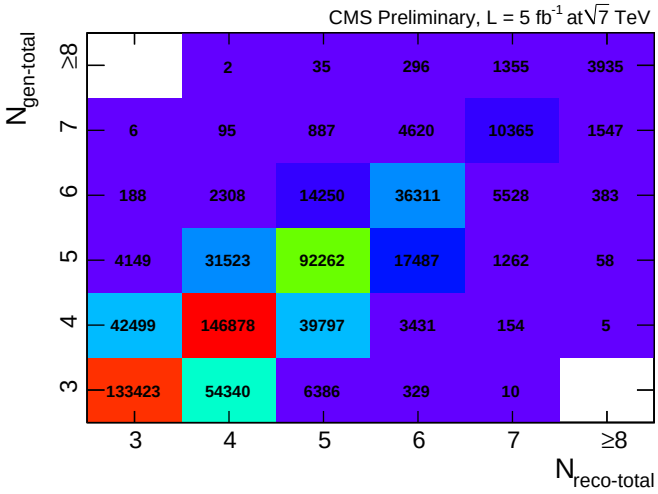

Figure 7.1: The plot depicts the number of $t\bar{t}$ MC events generated with i jets while containing reconstructed j jets, $i, j \in 3, 4, 5, 6, 7, \geq 8$. Events are normalized to 5 pb^{-1}.

Z+jets and electroweak processes. The systematic uncertainties are discussed in Section 7.2.

The final result, which is compared to theory predictions, is shown in Section 7.3.

7.1 Backgrounds Estimation

7.1.1 QCD Background

Since we now apply b-tagging, the QCD background is greatly reduced by $\sim 97\%$ as shown in Tab. 5.9. The remaining contribution is estimated from data, as MC is again not reliable in modeling this process. As before we use the electron isolation to select a clean QCD sample and use it to predict the QCD background in the signal region. Fig.7.2(a) shows that QCD process dominates when selecting for poor isolation electron, i.e. higher values of relIso. Moreover, QCD events have fewer b jets in the final state, such that an inversion of the b-tagging requirement further purifies a QCD control sample.

The sidebands in both electron relative isolation (relIso) and the number of tagged jets ($N_{\text{jets}}^{\text{tag}}$) are used to extrapolate QCD events into the signal region. This method is called "ABCD" method and often used in the hadron collision measurements. The data sample is divided into four separate regions as follows, where region B is the signal region.

- A: $N_{\text{jets}}^{\text{tag}} \leq 1$, relIso$<$ 0.1 (sideband)
- B: $N_{\text{jets}}^{\text{tag}} \geq 2$, relIso$<$ 0.1 (signal)
- C: $N_{\text{jets}}^{\text{tag}} \leq 1$, 0.3 $<$relIso$<$ 1.0 (sideband)
- D: $N_{\text{jets}}^{\text{tag}} \geq 2$, 0.3 $<$relIso$<$ 1.0 (sideband)

Fig. 7.2(b) shows the 2D distribution of data in relIso-$N_{\text{jets}}^{\text{tag}}$ plane with four marked regions. The main assumption of this ABCD method is to consider that the isolation of electrons and $N_{\text{jets}}^{\text{tag}}$ are weakly correlated for QCD events, such that the ratio of QCD events between region C and A is equal to that between region D and B. To extract the

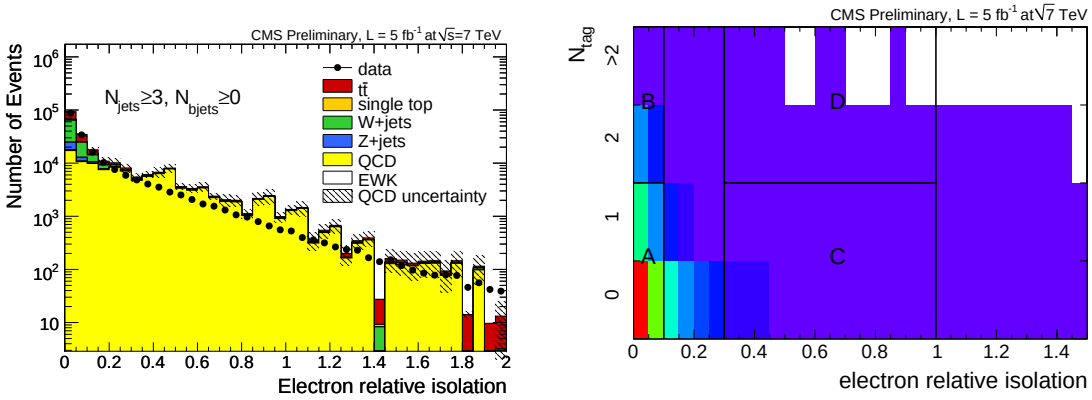

(a) (b)

Figure 7.2: 7.2(a) shows electron relIso distribution of data and MC for events with $N_{\text{jets}} \geq 3$, 7.2(b) shows electron relIso v.s. $N_{\text{jets}}^{\text{tag}}$ for data. Events pass the offline event selection without b-tagging and relIso cut.

ratio between region C and A (β_{QCD}), a binned maximum fit is applied on $\not\!\!E_{\text{T}}$ distribution of data in the isolated and lower tagged region A. In the fit, a QCD samples is derived from region C in data, non-QCD samples are from region A using simulation. The logarithm of the likelihood (LL) can be constructed as

$$LL(\{\mu_i,\ n_i\}) = -2\ \log\left(\prod_i^{\text{nbins}} \frac{\mu_i^{n_i}\cdot e^{-\mu_i}}{n_i!}\right) = -2\sum_i^{\text{nbins}} \log\left(\frac{\mu_i^{n_i}\cdot e^{-\mu_i}}{n_i!}\right), \tag{7.4}$$

where μ_i (n_i) are the expected (observed) number of events in each bin i of $\not\!\!E_{\text{T}}$. We model the expected $\not\!\!E_{\text{T}}$ distribution $\{\mu_i\}$ by

$$\mu_i = \sum_j \beta_j \theta_j^i, \tag{7.5}$$

where θ_j represents the $\not\!\!E_{\text{T}}$ distribution in i^{th} bin, and j is process dependent, i.e. $j = t\bar{t}$, W+jets, Z+jets, single top, QCD and EWK. The fit parameters β^j are ratios of measured and predicted numbers of events. In the likelihood fit we assign ratios of all non-QCD processes with 10% Gaussian constraints. Fig. 7.3(a) shows the $\not\!\!E_{\text{T}}$ shapes of the different samples taken from region C ($N_{\text{jets}}^{\text{tag}} \leq 1$, 0.3 <relIso< 1.0). The fitting results are shown in Fig. 7.3(b) and are summarized in Table 7.1.

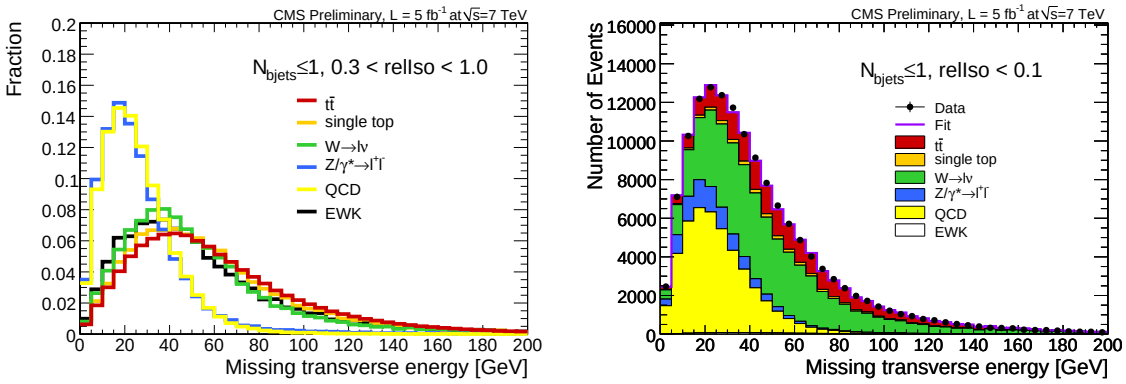

(a) (b)

Figure 7.3: 7.3(a) shows the sample shapes used in the binned likelihood fit, and 7.3(b) shows the results of fitting the data in the sideband region A

Table 7.1: The ratios of predicted and measured numbers of events of each processes from fitting the data in region A.

	$t\bar{t}$	single top	W+jets	Z+jets	EWK	QCD
β	0.94 ± 0.04	1.00 ± 0.10	1.01 ± 0.02	1.00 ± 0.02	0.99 ± 0.10	0.63 ± 0.01

The contribution of QCD in the signal region is then obtained by multiplying the number of events in region D by the ratio β_{QCD} in each jet multiplicity bin. Notice that the contribution from other non-QCD processes are subtracted from total events in region D using MC. In $N_{\text{jets}} = 7$ and ≥ 8, MC estimates more events from processes other than QCD, since QCD is completely negligible in this sample. In that case, zero QCD events are assigned in the samples with $N_{\text{jets}} = 7$ and ≥ 8. The uncertainty is the absolute difference of event numbers between the MC events from other processes and the data. The QCD events in the signal region are summarized in Tab. 7.2. The systematic uncertainty is discussed in Section 7.2.3.

Table 7.2: The table summarizes the QCD events in signal region (region B).

N_{jets}	3	4	5	6	7	≥ 8
QCD	521.4 ± 19.2	124.9 ± 9.0	13.6 ± 2.9	0.18 ± 0.34	0.0 ± 3.0	0.0 ± 2.0

QCD Cross Check: A binned template fit method can be used as a cross check for the QCD estimation. The template is the shape of $\not{E}_{\mathrm{T}}$ distribution, i.e. the normalization of the shape template is one. For QCD process, the template is taken in the region of $N_{\mathrm{jets}} = 3$ and relIso > 0.2. The templates of non-QCD events are obtained from MC with all the events passing the offline event selections without b-tagging. The same method, which is discussed in the beginning of Chapter 6, is applied on data in the signal region. The free parameters are numbers of events for each contributing process.

In the fit, we assign Gaussian constraints on both W+jets and Z+jets (single top and EWK) events within 100% (50%) of their predicted number. In addition, the fit is performed in jet multiplicity up to $N_{\mathrm{jets}} \geq 7$ since it does not converge in $N_{\mathrm{jets}} \geq 8$ due to limited statistics. Fig. 7.4(a)−7.4(e) show the fitting results in different jet multiplicity, where $\not{E}_{\mathrm{T}}$ distributions of each process are obtained by normalizing the shape templates with the event numbers from fitting, and the stacked histograms are compared with data. Tab. 7.3 summarizes the event numbers from fitting and compares them with MC predictions, there is a good agreement in QCD estimation between using ABCD method and the binned template fit method.

Table 7.3: Table shows the binned likelihood fitting results in the signal region, and compared to MC expectation for $N_{\mathrm{jets}} = 3, 4, 5, 6, \geq 7$. Errors from fitting are quoted.

	$t\bar{t}$	single top	W+jets	Z+jets	QCD	EWK
Fit $N_{\mathrm{jets}} = 3$	5226.4 ± 383.1	1037 ± 314	1071.5 ± 335.5	108.6 ± 122.2	485.4 ± 168.4	20.3 ± 10.1
MC $N_{\mathrm{jets}} = 3$	6737 ± 9.8	599 ± 6.4	463.4 ± 30.2	98.4 ± 6.5	904.5 ± 449.3	18.7 ± 0.3
Fit $N_{\mathrm{jets}} = 4$	4925.4 ± 175.4	289.3 ± 125.9	184.8 ± 114.7	37.7 ± 48.3	199.5 ± 80.7	5.9 ± 3
MC $N_{\mathrm{jets}} = 4$	5272.5 ± 8.7	236.8 ± 4.2	135.3 ± 16.3	33.2 ± 3.8	0.0 ± 0.0	5.5 ± 0.4
Fit $N_{\mathrm{jets}} = 5$	1886.6 ± 66.9	65.5 ± 33.5	23.2 ± 29.4	7.8 ± 7.5	13.7 ± 32.7	1.5 ± 0.7
MC $N_{\mathrm{jets}} = 5$	1968.2 ± 5.3	63.6 ± 2.3	41.4 ± 9.0	6.4 ± 1.7	0 ± 0	1.0 ± 0.2
Fit $N_{\mathrm{jets}} = 6$	512.9 ± 25.1	14.1 ± 7.1	6.3 ± 6.8	2.7 ± 3.3	0 ± 7.8	0.4 ± 0.2
MC $N_{\mathrm{jets}} = 6$	565.1 ± 2.8	15.1 ± 1.2	8.7 ± 4.1	2.1 ± 0.9	0 ± 0	0.2 ± 0.1
Fit $N_{\mathrm{jets}} \geq 7$	144.4 ± 14	3.2 ± 1.6	0.0 ± 4.1	0.8 ± 1.2	0 ± 2.1	0.1 ± 0
MC $N_{\mathrm{jets}} \geq 7$	177.8 ± 1.6	3.2 ± 0.5	0.0 ± 0.0	0.3 ± 0.4	0 ± 0	0.1 ± 0.1

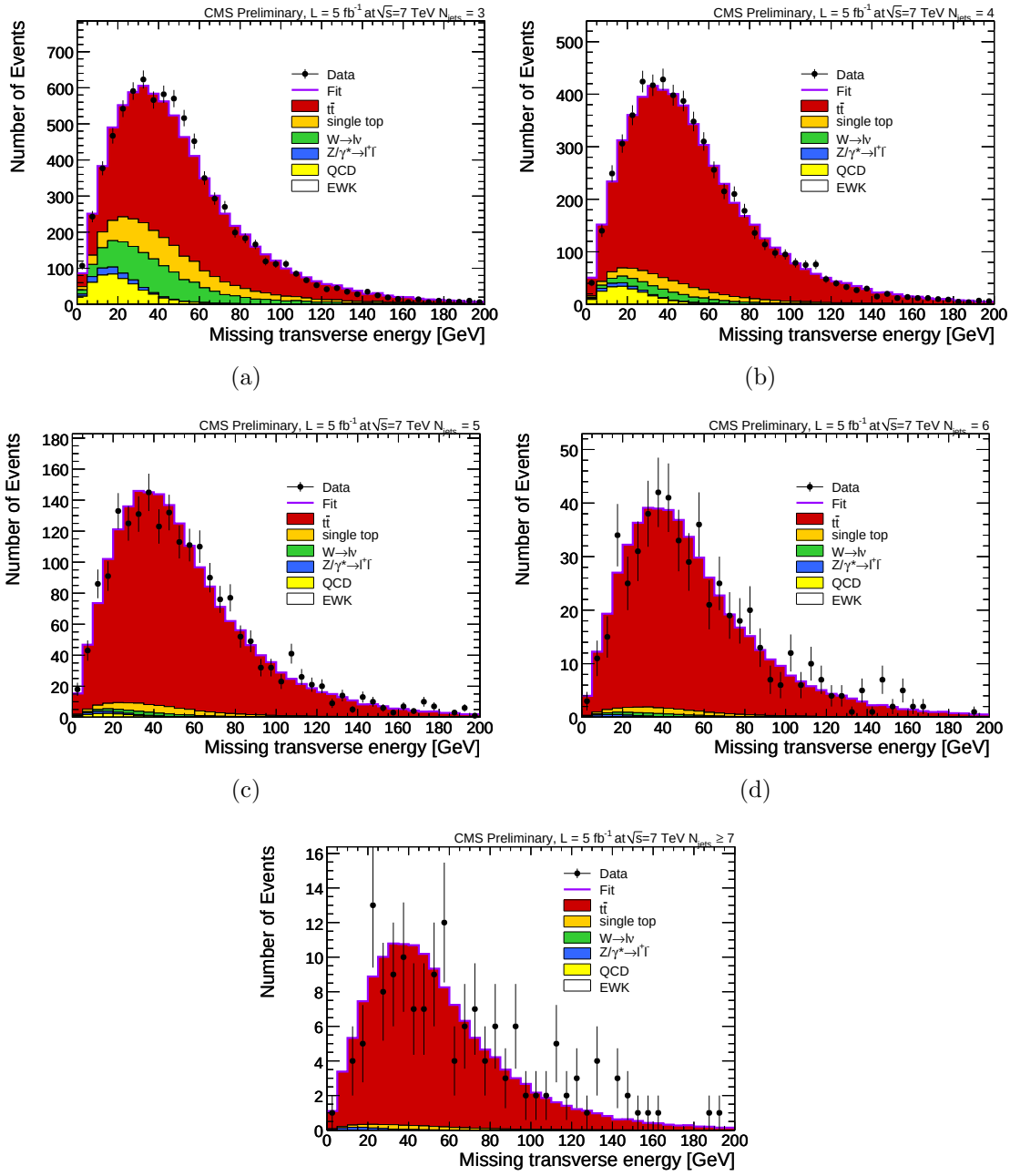

Figure 7.4: 7.4(a)–7.4(e) show results of binned template fit to data in $N_{\text{jets}} = 3, 4, 5, 6, \geq 7$. The QCD template is from control region C. Templates of other processes are from MC in the signal region.

7.1.2 W+jets Background

In the W+jets background estimation, the jet multiplicity shape is assumed to be well described by MC simulation. The overall normalization is derived from data including the estimation of pre-tagged W+jets events, flavor fractions and tagging efficiency. The charge asymmetry property is used again to estimate the total number of pre-tagged W+jets events. The simulated heavy flavor fractions are corrected by a factor k_i ($i = Wb\bar{b}$, $Wc\bar{c}$, Wc and W+light flavor) since MC cannot model these fractions correctly. This has been observed in both CMS and CDF experiments [122][123], which is bigger than the MC simulation. The b-tagging efficiency is taken from MC, and corrected by a scale factor derived from data, as described in Section 5.3.3.3. The overall normalization, which is the total number of tagged W+jets events is estimated by

$$N_{\mathrm{w+jets}}^{\mathrm{tagged}} = N_{\mathrm{W+jets}}^{\mathrm{pre-tagged}}(F_{\mathrm{W}b\bar{b}}\epsilon_b^{\mathrm{W}b\bar{b}} + F_{\mathrm{W}c\bar{c}}\epsilon_b^{\mathrm{W}c\bar{c}} + F_{\mathrm{W}c}\epsilon_b^{\mathrm{W}c} + F_{\mathrm{w+l}}\epsilon_b^{\mathrm{w+l}}) \tag{7.6}$$

where $N_{\mathrm{W+jets}}^{\mathrm{pre-tagged}}$ is the total number of pre-tagged W+jets events, F_i and ϵ^i ($i = Wb\bar{b}$, $Wc\bar{c}$, Wc, W + light) are the corrected flavor fractions and event tagging efficiencies respectively.

7.1.2.1 Pre-tagged W+jets from Charge Asymmetry Property

The number of pre-tagged W+jets events $N_{\mathrm{W+jets}}^{\mathrm{pre-tag}}$ is determined using the fact that the ratio of the cross sections $\frac{\mathrm{pp}\to\mathrm{W}^+}{\mathrm{pp}\to\mathrm{W}^-}$ is bigger than unity. This is described in Section 6.1.1. Processes other than W+jets give equal contribution of positively and negatively charged leptons. After subtracting the jet multiplicity distribution of electron from that of position, a pure W+jets sample is obtained from data, as shown in Fig. 7.5. Tab. 7.4 summarizes

the number of events after the subtraction in each jet bin. Therefore we can use the following equation to give the number of the pre-tagged W+jets events

$$N_{\mathrm{W+jets}}^{\mathrm{pre-tag}} = N_{W^+} + N_{W^-} = \frac{N_{W^+} - N_{W^-}}{A_w}, \tag{7.7}$$

where $N_{W^+}(N_{W^-})$ are the total numbers of events in data passing event selection cuts except b-tagging with positively (negatively) charged electrons. A_w is charge asymmetry factor, defined as $A_W \equiv \dfrac{\sigma(W^+) - \sigma(W^-)}{\sigma(W^+) + \sigma(W^-)}$. $A_w = 0.162 \pm 0.006$ is taken from MC.

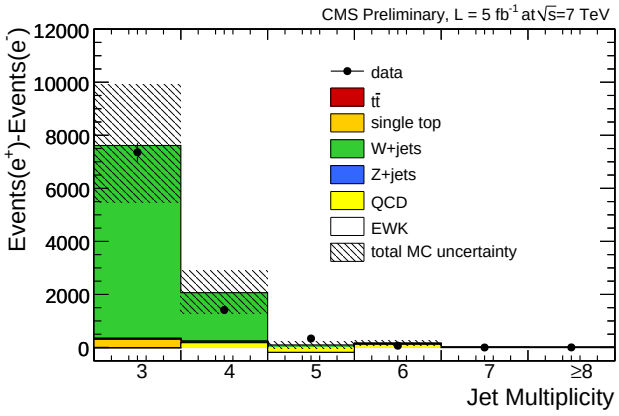

Figure 7.5: The plot shows the charge-subtracted electron jet multiplicity distribution. Events pass the offline event selection before b-tagging, MC are normalized to 5.0 fb^{-1}.

Table 7.4: The charge asymmetry distributions v.s. jet number, MC are normalized to 5.0 fb^{-1}.

	data	$t\bar{t}$	single top	W+jets	Z+jets	QCD	EWK
3	7359 ± 342.9	1.4 ± 17.6	316.7 ± 14.3	7271 ± 307.6	34.6 ± 59.7	-9 ± 2196.2	87.5 ± 6.7
4	1414 ± 176.1	-3.8 ± 13.7	52.6 ± 7.9	1883.1 ± 131.5	-46 ± 25.7	179.8 ± 794.1	17.4 ± 2.8
5	338 ± 87.2	0.6 ± 8	10.6 ± 3.8	266.8 ± 49.5	-0.6 ± 10.2	-182.2 ± 116.4	2.9 ± 1
6	66 ± 39.7	2.9 ± 4.1	1.3 ± 1.7	49.7 ± 18.2	-0.9 ± 3.8	121 ± 103.8	0.2 ± 0.4
7	-1 ± 17.7	2.9 ± 2.0	0.0 ± 0.7	8.1 ± 4.0	-0.9 ± 1.5	0.0 ± 0.0	-0.1 ± 0.2
≥ 8	2.0 ± 8.4	1.2 ± 1.0	-0.2 ± 0.3	2.9 ± 2.4	0.1 ± 0.7	0.0 ± 0.0	0.0 ± 0.1

After scaling $N_{W^+} - N_{W^-}$ by A_w, the number of pre-tagged W+jets is shown in Table 7.5 and compared with MC expectation. The systematic error quoted here is from the A_w measurement.

Table 7.5: The table shows the $N_{W^+} - N_{W^-}$ and $N_{W^+} + N_{W^-}$ in $N_{\text{jets}} \geq 3$, compared with MC.

$N_{\text{jets}} \geq 3$	$N_{W^+} - N_{W^-}$	$N_{W^+} + N_{W^-}$
Data	9177.0 ± 397.6	56588.3 ± 2131.6
W+jets MC	9481.6 ± 338.7	58503.8 ± 338.8

7.1.2.2 Heavy Flavor Correction and Tagging Efficiency

The MC cannot correctly predict the heavy flavor fraction of W+jets events, and so the CMS Top Physics Analysis Group has decided to apply a scale factor $k_{Wb\bar{b}} = 2 \pm 1$ to the MC estimation, which provides a conservative estimation based on the available results [123]. For the Wc ($Wc\bar{c}$) component, there is no such re-weighting but $K_{Wc(Wc\bar{c})} = 1^{+1}_{-0.5}$ is introduced for systematic studies. Then the corrected flavor fraction F_i is defined as Eq. 7.8 and summarized in Tab. 7.6.

$$F_i = \frac{k_i f_i}{\sum_i^{\text{all flavors}} k_i f_i} \tag{7.8}$$

Table 7.6: The fraction of each sub-sample f_i before and after correction (F_i) for increased heavy flavor by a factor k_i. The systematic uncertainties quoted here are from F_i.

i	f_i	k_i	F_i
$Wb\bar{b}$	0.025 ± 0.001	2 ± 1	$0.049 \pm 0.002(\text{stat.}) \pm 0.023(\text{syst.})$
$Wc\bar{c}$	0.036 ± 0.001	$1^{+1}_{-0.5}$	$0.036 \pm 0.001(\text{stat.})^{+0.034}_{-0.017}(\text{syst.})$
Wc	0.153 ± 0.002	$1^{+1}_{-0.5}$	$0.149 \pm 0.002(\text{stat.})^{+0.127}_{-0.063}(\text{syst.})$
W+light	0.785 ± 0.003	1	$0.766 \pm 0.001(\text{stat.})$

The event tagging efficiencies of $Wb\bar{b}$, $Wc\bar{c}$, Wc and W+light are obtained from MC which are corrected by the scale factors in Section 5.3.3.3. Table 7.7 shows the event tagging efficiencies, only statistic uncertainties are quoted. The uncertainty from scale factors is considered as systematic uncertainty of b-tagging. Using Eq. 7.6, the numbers of

tagged $Wb\bar{b}$, $Wc\bar{c}$, Wc and W+light flavor are shown in Tab. 7.8. Adding them together gives the total number of tagged W+jets events, see the last column of Tab. 7.8.

Table 7.7: The event tagging efficiency of W+heavy (light) flavor events measured with data-driven scale factors applied to the W+jets jet-level efficiencies. Only statistic uncertainty are quoted.

	$Wb\bar{b}$	$Wc\bar{c}$	Wc	W+light
ϵ_{eff}	0.228 ± 0.019	0.035 ± 0.006	0.010 ± 0.001	0.003 ± 0.0003

Table 7.8: Number of tagged W+heavy(light) flavor events, compared with MC expectation. The systematic uncertainties are from flavor fraction corrector k_i.

$N^{\text{tag}}_{\text{W+jets}}$	$Wb\bar{b}$	$Wc\bar{c}$	Wc	W+light	Total
Data	$632.2 \pm 63.3 \pm 269.7$	$71.3 \pm 12.7^{+67.3}_{-33.7}$	$84.3 \pm 9.1^{71.9}_{-35.7}$	130.0 ± 13.9	$917.7 \pm 66.7^{+312.7}_{-300.8}$
MC	334.8 ± 25.6	73.9 ± 12.0	86.8 ± 13.1	153.3 ± 17.3	648.8 ± 35.7

7.1.2.3 W+jets Estimation Summary

To extract the number of W+jets events in each jet bin, we multiply the total number of tagged W+jets events by the shape of jet multiplicity, as shown in Tab. 7.9.

Table 7.9: Numbers of W+jets in $N_{\text{jets}} = 3,\ 4,\ 5,\ 6,\ 7,\ \geq 8$, compared with MC expectation. The systematic uncertainties are from flavor fraction corrector k_i.

N_{jets}	jet multiplicity shape	Data	MC
3	0.714 ± 0.046	$655.4 \pm 63.6(\text{stat.})^{+223.2}_{-214.8}(\text{syst.})$	463.4 ± 30.2
4	0.209 ± 0.025	$191.8 \pm 26.8(\text{stat.})^{+65.3}_{-62.9}(\text{syst.})$	135.3 ± 16.3
5	0.063 ± 0.013	$57.8 \pm 12.6(\text{stat.})^{+19.7}_{-18.9}(\text{syst.})$	41.4 ± 9.0
6	0.013 ± 0.006	$11.9 \pm 5.6(\text{stat.})^{+4.1}_{-3.9}(\text{syst.})$	8.7 ± 4.1
7	0 ± 0	0 ± 0	0 ± 0
≥ 8	0 ± 0	0 ± 0	0 ± 0

7.2 Systematic Uncertainties

7.2.1 Jet Energy Scale

As described in Section 6.2.2.1, the uncertainty on JES calibration is one of the dominant uncertainties when selecting events with many jets. JES has potentially an impact on the shapes of $\not\!\!E_{\mathrm{T}}$ templates for all processes in QCD estimation, the flavor fractions and event tagging efficiency of W+jets events. To determine these effects, the jet four momenta are shifted by its upper and lower uncertainty which is provided for the standard η and p_T dependent jet energy corrections. We then use MC samples with these JES variations to repeat the study described in Section 7.1.1 and 7.1.2. Tab. 7.10 shows the effect of JES variations on QCD, W+jets, Z+jets, single top and EWK estimations. Tab. 7.11 and 7.12 show the effect of JES variations on ϵ_i defined in Eq. 7.3 and measured total cross section $\sigma_{t\bar{t}}$ respectively.

7.2.2 Factorization Scale and Matching Threshold

For $t\bar{t}$ and W+jets processes, Q^2 scale and matching threshold systematics have different effects on measuring the normalized differential cross section:

- $t\bar{t}$ Q^2 scale and matching threshold: N_i^{QCD}, ϵ_i and $\sigma_{t\bar{t}}^{\mathrm{measure}}$ which is the measured total cross section used for normalization.
- W+jets Q^2 scale and matching threshold: N_i^{QCD}, $N_i^{\mathrm{w+jets}}$ and $\sigma_{t\bar{t}}^{\mathrm{measure}}$

Therefore, they are treated independently and then added in quadrature. To estimate the systematic uncertainties due to the choice of Q^2scale and matching threshold, we investigate

Table 7.10: The table summarizes effect on the QCD, W+jets, $Z + jets$, single top, and EWK estimations due to JES variations.

		$N_{\text{jets}} = 3$	$N_{\text{jets}} = 4$	$N_{\text{jets}} = 5$	$N_{\text{jets}} = 6$	$N_{\text{jets}} = 7$	$N_{\text{jets}} \geq 8$
QCD	central	521.4 ± 19.2	124.9 ± 9.0	13.6 ± 2.9	0.18 ± 0.34	0.0 ± 3.0	0.0 ± 2.0
	JES up	526.3 ± 19.4	125.7 ± 9.1	8.6 ± 2.4	0.0 ± 2.1	0.0 ± 4.1	0.0 ± 3.0
	JES down	546.2 ± 20.0	144.4 ± 10.0	19.5 ± 3.6	3.9 ± 1.6	0.0 ± 4.0	0.0 ± 2.0
W+jets	central	655.4 ± 63.6	191.8 ± 26.8	57.8 ± 12.6	11.9 ± 5.6	0.0 ± 0.0	0.0 ± 0.0
	JES up	565.2 ± 132.5	147.8 ± 52.0	53.6 ± 29.1	0.0 ± 0.0	0.0 ± 0.0	0.0 ± 0.0
	JES down	622.4 ± 154.2	162.2 ± 60.7	43.0 ± 28.4	0.0 ± 0.0	0.0 ± 0.0	0.0 ± 0.0
Single top	central	599 ± 6.4	236.8 ± 4.2	63.6 ± 2.3	15.1 ± 1.2	3.0 ± 0.5	0.2 ± 0.1
	JES up	587.1 ± 11.1	251.9 ± 6.3	67 ± 3.1	15.8 ± 1.4	2.8 ± 0.3	0.6 ± 0.4
	JES down	547.1 ± 10.6	214.9 ± 5.8	55.8 ± 2.8	14.3 ± 1.3	2.1 ± 0.3	0.2 ± 0.2
Z+jets	central	98.4 ± 6.5	33.2 ± 3.8	6.4 ± 1.7	2.1 ± 0.9	0.3 ± 0.4	0.0 ± 0.0
	JES up	94.7 ± 12.5	22.4 ± 6.1	2.1 ± 1.9	1.5 ± 1.6	0.0 ± 0.0	0.0 ± 0.0
	JES down	80.7 ± 11.6	21.6 ± 6.0	1.2 ± 1.4	1.2 ± 1.4	0.0 ± 0.0	0.0 ± 0.0
EWK	central	18.7 ± 0.8	5.5 ± 0.2	1.0 ± 0.2	0.2 ± 0.1	0.1 ± 0.1	0.0 ± 0.0
	JES up	20.0 ± 1.8	5.4 ± 1.1	1.2 ± 0.5	0.1 ± 0.1	0.0 ± 0.0	0.0 ± 0.0
	JES down	16.2 ± 1.7	5.5 ± 1.1	1.1 ± 0.5	0.1 ± 0.1	0.0 ± 0.0	0.0 ± 0.0

Table 7.11: The table summarizes JES effect on the ϵ_i from $t\bar{t}$ MC, defined in Eq. 7.3

ϵ_i	$N_{\text{jets}} = 3$	$N_{\text{jets}} = 4$	$N_{\text{jets}} = 5$	$N_{\text{jets}} = 6$	$N_{\text{jets}} = 7$	$N_{\text{jets}} \geq 8$
central	0.0298	0.0222	0.0134	0.0096	0.0080	0.0067
JES up	0.0297	0.0232	0.0144	0.0104	0.0086	0.0070
JES down	0.0299	0.0211	0.0124	0.0086	0.0076	0.0057

their effects on $\not\!\!E_{\text{T}}$ templates of $W+$ jets and $t\bar{t}$ events; see Fig. 7.6(a) and 7.6(b). Using $\not\!\!E_{\text{T}}$ templates from these variations to redo the binned likelihood fit, we give QCD estimations due to variations of $t\bar{t}$ (W+jets) Q^2 scale and matching threshold in Tab. 7.13.

Q^2 scale and matching threshold also affect the flavor fractions and event tagging efficiencies of W+jets events. Tab. 7.14 shows W+jets estimation due to the variations of Q^2 scale and matching threshold, compared to the central W+jets estimation in Section 7.1.2.

Table 7.12: The table summarizes JES effect on the measured $\sigma_{t\bar{t}}$.

	central	JES up	JES down
$\sigma_{t\bar{t}}^{\text{measure}}$ (pb)	161.2	158.5	167.8

Other than their effects on the background estimation, they also affect ϵ_i and the measured total cross sections, as seen in Tab. 7.15 and 7.16.

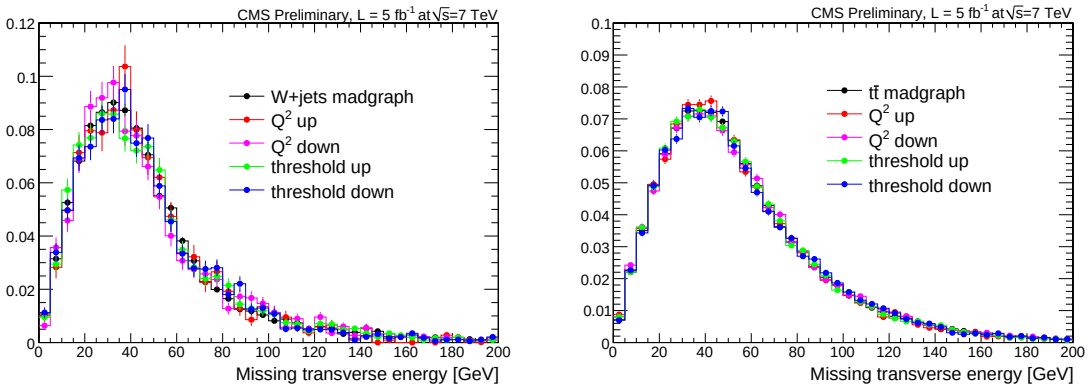

(a) (b)

Figure 7.6: $\not{E}_{\text{T}}$ templates of W+jets (7.6(a)) and $t\bar{t}$ (7.6(b)) due to variations of Q^2 scale and matching threshold.

Table 7.13: The table summarizes QCD estimations due to variations of scale Q^2 and matching threshold. The uncertainties are from fitting.

$N_{\text{jets}}^{\text{QCD}}$	3	4	5	6	7	≥ 8
central	521.4 ± 19.2	124.9 ± 9.0	13.6 ± 2.9	0.18 ± 0.34	0.0 ± 3.0	0.0 ± 2.0
$t\bar{t}$ Q^2 up	520.9 ± 19.1	129.6 ± 9.2	19.2 ± 3.5	1.6 ± 1.0	0.0 ± 2.0	0.0 ± 1.6
$t\bar{t}$ Q^2 down	527.6 ± 19.3	117.1 ± 8.7	2.9 ± 1.4	0.0 ± 7.0	0.0 ± 3.0	0.0 ± 2.0
$t\bar{t}$ th up	516.4 ± 19.1	126.7 ± 9.1	10.2 ± 2.5	0.0 ± 3.0	0.0 ± 1.0	0.0 ± 1.0
$t\bar{t}$ th down	534.7 ± 19.5	127.3 ± 9.1	0.0 ± 2.0	0.0 ± 11.1	0.0 ± 4.0	0.0 ± 3.3
W+jets Q^2 up	505.2 ± 18.9	128.1 ± 9.1	13.6 ± 2.9	0.22 ± 0.39	0.0 ± 3.0	0.0 ± 1.0
W+jets Q^2 down	527.6 ± 19.3	117.1 ± 8.7	2.9 ± 1.4	0.20 ± 0.35	0.0 ± 4.0	0.0 ± 1.0
W+jets th up	562.7 ± 20.4	106.4 ± 8.5	14.5 ± 3.1	0.21 ± 0.38	0.0 ± 4.0	0.0 ± 1.0
W+jets th down	545.4 ± 20.0	136.3 ± 9.7	14.4 ± 3.2	0.21 ± 0.37	0.0 ± 4.3	0.0 ± 1.0

Table 7.14: The table summarizes W+jets estimations from variations of scale Q^2 and matching threshold. Only statistic uncertainties are quoted.

$N_{\text{jets}}^{\text{W+jets}}$	3	4	5	6	7	≥ 8
central	655.4 ± 63.6	191.8 ± 26.8	57.8 ± 12.6	11.9 ± 5.6	0.0 ± 0.0	0.0 ± 0.0
W+jets Q^2 up	565.9 ± 246.6	185.4 ± 114.2	137.6 ± 95.3	16.9 ± 12.8	0.0 ± 0.0	0.0 ± 0.0
W+jets Q^2 down	791.9 ± 151.5	154.4 ± 48.9	62.5 ± 28.7	0 ± 0	0.0 ± 0.0	0.0 ± 0.0
W+jets th up	578.9 ± 165.1	316.2 ± 106.0	0.0 ± 0.0	26.7 ± 24.6	0.0 ± 0.0	0.0 ± 0.0
W+jets th down	872.8 ± 228.0	223.0 ± 87.6	36.2 ± 31.4	0.0 ± 0.0	0.0 ± 0.0	0.0 ± 0.0

Table 7.15: The table summarizes Q^2 and matching threshold effects on ϵ_i from $t\bar{t}$ MC, as defined in Eq. 7.3

ϵ_i	$N_{\text{jets}} = 3$	$N_{\text{jets}} = 4$	$N_{\text{jets}} = 5$	$N_{\text{jets}} = 6$	$N_{\text{jets}} = 7$	$N_{\text{jets}} \geq 8$
central	0.0298	0.0222	0.0134	0.0096	0.0080	0.0067
$t\bar{t}$ Q^2 up	0.0298	0.0217	0.0125	0.0084	0.0069	0.0056
$t\bar{t}$ Q^2 down	0.0299	0.0226	0.0142	0.0105	0.0084	0.0064
$t\bar{t}$ th up	0.0297	0.0221	0.0135	0.0092	0.0074	0.0060
$t\bar{t}$ th down	0.0303	0.0228	0.0140	0.0101	0.0074	0.0062

Table 7.16: The table summarizes Q^2 scale and matching threshold effects on the measured $t\bar{t}$ cross section $\sigma_{t\bar{t}}^{\text{measure}}$.

	central	$t\bar{t}$ Q^2 up	$t\bar{t}$ Q^2 down
$\sigma_{t\bar{t}}^{\text{measure}}$ (pb)	161.2	163.0	158.6
	central	W+jets Q^2 up	W+jets Q^2 down
$\sigma_{t\bar{t}}^{\text{measure}}$ (pb)	161.2	160.9	160.3
	central	$t\bar{t}$ th up	$t\bar{t}$ matching threshold down
$\sigma_{t\bar{t}}^{\text{measure}}$ (pb)	161.2	161.3	157.6
	central	W+jets th up	W+jets matching threshold down
$\sigma_{t\bar{t}}^{\text{measure}}$ (pb)	161.2	160.9	158.4

7.2.3 Systematic Uncertainties on Backgrounds

- The QCD template is extracted from the control region C requiring 0.3 <relIso< 1.0. The template shifts when applying different relIso cuts. We loose the relIso cut (relIso> 0.2), and use the same method described in Section 7.1.1 to re-estimate the QCD background and then take the difference as the systematic uncertainty due to template shift. Tab. 7.17 shows the numbers of QCD events estimated using control region 0.3 <relIso< 1.0 and relIso> 0.2 respectively.

Table 7.17: The tabel compares the number of QCD events between using control region 0.3 <relIso< 1.0 and relIso> 0.2. The difference is taken as the systematic uncertainty.

$N_{\text{jets}}^{\text{QCD}}$	3	4	5	6	7	≥ 8
central (0.3 <relIso< 1.0)	521.4 ± 19.2	124.9 ± 9.0	13.6 ± 2.9	0.18 ± 0.34	0.0 ± 3.0	0.0 ± 2.0
syst. (relIso> 0.2)	606.8 ± 17.4	131.4 ± 7.4	4.2 ± 1.3	0.0 ± 2.0	0.0 ± 4.0	0.0 ± 2.0

- The systematic uncertainty of W+jets is from flavor fraction correction, its contribution can be found in Tab. 7.9.

- An estimate of the uncertainty on remaining backgrounds (Z+jets, single top and EWK) is performed by varying their predicted cross section with ±30% which is roughly equal to the uncertainty in the measurements of these cross sections.

7.2.4 Others

We also include uncertainties 1) from measured integrated luminosity, which is 2.2%; 2) from electron selection efficiency which combines the contribution from trigger and ID/relIso, resulting in a total of 3% uncertainty; 3) from scale factors in b-tagging efficiency described in Section 5.3.3.3; 4) due to Parton Distribution Function (PDF). PDF uncertainty is

estimated using the standard $t\bar{t}$ sample from MADGRAPH with the CTEQ66 PDF set and applying the re-weighting method, as described in [124].

7.2.5 Summary of the Systematic Uncertainties

A summary of the systematic uncertainties on the normalized differential cross section is given in Tab. 7.18. Due to the normalization in the differential cross section measurement, the systematic uncertainties that are correlated across all bins in the measurement cancel out, i.e. uncertainty from the integrated luminosity, electron selection efficiency, scale factors for b-tagging efficiency.

The uncertainty from JES increases as jet number increases and becomes one of the major sources of uncertainty in higher jet bins. Q^2 scale systematics also increase along N_{jets} because the higher jet bins have smaller statistics and when a larger Q^2 generates more jets, the feed-down from lower to higher jet bins generate a bigger relative effect in the higher jet bins. In the $N_{\text{jets}} = 7,\ \geq 8$, the data statistic uncertainty is another major source of uncertainty.

Table 7.18: Breakdown of systematic and statistical uncertainties on normalized differential cross section (in %).

source	$N_{\text{jets}} = 3$	$N_{\text{jets}} = 4$	$N_{\text{jets}} = 5$	$N_{\text{jets}} = 6$	$N_{\text{jets}} = 7$	$N_{\text{jets}} \geq 8$
Jet Energy Scale	3.47	1.93	5.01	9.03	10.12	13.79
Jet Energy Resolution	0.39	0.35	0.71	1.07	0.95	1.49
b-Tagging	0.43	0.28	0.57	0.79	1.23	1.33
Pile-up	0.34	0.29	0.54	0.60	0.07	0.08
HLT/eID/relIso	0.07	0.05	0.06	0.08	0.09	0.12
$t\bar{t}$ Q^2 scale	1.21	1.07	5.21	12.76	13.70	18.78
W+jets Q^2 scale	1.33	1.21	2.42	2.80	0.55	0.55
$t\bar{t}$ matching threshold	0.46	0.58	1.24	3.67	10.19	10.96
W+jets matching threshold	2.05	1.82	3.09	4.06	1.79	1.78
PDF	1.20	0.10	2.20	4.30	7.00	9.10
W+jets flavor fraction	1.27	1.02	1.28	1.18	0.63	0.69
W+jets normalization	0.28	0.23	0.30	0.45	0.27	0.44
Z+jets cross section	0.17	0.10	0.20	0.18	0.22	0.30
Single top cross section	0.90	0.58	0.98	1.09	1.21	1.77
EWK cross section	0.03	0.02	0.04	0.04	0.03	0.05
QCD Eestimation	0.60	0.50	0.71	1.25	2.68	3.35
Luminosity	0.13	0.08	0.14	0.16	0.17	0.25
Total syst.	4.95	3.46	8.86	17.53	21.40	27.62
MC statistic	0.24	0.20	0.37	0.88	1.26	0.76
data statistic	1.44	1.49	2.49	4.82	9.54	18.29
Total stat.	1.46	1.50	2.51	4.89	9.62	18.30
stat.$\oplus$syst.	5.16	3.78	9.21	18.20	23.47	33.13

7.3 Results

The numbers of data and background events in $N_{\text{jets}} = 3,\ 4,\ 5,\ 6,\ 7,\ \geq 8$ are summarized in Tab. 7.19, where the total uncertainties are quoted. Using the listed numbers, $t\bar{t}$ events measured from data in each jet multiplicity bin is calculated by the following equation,

$$\begin{aligned} N_{t\bar{t}}^{\text{data}} &= N_{\text{data}} - N_{\text{BG}} \\ &= N_{\text{data}} - N_{\text{W+Jets}}^{\text{data}} - N_{\text{QCD}}^{\text{data}} - N_{\text{single-top}}^{\text{MC}} - N_{\text{Z+jets}}^{\text{MC}} - N_{\text{EWK}}^{\text{MC}}. \end{aligned} \tag{7.9}$$

Tab. 7.20 and Fig. 7.7(a) show the amount of $t\bar{t}$ events measured in data for each jet bin. There is a good agreement between data and MC expectation (Madgraph). A comparison of the data with different $t\bar{t}$ MC expectations (Madgraph, POWHEG, Herwig6) is also shown in Fig. 7.7(a).

Table 7.19: Number of events in $N_{\text{jets}} = 3,\ 4,\ 5,\ 6,\ 7,\ \geq 8$ for all processes. QCD and W+jets events are estimated using the data driven method from Section 7.1, while single top, Z+jets and EWK events are estimated using MC expectation.

	$N_{\text{jets}} = 3$	$N_{\text{jets}} = 4$	$N_{\text{jets}} = 5$	$N_{\text{jets}} = 6$	$N_{\text{jets}} = 7$	$N_{\text{jets}} \geq 8$	documentation
N_{data}	8297 ± 91.1	5836 ± 76.4	2113 ± 46.0	562 ± 23.7	126 ± 11.2	32 ± 5.7	Tab. 5.11
$N_{\text{W+Jets}}^{\text{data}}$	$655.4^{+232.1}_{-223.9}$	$191.8^{+70.6}_{-68.4}$	$57.8^{+23.4}_{-22.8}$	11.9 ± 6.9	0.0 ± 0.0	0.0 ± 0.0	Table 7.9
$N_{\text{QCD}}^{\text{data}}$	521.4 ± 87.5	124.9 ± 11.1	13.6 ± 9.7	0.18 ± 0.3	0.0 ± 3.0	0.0 ± 2.0	Table 7.2
$N_{\text{single-top}}^{\text{MC}}$	599 ± 6.4	236.8 ± 4.2	63.6 ± 2.3	15.1 ± 1.2	3.0 ± 0.5	0.2 ± 0.1	Tab. 5.11
$N_{\text{Z+jets}}^{\text{MC}}$	98.4 ± 6.5	33.2 ± 3.8	6.4 ± 1.7	2.1 ± 0.9	0.3 ± 0.4	0.0 ± 0.0	Table 5.11
$N_{\text{EWK}}^{\text{MC}}$	18.7 ± 0.8	5.5 ± 0.4	1.0 ± 0.2	0.2 ± 0.1	0.1 ± 0.1	0.0 ± 0.0	Tab. 5.11

Table 7.20: The number of $t\bar{t}$ events calculated via Eq. 7.9 in $N_{\text{jets}} = 3,\ 4,\ 5,\ 6,\ 7$ and ≥ 8.

	$N_{\text{jets}} = 3$	$N_{\text{jets}} = 4$	$N_{\text{jets}} = 5$	$N_{\text{jets}} = 6$	$N_{\text{jets}} = 7$	$N_{\text{jets}} \geq 8$
$N_{t\bar{t}}^{\text{MC}}$	6737 ± 9.8	5272.5 ± 8.7	1968.2 ± 5.3	565.1 ± 2.8	140.0 ± 1.4	37.8 ± 0.7
$N_{t\bar{t}}^{\text{data}}$	6404.1 ± 518.7	5243.8 ± 215.1	1970.6 ± 116.5	532.5 ± 77.2	122.6 ± 15.7	31.8 ± 6.6

Based on the jet multiplicity in Tab. 7.20, the inclusive $t\bar{t}$ cross section defined in Eq. 7.1 is $\sigma_{t\bar{t}}^{\text{measure}} = 161.2^{+12.4}_{-11.6}$ pb which agrees with the NNLL calculation. Then the

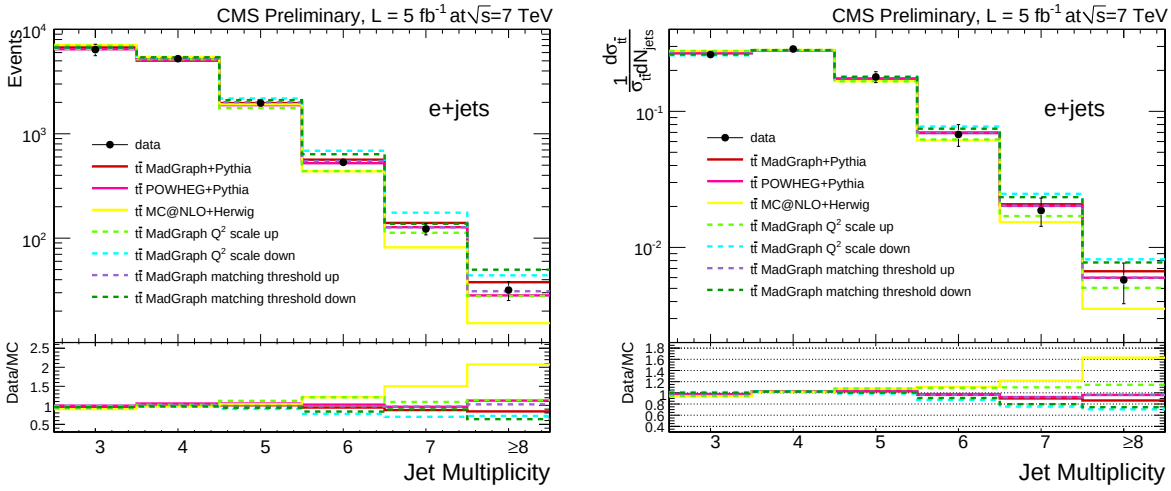

(a) (b)

Figure 7.7: 7.7(a) shows the jet multiplicity distribution of $t\bar{t}$ measured from data using Eq. 7.9, and 7.7(b) shows the measured normalized differential cross section of $t\bar{t}$ with respect to the jet multiplicity. Data are compared with MC expectations generated by different generators and also compared with Q^2, matching threshold up and down MC samples Total uncertainties are quoted here.

normalized differential cross section is calculated via Eq. 7.2. Tab. 7.21 and Fig. 7.7(b) show the measured normalized differential cross section of $t\bar{t}$ in jet multiplicity bins. The measurement is compared with different MC expectations produced by different generators. No deviation from MC@NLO (Madgraph, POWHEG, Herwig6) predictions is observed from the measurement within the uncertainties.

Table 7.21: The table shows the measured normalized differential cross section of $t\bar{t}$ in $N_{\text{jets}} = 3,\ 4,\ 5,\ 6,\ 7,\ \geq 8$, compared with MC expectation (Madgraph).

$\frac{d\sigma}{\sigma_{t\bar{t}} dN_{jets}}$	$N_{\text{jets}} = 3$	$N_{\text{jets}} = 4$	$N_{\text{jets}} = 5$	$N_{\text{jets}} = 6$	$N_{\text{jets}} = 7$	$N_{\text{jets}} \geq 8$
Madgraph MC	$0.268 \pm 8 \times 10^{-5}$	$0.281 \pm 8 \times 10^{-5}$	$0.174 \pm 6 \times 10^{-5}$	$0.070 \pm 4 \times 10^{-5}$	$0.021 \pm 2 \times 10^{-5}$	$0.007 \pm 1 \times 10^{-5}$
data	0.261 ± 0.013	0.287 ± 0.011	0.179 ± 0.016	0.068 ± 0.012	0.019 ± 0.004	0.006 ± 0.002

Decreasing the values of Q^2 effectively increases the value of α_s, and ISR effects is also included in Q^2 scale MC sample, all of which result in an enhanced radiative production of additional partons. This increased production in turn leads to more jets. From the

comparison between the measurement and Q^2 scale up and down MC, we can see such Q^2 scale effect in $N_{\text{jets}} = 5,\ 6,\ 7, \geq 8$. This measurement is included in CMS Physics Analysis Summary TOP-12-018.

CHAPTER 8

Summary and Outlook

This thesis presents a study of top pair production in the electron plus jets channel. First, the production cross section is measured using pp collision data at $\sqrt{s} = 7$ TeV with an integrated luminosity of 857.7 pb^{-1}. $t\bar{t}$ events are selected according to the properties of the final state topology. A binned template fit method is then used to extract the number of $t\bar{t}$ events. The charge asymmetry property of W+jets events is used to extract the template of W+jets from data. A QCD template is also obtained from data, by using the non-isolation property of electrons in the QCD samples. The cross section and full uncertainties are determined by a pseudo-experiment-based Neyman construction, which treats systematic uncertainties as nuisance parameters. This measurement yields a $t\bar{t}$ production cross section of $\sigma_{t\bar{t}} = 166.7^{+78.2}_{-69.3}$ (stat. $\oplus$ syst.) pb. The large uncertainty comes from the statistic limits in the W+jets template and large statistic fluctuation in the QCD template. However, the central value is still consistent with the theoretical prediction. Moreover, the data driven methods developed in this method can be applied in further studies with more integrated luminosity.

The second analysis described in this thesis is the measurement of a normalized differential cross section of $t\bar{t}$ events with respect to jet multiplicity. The full dataset taken in 2011 is used, which corresponds to an integrated luminosity of 5 fb^{-1}. In order to achieve a precise measurement, we rely on a b-tagging technique to suppress most QCD and W+jets backgrounds. Similar methods as those in the cross section measurement are employed in the estimation of the remaining backgrounds. The normalized differential

cross section is measured by a simple counting method. In this analysis, the measured total cross section for normalization is $\sigma_{t\bar{t}} = 161.2^{+12.4}_{-11.6}$ (stat. $\oplus$ syst.) pb. The precision is improved due to the increasing statistics and efficient background rejection of b-tagging. The measured normalized differential cross section is compared with different MC samples for testing perturbative QCD, and a good agreement has been observed.

During 2012, the center of mass energy was increased to 8 TeV, and around 20 fb^{-1} data has already been collected in both CMS and ATLAS. The measured cross section can achieve an uncertainty less than 7%. Such a precision challenges the calculation of perturbative QCD in NNLO. The tremendous amount of data allows many differential cross section measurements which are sensitive to new physics. LHC finished its first run on Feb. 14$^{\text{th}}$ 2013, and will be upgraded in one year to reach its designed energy $\sqrt{s} = 14$ TeV and a peak luminosity of 10^{34} cm^{-2}s^{-1}. The upgrades of CMS including the whole pixel detector, CSC, RPC, HCAL electronics and triggers, all of which will make sure the detector will operate at its designed performance in the high luminosity environment. The upgraded LHC will open a new era for both top quark physics and physics beyond the SM.

APPENDIX A

The Particle Flow Reconstruction

The PF reconstruction follows three major steps. First, the fundamental "elements", including the charged particle tracks and the calorimeter clusters, are reconstructed. To achieve a high efficiency and a low fake rate, an iterative track finding strategy and a cluster algorithm were developed, which are described Section A.1. Then these elements are topologically linked into "blocks" via a link algorithm described in Section A.2. In the third step, the blocks will be interpreted as particles using PF algorithm, see Section A.3

A.1 Iterative Tracking & Calorimeter Clustering

A.1.1 Iterative Tracking

It has been shown that the incorporation of tracking information into the jet reconstruction, as opposed to using the calorimeters only, is of great advantage. This is because i) approximately two thirds of the jets' energy is carried by charged particles; ii) charged hadrons if detected by the calorimeters only, would have a degraded energy resolution and a biased direction. The reconstruction of charged particles heavily relies on the tracker because its resolution outperforms the calorimeters for charged hadrons with transverse momenta (p_T) up to $\mathcal{O}(300)$ GeV, and it also precisely measures the direction of the charged particles emanating from the collision vertex.

The tracks needs to be reconstructed with near 100% efficiency. A low fake rate is also

required to avoid excess energy counting. An iterative tracking algorithm is designed to meet these two requirements. First, tracks are seeded and reconstructed with a very tight criteria. This step yields a very low fake rate but moderate track finding efficiency. Then, the hits unambiguously assigned to these tracks are removed from the list. Track reconstruction using remaining hits is repeated with progressively looser criteria, which increase efficiency while maintaining a negligible fake rate. In the fourth and fifth iteration, the constraint on the vertex position is relaxed to allow the secondary vertex reconstruction. This iterative technique allows tracking efficiencies higher than 90% for charged particles in jets. Particles with momentum as low as 150 MeV and created as far as 50 cm from the beam axis can be reconstructed with a fake rate of the order of one percent [82].

A.1.2 Calorimeter Clustering

When a particle enters the calorimeters, it will deposit energy in different cells. The deposited energy are clustered using an algorithm specific to PF reconstruction. The clustering algorithm must be highly efficient, and be able to measure the energy and direction of stable neutral particles and to distinguish closely-spaced energy deposits. The algorithm is developed and used in the ECAL, HCAL and PS but not in the HF, where each cell is treated as a single cluster.

The clustering starts with the identification of calorimeter cell energy maxima above a given threshold, which form "cluster seeds". These seeds are used to create "topological clusters" by collecting nearby cells with energy exceeds the predefined threshold. These nearby cells should also have at least one side in common with a cell already in the cluster. A topological cluster gives rise to as many "particle flow clusters" as seeds. The energy and position of the each PF cluster are determined by an iterative procedure. First, each cluster

is assigned a position equal to that of its original seed. Second, the energy of each cell in the topological cluster is shared among all PF clusters proportional to $\exp(-d_{ij}^2/R)$, where d_{ij} is the distance between PF cluster i and cell j, R is a constant number (5 cm for ECAL and 10 cm for HCAL). The position of each cluster is then re-computed as the average position of its cells. The energies of the PF clusters are again determined with these new positions.

A.2 Linking algorithm

Particles generally interact with more than one sub-detector, then produce several PF elements such as tracks, ECAL and HCAL clusters. The next step is to link together these elements from the same original particle without double counting from different detectors. The link algorithm provisionally links all pairs of elements, the quality of the link is expressed as the distance in $\eta - \phi$ plane between two linked elements. Elements that are either directly or indirectly linked are used to create "blocks" of elements. The high granularity of the CMS detectors ensures that blocks typically contain only one, two or three elements.

A charged particle track is linked to a given cluster if the extrapolated position is within the cluster boundaries. These boundaries can be enlarged to account for cracks in the detector, uncertainty in the position of the shower maximum and multiple scattering. In the case of electrons, the link between a track and ECAL must also incorporate all bremsstrahlung photons emitted by the electrons. Clusters in each of the ECAL and HCAL, or PS and ECAL are associated with each other when the cluster in the less granular calorimeter completely contains the cluster in the more granular calorimeter, unless a track can link them both. Finally in the case of muons, a charged-particle track and a muon track in the muon system is linked when a global fit between the two tracks returns a χ^2

above a given threshold. This χ^2 then becomes the link measure itself; in case more tracker tracks fit to the same muon track, only the one with the smallest χ^2 is retained.

A.3 Particle Flow Algorithm

The particle reconstruction and identification are performed on the blocks of linked elements using PF algorithm. The PF algorithm assigns the elements within a block to only one particle, and then progressively removes them from the blocks to reduce the combinatorics. The algorithm runs iteratively until no more elements are left.

PF algorithm starts by removing tracks and energy deposits in the calorimeters associated with PF muons. A PF muon is a global muon whose momentum returned by the global fit is consistent with the momentum measured from the tracker within three standard deviations. The energy deposit estimated from cosmic ray is around 3 GeV with an uncertainty of ±100%. Next, the electron tracks are reconstructed using the track seeded approach, and then required to pass a loose track pre-selection, which improve the reconstruction efficiency for low p_T and non-isolated electrons. The pre-identified tracks are re-fit with a Gaussian-Sum Filter and linked to PF clusters that matches their extrapolation to the calorimeters. The final electron identification is performed by a multivariate discriminator, and the identified electron is defined as a PF electrons. Tracks and PF clusters associated with PF electrons, the clusters linked by the bremsstrahlung recovery are removed from further processing. Details of the reconstruction and identification of electrons and muons are discussed further in Section 4.2 and 4.3.

The remaining elements may give rise to charged hadrons, photons or neutral hadrons. Since a track can be directly connected to a number of ECAL and HCAL clusters, the

neutral particles can be separated from the charged particles in the "block" by comparing the momentum of the linked tracks to the total calibrated cluster energy. In the case that several tracks are linked to the same cluster, the sum of their momentum is compared to the energy deposit. Conversely, if a track is linked to more than one HCAL cluster, only the closest cluster is retained for the comparison. The same happens for ECAL clusters, but more consideration is needed to account for hadronic shower fluctuation and overlapping photons.

Each of the remaining tracks gives rise to a PF charged hadron, with momentum equal to the track momentum. Its energy is calculated by assuming that the charged particle mass is equal to the charged pion mass. If the calibrated calorimetric energy is comparable with the track momentum within the uncertainties, the momentum and energy of such PF charge hadron are derived by a fit to the track and cluster energy otherwise. If calibrated energy is greater than the total track momentum by more than the calorimetric energy resolution, it indicates that the presence of neutral particles in the block. If the excess is larger than the total ECAL energy of the block, a PF photon is reconstructed with the ECAL energy. The rest of the excess energy is assigned to a PF neutral hadron. If the excess is less than the total ECAL energy, a PF photon only is reconstructed. Remaining ECAL and HCAL clusters in an event not linked to tracks give rise to PF photons and neutral hadrons respectively.

PF jets in an event are reconstructed from a full set of PF particles using the anti-k_T jet clustering algorithm, which will be described in Section 4.4. The missing transverse energy $\not{E}_{\mathrm{T}}$ of an event is computed as the negative vector sum of the $\vec{p}_T$ of all PF particles, which will be described in Section 4.5

APPENDIX B

Lists of Data and MC Samples

The data samples used in the analysis of this thesis are listed in Tab. B.1. Tab. B.2 and B.3 list the Summer11 and Fall11 MC samples used in the analysis.

Table B.1: The single electron (electron had) Data samples used in top pair cross section (differential cross section) measurement. The JSON files used for select good luminosity blocks are also listed.

Dataset	Run Range	$\mathcal{L}$ [pb^{-1}]
data samples used in $t\bar{t}$ cross section measurement		
/SingleElectron/Run2011A-May10ReReco-v1	up to 163869	204.7
/SingleElectron/Run2011A-PromptReco-v4	165088-166967	653.0
JSON Cert_160404-163869_7TeV_May10ReReco_Collisions11_JSON_v2.txt		
JSON Cert_160404-167913_7TeV_PromptReco_Collisions11_JSON.txt		
data samples used in $t\bar{t}$ differential cross section measurement		
/ElectronHad/Run2011A-08Nov2011-v1	160404-175770	2286.0
/ElectronHad/Run2011B-19Nov2011-v1	175832-180252	2714.0
JSON Cert_160404-180252_7TeV_ReRecoNov08_Collisions11_JSON_v2.txt		

Table B.2: Summer11 MC datasets used in $t\bar{t}$ cross section analysis.

Process	Dataset
$t\bar{t}$	/TTJets_TuneZ2_7TeV-madgraph-tauola/Summer11-PU_S4_START42_V11-v1
W+Jets	/WJetsToLNu_TuneZ2_7TeV-madgraph-tauola/Summer11-PU_S4_START42_V11-v1
Z+Jets	/DYJetsToLL_TuneZ2_M-50_7TeV-madgraph-tauola/Summer11-PU_S4_START42_V11-v1
QCD	/QCD_Pt-20_MuEnrichedPt-15_TuneZ2_7TeV-pythia6/Summer11-PU_S4_START42_V11-v1
	/QCD_Pt-20to30_EMEnriched_TuneZ2_7TeV-pythia6/Summer11-PU_S4_START42_V11-v1
	/QCD_Pt-30to80_EMEnriched_TuneZ2_7TeV-pythia/Summer11-PU_S4_START42_V11-v1
	/QCD_Pt-80to170_EMEnriched_TuneZ2_7TeV-pythia6/Summer11-PU_S4_START42_V11-v1
	/QCD_Pt-20to30_BCtoE_TuneZ2_7TeV-pythia6/Summer11-PU_S3_START42_V11-v2
	/QCD_Pt-30to80_BCtoE_TuneZ2_7TeV-pythia6/Summer11-PU_S4_START42_V11-v1
	/QCD_Pt-80to170_BCtoE_TuneZ2_7TeV-pythia/Summer11-PU_S4_START42_V11-v1
Single-t t	/T_TuneZ2_t-channel_7TeV-powheg-tauola/Summer11-PU_S4_START42_V11-v1
Single-t tW	/T_TuneZ2_tW-channel-DR_7TeV-powheg-tauola/Summer11-PU_S4_START42_V11-v1
Single-t s	/T_TuneZ2_s-channel_7TeV-powheg-tauola/Summer11-PU_S4_START42_V11-v1
Single-$\bar{t}$ t	/Tbar_TuneZ2_t-channel_7TeV-powheg-tauola/Summer11-PU_S4_START42_V11-v1
Single-$\bar{t}$ tW	/Tbar_TuneZ2_tW-channel-DR_7TeV-powheg-tauola/Summer11-PU_S4_START42_V11-v1
Single-$\bar{t}$ s	/Tbar_TuneZ2_s-channel_7TeV-powheg-tauola/Summer11-PU_S4_START42_V11-v1
$t\bar{t}$ Q^2 scale up	/TTjets_TuneZ2_scaleup_7TeV-madgraph-tauola/Summer11-PU_S4_START42_V11-v1
$t\bar{t}$ Q^2 scale down	/TTjets_TuneZ2_scaledown_7TeV-madgraph-tauola/Summer11-PU_S4_START42_V11-v1
$t\bar{t}$ matching threshold up	/TTjets_TuneZ2_matchingup_7TeV-madgraph-tauola/Summer11-PU_S4_START42_V11-v1
$t\bar{t}$ matching threshold down	/TTjets_TuneZ2_matchingdown_7TeV-madgraph-tauola/Summer11-PU_S4_START42_V11-v1
W+ jets Q^2 scale up	/WJetsToLNu_TuneZ2_scaleup_7TeV-madgraph-tauola/Summer11-PU_S4_START42_V11-v1
W+ jets Q^2 scale down	/WJetsToLNu_TuneZ2_scaledown_7TeV-madgraph-tauola/Summer11-PU_S4_START42_V11-v1
W+jets matching threshold up	/WJetsToLNu_TuneZ2_matchingup_7TeV-madgraph-tauola/Summer11-PU_S4_START42_V11-v1
W+jets matching threshold down	/WJetsToLNu_TuneZ2_matchingdown_7TeV-madgraph-tauola/Summer11-PU_S4_START42_V11-v1

Table B.3: Fall11 MC datasets used in the $t\bar{t}$ differential cross section analysis.

Process	Dataset
$t\bar{t}$ Madgraph	/TTJets_TuneZ2_7TeV-madgraph-tauola/Fall11-PU_S6_START42_V14B-v2
W+Jets	/WJetsToLNu_TuneZ2_7TeV-madgraph-tauola/Fall11-PU_S6_START42_V14B-v1
Z+Jets	/DYJetsToLL_TuneZ2_M-50_7TeV-madgraph-tauola/Fall11-PU_S6_START42_V14B-v1
QCD	/QCD_Pt-20to30_EMEnriched_TuneZ2_7TeV-pythia6/Fall11-PU_S6_START42_V14B-v1
	/QCD_Pt-30to80_EMEnriched_TuneZ2_7TeV-pythia/Fall11-PU_S6_START42_V14B-v1
	/QCD_Pt-80to170_EMEnriched_TuneZ2_7TeV-pythia6/Fall11-PU_S6_START42_V14B-v1
	/QCD_Pt-20to30_BCtoE_TuneZ2_7TeV-pythia6/Fall11-PU_S6_START42_V14B-v1
	/QCD_Pt-30to80_BCtoE_TuneZ2_7TeV-pythia6/Fall11-PU_S6_START42_V14B-v1
	/QCD_Pt-80to170_BCtoE_TuneZ2_7TeV-pythia/Fall11-PU_S6_START42_V14B-v2
Single-t t	/T_TuneZ2_t-channel_7TeV-powheg-tauola/Fall11-PU_S6_START42_V14B-v1
Single-t tW	/T_TuneZ2_tW-channel-DR_7TeV-powheg-tauola/Fall11-PU_S6_START42_V14B-v1
Single-t s	/T_TuneZ2_s-channel_7TeV-powheg-tauola/Fall11-PU_S6_START42_V14B-v1
Single-$\bar{t}$ t	/Tbar_TuneZ2_t-channel_7TeV-powheg-tauola/Fall11-PU_S6_START42_V14B-v1
Single-$\bar{t}$ tW	/Tbar_TuneZ2_tW-channel-DR_7TeV-powheg-tauola/Fall11-PU_S6_START42_V14B-v1
Single-$\bar{t}$ s	/Tbar_TuneZ2_s-channel_7TeV-powheg-tauola/Fall11-PU_S6_START42_V14B-v1
WW	/WW_TuneZ2_7TeV_pythia6_tauola/Fall11-PU_S6_START42_V14B-v1
WZ	/WZ_TuneZ2_7TeV_pythia6_tauola/Fall11-PU_S6_START42_V14B-v1
ZZ	/ZZ_TuneZ2_7TeV_pythia6_tauola/Fall11-PU_S6_START42_V14B-v1
$t\bar{t}$ powheg	/TT_TuneZ2_7TeV-powheg-tauola/Fall11-PU_S6_START42_V14B-v1
$t\bar{t}$ NLO Herwig	/TT_TuneZ2_7TeV-mcatnlo/Fall11-PU_S6_START42_V14B-v1
$t\bar{t}$ Q^2 scale up	/TTjets_TuneZ2_scaleup_7TeV-madgraph-tauola/Fall11-PU_S6_START42_V14B-v1
$t\bar{t}$ Q^2 scale down	/TTjets_TuneZ2_scaledown_7TeV-madgraph-tauola/Fall11-PU_S6_START42_V14B-v2
$t\bar{t}$ matching threshold up	/TTjets_TuneZ2_matchingup_7TeV-madgraph-tauola/Fall11-PU_S6_START42_V14B-v2
$t\bar{t}$ matching threshold down	/TTjets_TuneZ2_matchingdown_7TeV-madgraph-tauola/Fall11-PU_S6_START42_V14B-v2
W+ jets Q^2 scale up	/WJetsToLNu_TuneZ2_scaleup_7TeV-madgraph-tauola/Fall11-PU_S6_START42_V14B-v1
W+ jets Q^2 scale down	/WJetsToLNu_TuneZ2_scaledown_7TeV-madgraph-tauola/Fall11-PU_S6_START42_V14B-v1
W+jets matching threshold up	/WJetsToLNu_TuneZ2_matchingup_7TeV-madgraph-tauola/Fall11-PU_S6_START42_V14B-v1
W+jets matching threshold down	/WJetsToLNu_TuneZ2_matchingdown_7TeV-madgraph-tauola/Fall11-PU_S6_START42_V14B-v1

References

1. S. Glashow, *Partial symmetries of weak interactions.* Nucl. Phys., 22 579588, 1961. 1
2. S. Weinberg, *A model of leptons.* Phys. Rev. Lett., 19, 12641266, 1967. 1
3. A. Salam and N. Svartholm. ed. , *Elementary Particle Physics: Relativistic Groups and Analyticity.* Eighth Nobel Symposium. Stockholm: Almquvist and Wiksell. pp. 367, 1968. 1
4. CDF Collaboration, *Observation of Top Quark Production in $\bar{p}p$ Collisions with the Collider Detector at Fermilab.* Phys. Rev. Lett. 74, 2626, 1995. 1, 11
5. DØ Collaboration, *Observation of the Top Quark.* Phys. Rev. Lett. 74, 2632, 1995. 1, 11
6. CMS Collaboration, *Measurement of the top quark-pair production cross section with ATLAS in pp collisions at $\sqrt{s} = 7$ TeV, 2010.* Eur.Phys.J.C71:1577, arXiv:1012.1792, 2011. 1
7. CMS Collaboration, *First Measurement of the Cross Section for Top-Quark Pair Production in Proton-Proton Collisions at $\sqrt{s} = 7$ TeV.* Phys. Lett., B695:424-443, arXiv:1010.5994, 2011. 1
8. J. Beringer et al. (Particle Data Group), *Review of Particle Physics.* Phys. Rev. D 86, 010001, 2012. x, 1, 2, 8, 10, 12, 15
9. F.-P. Schilling, *Top Quark Physics at the LHC: A Review of the First Two Years.* arXiv:1206.4484, 2012. 1
10. "Standard Model." http://en.wikipedia.org/wiki/Standard_Model. x, 4
11. C. S. Wu, E. Ambler, R. W. Hayward, D. D. Hoppes, and R. P. Hudson, *Experimental test of parity conservation in beta decay.* Phys. Rev. 105 1413-1414, 1957. 4
12. R. L. Garwin, L. M. Lederman, and M. Weinrich, *Observations of the failure of conservation of parity and charge conjugation in meson decays: the magnetic moment of the free muon.* Phys. Rev. 105 1415-1417, 1957. 4
13. N. Cabibbo, *Unitary Symmetry and Leptonic Decays.* Physical Review Letters 10 (12): 531-533., 1963. 5
14. "Why do we expect a higgs boson." http://www.quantumdiaries.org/2011/11/21/why-do-we-expect-a-higgs-boson-part-i-electroweak-symmetry-breaking/. x, 7
15. J. Goldstone, A. Salam and S. Weinberg, *Broken Symmetries.* Phys. Rev. 127, 965, 1962. 6
16. E. Fermi, *Fermi's theory of beta decay.* American Journal of Physics Volume 36, Issue 12, pp. 1150, 1968. 8

17. UA1 Collaboration, CERN, Geneva, Switzerland, *Recent results on intermediate vector boson properties at the CERN super proton synchrotron collider.* Phys. Lett. B 166, page 484, 1986. 8

18. R. Ansari et al., *Measurement of the standard model parameters from a study of W and Z bosons.* Phys. Lett. B 186, page 440, 1987. 8

19. ATLAS Collaboration, *Observation of a new particle in the search for the Standard Model Higgs boson with the ATLAS detector at the LHC.* Physics Letters B, 716(1):1-29, 2012. 8

20. CMS Collaboration, *Observation of a new boson at a mass of 125 GeV with the CMS experiment at the LHC.* Physics Letters B, 716(1):30-61, 2012. 8

21. "Gell-Mann matrices." http://en.wikipedia.org/wiki/Gell-Mann_matrices. 9

22. B. Andersson, G. Gustafson, G. Ingelman and T. Sjostrand, *Parton fragmentation and string dynamics.* Phys. Rept. 97, 31, 1983. 11

23. G. Marchesini and B.R. Webber, *Monte Carlo simulation of general hard processes with coherent QCD radiation.* Nuclear Physxcs B310 461-526, 1988. 11

24. J. C. Collins, D. E. Soper, and G. Sterman, *Heavy particle production in high-energy hadron collisions.* Nucl. Phys. B263, 37, 1986. 12

25. J. C. Collins, D. E. Soper and G. Sterman, *Factorization of Hard Processes in QCD.* Adv. Ser. Direct. High Energy Phys., 5 1-91., 1988. 12

26. V. N. Gribov and L. N. Lipatov, *Deep inelastic e p scattering in perturbation theory.* Sov. J. Nucl. Phys. 15, 438, 1972. 13

27. H.-L. Lai, et al., *New parton distributions for collider physics.* Phys. Rev. D82, 074024, 2010. 13

28. A.D. Martin et al., *Parton distributions for the LHC.* Eur.Phys.J. C63 189-285, 2009. 13

29. M.-A. Pleier, *Review of properties of the top quark from measurements at the Tevatron.* International Journal of Modern Physics A Volume 24, Issue 16n17, 10 July, 2009. x, 14

30. M. L. Mangano, *Two Lectures on Heavy Quark Production in Hadronic Collisions.* CERN-TH/97-328, hep-ph/9711337, 1997. 14

31. M. Jezabek and J.H. Kühn, *QCD corrections to semileptonic decays of heavy quarks.* Nucl. Phys. B 314, 1, 1989. 15

32. M. Jezabek and J.H. Kühn, *Top quark width: Theoretical update.* Phys. Rev. D. 48 R1910, 1993. 15

33. I.I.Y. Bigi et al., *Production and decay properties of ultra-heavy quarks.* Phys. Lett. B181, 157, 1986. 15

34. "Useful Diagrams of Top Signals and Backgrounds." http://www-d0.fnal.gov/

Run2Physics/top/top_public_web_pages/top_feynman_diagrams.html. x, 16

35. D. J. H. Chung, L. L. Everett, G. L. Kane, S. F. King, J. Lykken and L-T. Wang, *The soft supersymmetry-breaking Lagrangian: theory and applications*. Phys. Rept. 407, 1, 2005. 17

36. Z. Han, A. Katz, M. Son, and B. Tweedie, *Boosting Searches for Natural SUSY with RPV via Gluino Cascades*. arXiv:1211.4025, 2013. 17

37. L. Evans and P. Bryant (editors), *LHC Machine*. 3 S08001 doi: 10.1088/1748-0221/3/08/S08001, 2008. 19, 20

38. C. Leffèvre, *The CERN Accelerator Complex*. CERN-DI-0812015 http://cdsweb.cern.ch/record/1260465, 2008. x, 19

39. CMS Collaboration, *Measurement of CMS Luminosity*. Public Analysis Summary CMS PAS EWK-10-004, 2010. 20

40. The LHC Study Group, *Design study of the Large Hadron Collider (LHC): a multiparticle collider in the LEP tunnel*. CERN 91-03 (Pink Book), 1991. 20

41. F. Zimmermann and M. P. Zorzano-Mier, *Touschek Scattering in HERA and LHC*. CERN LHC-PROJECT-NOTE-244, 2000. 20

42. D. Fournier, *Performance of the LHC, ATLAS and CMS in 2011*. EPJ Web Conf. 28 01003, 2012. xiv, 21

43. CMS Collaboration, *Public CMS Luminosity Information*. https://twiki.cern.ch/twiki/bin/view/CMSPublic/LumiPublicResults, 2011. x, 21, 22

44. CMS Collaboration, *The CMS experiment at the CERN LHC*. Journal of Instrumentation (JINST), 3 S08004, 2008. x, xi, 22, 23, 25, 37, 38, 39, 42, 46

45. CMS Collaboration, *CMS tracking performance results from early LHC operation*. The European Physical Journal C -Particles and Fields 70 1165-1192, 2010. x, 24, 33

46. CMS Collaboration, *Commissioning and performance of the CMS pixel tracker with cosmic ray muons*. J. Instrum. 5 T03007, 2010. 25

47. CMS Collaboration, *CMS Physics Technical Design Report Volume I: Detector Performance and Software*. Technical Design Report CMS. CERN, Geneva, 2006. x, xi, 25, 34, 36, 38, 41

48. S. Königa, Ch. Hörmanna, R. Horisberger et al, *Building CMS pixel barrel detector modules*. Nucl. Instr. Meth. Phys. Res. A 582 776-780, 2007. x, 27

49. D. Kotlińskia, E. Bartzb, W. Erdmann et al, *The control and readout systems of the CMS pixel barrel detector*. Nucl. Instr. Meth. Phys. Res. A 565 73-78, 2006. x, 28

50. "Overview of hardware components in DAQ system (by Karl Ecklund)." https://twiki.cern.ch/twiki/bin/viewauth/CMS/PixelOnlineSoftware. x, 28

51. "I^2C." http://en.wikipedia.org/wiki/IC. 27

52. Souvik Das, *Status and performance of the Compact Muon Solenoid pixel*. Nucl. Instr. Meth. Phys. Res. A 623 147-149, 2010. x, 27, 31

53. "A Cursory Overview of Pixel Online Software for the DAQ Tutorial, author: Souvik Das." https://twiki.cern.ch/twiki/pub/CMS/PixelOnlineSoftware/PixelDAQTutorial17April2008.pdf. x, 29

54. "CMS Pixel Online Software and Calibrations, authors: A. Ryd, K. Ecklund, et al." https://twiki.cern.ch/twiki/pub/CMS/PixelOnlineSoftware/UsersGuide.pdf. 29, 30

55. P. Azzurri, *The CMS Silicon Strip Tracker*. Journal of Physics: Conference Series 41 127-134. doi:10.1088/1742-6596/41/1/011, 2006. 33

56. CMS Collaboration, *Commissioning and performance of the CMS silicon strip tracker with cosmic ray muons*. J. Instrum. 5 T03008, 2010. 33

57. P. Lecoq et al, *Lead tungstate ($PbWO_4$) scintillators for LHC EM calorimetry*. Nucl. Instrum. Meth. A 365 (1995) 291, 1995. 33

58. A.A. Annenkov, M.V. Korzhik and P. Lecoq, *Lead tungstate scintillation material*. Nucl. Instrum. Meth. A 490 (2002) 30, 2002. 33

59. I. Dafinei, E. Auffray, P. Lecoq M. Schneegans, *Lead tungstate for high energy calorimetry*. Mat. Res. Soc. Symp. Proc. 348 99, 1994. 34

60. M. Paganoni, *The CMS Electromagnetic Calorimeter*. Nuclear Science Symposium Conference Record, 2005 IEEE, 1034-1037, 2005. 35

61. CMS Collaboration, *Energy resolution of the barrel of the CMS electromagnetic calorimeter*. J. Instrum. 2 (2007) P04004, 2007. 36

62. CMS Collaboration, *Electromagnetic calorimeter calibration with 7 TeV data*. CMS Physics Analysis Summary CMS-PAS-EGM-10-003, 2010. 36

63. S. Abdullin et al., *Design, performance, and calibration of CMS hadron-barrel calorimeter wedges*. Eur. Phys. Journal C 55 (2008) 159-171, 2008. 39

64. S. Abdullin et al., *Design, performance, and calibration of CMS forward calorimeter wedges*. Eur. Phys. Journal C 53 (2008) 139-166, 2008. 39

65. S. Chatrchyan et al., *Performance of the CMS drift tube chambers with cosmic rays*. JINST, vol. 5, p. T03015, 2010. 41

66. S. Chatrchyan et al., *Performance of the CMS cathode strip chambers with cosmic rays*. JINST, vol. 5, p. T03018, 2010. 43

67. S. Chatrchyan et al., *Performance study of the CMS barrel resistive plate chambers with cosmic rays*. JINST, vol. 5, p. T03017, 2010. 43

68. "MSTW. MSTW homepage." http://mstwpdf.hepforge.org/plots/plots.html. xi, 43, 44

69. CMS Collaboration, *The TriDAS Project Technical Design Report: The Level-1*

Trigger. CERN-LHCC 2000-038, 2000. xi, 45, 46

70. N. Amapane, *The CMS Muon Trigger System*. CMS Conference Report CR 2003/047, 2003. 46, 47
71. CMS Collaboration, *Performance of the CMS Level-1 trigger during commissioning with cosmic ray muons and LHC beams*. JINST 5 T03002, 2010. 47
72. G. Bagliesi, *CMS high-level trigger selection*. Eur Phys J C 33, s1035-s1037, 2004. 47
73. CMS Collaboration, *The CMS High Level Trigger*. Eur. Phys. J. C 46, 605-667, 2006. 48
74. L. Agostino and M. Pieri, *HLT Selection of Electrons and Photons*. CMS Note 2006/078, 2006. 48
75. CMS Collaboration, *Tracking and Primary Vertex Results in First 7 TeV Collisions*. Public Analysis Summary CMS PAS TRK-2010-005, 2010. 49, 50
76. R. Fruewirth W. Waltenberger and P. Vanlaer, *Adaptive Vertex Fitting*. CMS Note 2007/008, 2007. 50
77. CMS Collaboration, *CMS Collaboration, Electron reconstruction within the particle flow Algorithm*. CMS Analysis Note CMS AN-2010/034, 2010. xi, 51
78. M. Pioppi, *A pre-identification for electron reconstruction in the CMS particle-flow algorithm*. J.Phys.Conf.Ser. 119 (2008) 032039, 2008. 51
79. CMS Collaboration, *Electron reconstruction and identification at* $\sqrt{s} = 7$ *TeV*. Public Analysis Summary CMS PAS-EGM-10-004, 2010. 52
80. CMS Collaboration, *Performance of muon identification in pp collisions at* $\sqrt{s} = 7$ *TeV*. CMS Physics Analysis Summary, CMS PAS-MUO-10-002, 2010. 53, 54
81. CMS Collaboration, *Commissioning of the particle-flow event reconstruction with leptons from J/Psi and W decays at 7 TeV*. Public Analysis Summary CMS PAS PFT-2010-003, 2010. 54
82. CMS Collaboration, *Particle-Flow Event Reconstruction in CMS and Performance for Jets, Taus, and* E_T^{miss}. Public Analysis Summary CMS PAS PFT-2009-001, 2009. 54, 136
83. M. Cacciari G. P. Salam and G. Soyez, *The anti-*k_T *jet clustering algorithm*. JHEP 04 (2008) 063, 2008. 55
84. CMS Collaboration, *Determination of Jet Energy Calibration and Transverse Momentum Resolution in CMS*. Journal of Instrumentation 6 no. 11, P11002, 2011. 56, 57, 98
85. CMS Collaboration, *Jet Energy Resolution in CMS at* $\sqrt{s} = 7$ *TeV*. CMS Physics Analysis Summary CMS-PAS-JME-10-014, 2010. 57
86. CMS Collaboration, *Missing transverse energy performance of the CMS detector*. JINST 6 P09001 doi:10.1088/1748-0221/6/09/P09001, 2011. 57

87. S. T. Poprocki, *SEARCH FOR WZ + ZZ PRODUCTION WITH MISSING TRANSVERSE ENERGY PLUS JETS WITH b ENHANCEMENT AT CDF AT SQRT(S) = 1.96 TeV*. Cornell Ph.D. Thesis, Chapter 4, 4.1, 2011. xi, 58

88. CMS Collaboration, *Identification of b-quark jets in the CMS experiment*. CMS Physics Analysis Summary CMS-PAS-BTV-12-001, 2012. xi, 59, 60, 61, 78

89. C. Weiser, *A Combined Secondary Vertex Based B-Tagging Algorithm in CMS*. CMS NOTE 2006/014, 2006. 59

90. CMS Collaboration, *Performance of b-jet identification in CMS*. CMS Physics Analysis Summary CMS-PAS-BTV-11-001, 2011. 60

91. UA1 Collaboration, *Study of heavy flavour production in events with a muon accompanied by jet(s) at the CERN proton-antiproton collider*. Z. Phys. C 37 489, 1988. 61

92. DØ Collaboration, *b-Jet Identification in the DØ Experiment*. Nucl. Instrum. Meth. A 620 490, 2010. 61

93. J. Alwall1, P. Demin et al. , *MadGraph/MadEvent v4: the new web generation*. JHEP, no. 09, 028, 2007. 66, 67

94. "Matrix Element Method." https://cp3.irmp.ucl.ac.be/projects/madgraph/wiki/MatrixElement. 66

95. T. Sjstrand, S. Mrenna, and P. Skands, *PYTHIA 6.4 physics and manual*. JHEP, no. 05, 026, 2006. 67

96. CMS Collaboration, *Measurement of the $t\bar{t}$ production cross section in pp collisions at $\sqrt{s} = 7$ TeV with lepton+jets final states*. CMS PAPER TOP-11-003, 2011. 67

97. "The POWHEG BOX." http://powhegbox.mib.infn.it/. 68

98. Geant4 Collaboration, S. Agostinelli, J. Allison et al., *Geant4-a simulation toolkit*. Nuclear Instruments and Methods in Physics Research A 506 250-303, 2003. 68

99. N. Kidonakis, *Next-to-next-to-leading soft-gluon corrections for the top quark cross section and transverse momentum distribution*. arXiv:1009.4935, 2010. 68, 69

100. M. L. Mangano, M. Moretti, F. Piccinini et al., *Matching matrix elements and shower evolution for top-pair production in hadronic collisions*. JHEP, no. 01, 013., 2007. 69

101. K. Melnikov and F. Petriello, *Electroweak gauge boson production at hadron colliders through $\mathcal{O}(\alpha_s^2)$*. Phys. Rev. D74 114017, arXiv:hep-ph/0609070, 2006. 69

102. N. Kidonakis, *Next-to-next-to-leading-order collinear and soft gluon corrections for t-channel single top quark production*. Phys. Rev. D 83 091503, arXiv:hep-ph/1103.2792, 2011. 69

103. N. Kidonakis, *Two-loop soft anomalous dimensions for single top quark associated production with a W^- or H^-*. Phys.Rev. D82 054018, arXiv:1005.4451, 2010. 69

104. N. Kidonakis, *Next-to-next-to-leading-logarithm resummation for s-channel single top*

quark production. Phys. Rev. D 81 054028, arXiv:hep-ph/1001.5034, 2010. 69

105. J. M. Campbell, R. K. Ellis, and C. Williams, *Vector boson pair production at the LHC*. JHEP 1107 018, arXiv:1105.0020, 2011. 69

106. "Top PAG Reference Selections for 2011." https://twiki.cern.ch/twiki/bin/viewauth/CMS/TWikiTopRefEventSel2011. 69

107. "Egamma Physics Trigger Group." https://twiki.cern.ch/twiki/bin/view/CMS/EgammaPTG. 70

108. CMS Collaboration, *A cut based method for electron identification in CMS*. CMS Analysis Note 2008/082 (2008), 2008. 71

109. "Jet Identification." https://twiki.cern.ch/twiki/bin/view/CMS/JetID. 73

110. "Pileup Reweighting Utilities." https://twiki.cern.ch/twiki/bin/viewauth/CMS/PileupMCReweightingUtilities. 75

111. CMS Collaboration, *Simultaneous Heavy Flavor and Top (SHyFT) Cross Section Measurement*. CMS Anlysis Note AN-2011/210, 2011. 77

112. CMS Collaboration, *Measurement of the inclusive top pair production cross section in the semi-leptonic muon and electron channels with the complete dataset from 2011 data taking period*. CMS Anlysis Note AN-2011/443, 2011. 77

113. "b Tag & Vertexing Physics Object Group." https://twiki.cern.ch/twiki/bin/viewauth/CMS/BtagPOG. Recommendation for b/c-tagging and mistagging Data/MC Scale Factors. xiv, 78

114. "b Tag & Vertexing Physics Object Group." https://twiki.cern.ch/twiki/pub/CMS/BtagPOG/SFlightFuncs.C. 78

115. C. Koma and W. J. Stirling, *Charge asymmetry in W+ jets production at the LHC*. Eur. Phys. J. C 69: 6773, 2010. 88

116. CMS Collaboration, *Jet Production Rates in Association with W and Z Bosons in pp Collisions at* $\sqrt{s} = 7$ *TeV*. JHEP 1201 (2012) 010, CERN-PH-EP-2011-125, 2012. 88, 89

117. "MCFM-Monte Carlo for FeMtobarn processes." http://mcfm.fnal.gov/. 89

118. CMS Collaboration, *Measurement of missing transverse energy in top pair events*. Public Analysis Summary CMS PAS TOP-12-019, 2012. 93

119. "QCD background update." https://twiki.cern.ch/twiki/pub/CMS/TTbarPlusX/QCD_background_update_10Oct.pdf. 93

120. L. Lyons, *Bayes and Frequentism: a particle physicists perspective, Contemporary Physics*. doi:10.1080/00107514.2012.756312, 2013. 104

121. K.S. Cranmer, *Frequentist Hypothesis Testing with Background Uncertainty*. arXiv:physics/0310108, 2003. 104

122. CMS Collaboration, *Measurement of the $t\bar{t}$ production cross section in pp collisions at 7 TeV in lepton+jets events using b-quark jet identification.* Phys. Rev. D 84, 092004, 2011. 119

123. CDF Collaboration, *Measurement of the $t\bar{t}$ production cross section in $p\bar{p}$ collisions at $\sqrt{s} = 1.96$ TeV using lepton+jets events with secondary vertex b-tagging.* Phys. Rev. D 71, 052003, 2005. 119, 121

124. P. Biallass, T. Hebbeker, C. Hof et al., *Parton Distribution Uncertainty Determination within CMSSW.* CMS Analysis Note AN-2009/048, 2009. 128